รายงานวิจัยฉบับสมบูรณ์

โครงการ “รูปแบบของเซ็นเซอร์สีแสดงการเปลี่ยนแปลงสัณฐานวิทยาของอนุภาคเงินระดับนาโนเมตรที่เกิดจากสารชีวโมเลกุล”

โดย ผู้ช่วยศาสตราจารย์ ดร.คเณศ วงษ์ระวี

เสร็จสิ้นโครงการ 15 ตุลาคม 2560

สัญญาเลขที่ TRG5880238

รายงานวิจัยฉบับสมบูรณ์

โครงการ “รูปแบบของเซ็นเซอร์สีแสดงการเปลี่ยนแปลงสัณฐานวิทยาของอนุภาคเงินระดับนาโนเมตรที่เกิดจากสารชีวโมเลกุล”

ผู้ช่วยศาสตราจารย์ ดร.คเณศ วงษ์ระวี
ภาควิชาเคมี คณะวิทยาศาสตร์ จุฬาลงกรณ์มหาวิทยาลัย

สนับสนุนโดยสำนักงานกองทุนสนับสนุนการวิจัยและ
จุฬาลงกรณ์มหาวิทยาลัย

Abstract

Project Code **:** TRG5880238

Project Title **:** Pattern recognized colorimetric sensor based on morphological change of silver nanoprisms (AgNPrs) induced by biological molecules

Investigator **:** Assistant Prof. Kanet Wongravee
Department of chemistry, Faculty of science, Chulalongkorn university

E-mail Address : kanet.w@chula.ac.th, kanet.wongravee@gmail.com

Project Period : 2 years

Herein, we present two works based on a shape evolution of 3D flower-like gold microstructures (3D-FLGMSs) from gold nanosheets induced by H_2O_2 with the presence of starch and phase phase transferring process of anisotropic silver nanoparticles (AgNPs) from aqueous to a wide range of organic solvents using graphene oxide as carrier. In the work, a systematic investigation of the influences of the parameters on the size, morphology and structural evolution of 3D-FLGMSs was presented. It was found that H_2O_2 plays a key role on the formation of 3D-FLGMSs as it promotes a rapid generation of small nanosheets with starch-bound {111} facet at the very early stage. The generated nanosheets undergo oriented attachment (OA) and transform into a large primary gold nanosheets with imperfect facet-binding. It later undergos a subsequent epitaxial growth of nanopetals from the imperfects turns the primary nanosheets into 3D-FLGNSs with lateral size as large as 30 μm within 120 min. The 3D-FLGNSs can be employed as SERS substrates which allow the detection limit of Rhodamine 6G (R6G) at the concectration as low as 0.1 μM. In the later work, we purpose the transferring process to transfer AgNPs in aqueous solution to the organic solvents by using graphene oxide (GOx) as a carrier. The transferring process was utilized by only two straightforward steps. Firstly, the composite of graphene oxide-silver nanoparticles (GO/AgNPs) were synthesized using N,N' dimethylformamide (DMF) as a reducing agent. Secondly, the composite GO/AgNP were modified with oleylamine (OAm) in order to improve hydrophobicity. It was found that the GO/AgNP-OAm are uniformly dispersed in the organic solvents for at least 18 hours after sonication. These two materials (3D-FLGMSs and GO/AgNP-OAm) have a potential to be used for sensing biological molecules (quanlitative and quantitative) in the future.

Keywords : flower-like gold microstructures, silver nanoparticles, phase transferring, graphene oxide, hydrogen peroxide

เอกสารแนบหมายเลข 2

บทคัดย่อ

รหัสโครงการ : TRG5880238
ชื่อโครงการ : รูปแบบของเซ็นเซอร์สีแสดงการเปลี่ยนแปลงสัณฐานวิทยาของอนุภาคเงินระดับนาโนเมตรที่เกิดจากสารชีวโมเลกุล
ชื่อนักวิจัย : ผู้ช่วยศาสตราจารย์ ดร.คเณศ วงษ์ระวี
ภาควิชาเคมี คณะวิทยาศาสตร์ จุฬาลงกรณ์มหาวิทยาลัย
E-mail Address : kanet.w@chula.ac.th, kanet.wongravee@gmail.com
ระยะเวลาโครงการ : 2 ปี

ในงานวิจัยนี้ผู้วิจัยได้เสนองานวิจัย 2 ชิ้นด้วยกันคือการเปลี่ยนรูปร่างของอนุภาคทองคำรูปร่างคล้ายดอกไม้ระดับไมโครเมตรที่เกิดจากอนุภาคทองคำแบบแผ่นระดับนาโนเมตร เหนี่ยวนำการเกิดด้วยไฮโดรเจนเปอร์ออกไซด์ในสารละลายแป้ง และงานที่เกี่ยวข้องกับการนำเสนอวิธีการเคลื่อนย้ายเฟสของอนุภาคเงินระดับนาโนเมตรจากน้ำไปยังตัวทำละลายอินทรีย์หลายชนิดด้วยการใช้แกรฟีนออกไซด์เป็นตัวนำพา ในงานวิจัยนี้ได้ศึกษาผลกระทบของตัวแปรต่าง ๆ ที่มีผลต่อการเกิดอนุภาคทองคำรูปร่างคล้ายดอกไม้ระดับไมโครเมตรเพื่อที่จะได้นำเสนอกลไกการเกิดได้ พบว่าไฮโดรเจนเปอร์ออกไซด์เป็นตัวแปรสำคัญในการทำให้อนุภาคทองคำเกิดเป็นรูปร่างคล้ายดอกไม้ ซึ่งรูปร่างนี้เกิดจากการรวมกันของอนุภาคทองคำแบบแผ่นระดับนาโนเมตรผ่านกระบวนการ oriented attachment จนกลายเป็นอนุภาคทองคำแบบแผ่นขนาดใหญ่ จากนั้นอนุภาคทองคำขนาดเล็กจะมารวมกับอนุภาคทองคำแบบแผ่นขนาดใหญ่ในบริเวณที่มีรอยหักที่ไม่สมบูรณ์เกิดเป็นลักษณะรูปร่างคล้ายดอกไม้ที่มีขนาดใหญ่ประมาณ 30 ไมโครเมตร โดยใช้เวลาการสังเคราะห์เพียง 120 นาที อนุภาคทองคำรูปร่างคล้ายดอกไม้ระดับไมโครเมตรยังถูกนำมาประยุกต์ใช้เป็นตัวขยายสัญญาณรามานโดยสามารถใช้วัดความเข้มข้นของ R6G ได้ในระดับต่ำ 0.1 µM สำหรับงานวิจัยอีกชิ้นหนึ่งเป็นการนำเสนอวิธีการเคลื่อนย้ายเฟสของอนุภาคเงินระดับนาโนเมตรจากน้ำไปยังตัวทำละลายอินทรีย์โดยอาศัยแกรฟีนออกไซด์เป็นตัวพา โดยวิธีการมีเพียง 2 ขั้นตอนแบบตรงไปตรงมาคือการสังเคราะห์คอมโพสิตระหว่างแกรฟีนออกไซด์กับอนุภาคเงินระดับนาโนเมตร จากนั้นทำการเคลื่อนย้ายเฟสโดยปรับปรุงพื้นผิวแกรฟีนออกไซด์ด้วยสาร oleylamine จากการทดลองพบว่าคอมโพสิตของระหว่างแกรฟีนออกไซด์กับอนุภาคเงินระดับนาโนเมตรที่ปรับปรุงพื้นผิวด้วย oleylamine แล้วนั้นสามารถกระจายตัวอยู่ในตัวทำละลายอินทรีย์ได้มากกว่า 18 ชั่วโมง ซึ่งเพียงพอต่อการประยุกต์ใช้งานในอุตสาหกรรม ซึ่งวัสดุอนุภาคทองคำรูปร่างคล้ายดอกไม้ระดับไมโครเมตรและคอมโพสิตของระหว่างแกรฟีนออกไซด์กับอนุภาคเงินระดับนาโนเมตร นั้นเป็นวัสดุที่มีแนวโน้มในการประยุกต์ใช้สำหรับตรวจวัดสารชีวโมเลกุลต่อไป

คำหลัก : อนุภาคทองคำรูปร่างคล้ายดอกไม้ระดับไมโครเมตร, อนุภาคเงินระดับนาโนเมตร, การเคลื่อนย้ายเฟส, แกรฟีนออกไซด์, ไฮโดรเจนเปอร์ออกไซด์

งานวิจัยชิ้นที่ 1

Shape evolution of 3D Flower-like Gold Microstructures from Gold Nanosheets via Oriented Attachment

In this study, we report the shape evolution pathways of 3D flower-like gold microstructures (3D-FLGMSs) from the nanosheets. The influences of the concentration of H_2O_2, starch and molar ratio of $[H_2O_2]/[HAuCl_4]$ were systematically investigated in detail. The developed method for the fabrication of 3D-FLGMSs is simple, effective, fast, green and efficient with industrial-scale production capability. To our knowledge, this is the first for the preparation of such a complex microstructure of 3D-FLGMSs using H_2O_2 as a green reducing agent and starch as stabilizer. It could serve as a challenge for the fabrication of microstructures using a simple chemical approach. Furthermore, a potential application of 3D-FLGMSs as SERS substrate was demonstrated.

Preparation of 3D-FLGMSs

The 3D-FLGMSs were synthesized by a simple wet chemical method using H_2O_2 as a reducing agent and starch as a stabilizer. Briefly, starch solution (25 mL, 2% w/v) and $HAuCl_4$ (1.25 mL, 0.5 M) were mixed under vigorous stirring for 30 min. The volume of the mixture was adjusted to 33.3 mL using deionized water and stirred for another 30 min before an instantly addition of H_2O_2 (16.7 mL, 30% w/w). The solution was stirred for another 5 min and kept in ambient condition without disturbance. Within 20 min, the golden yellow solution turned colourless with a concomitant formation of dark-brown solid 3D-FLGMSs together with a formation of many oxygen bubbles according to the following redox reaction.

$$2AuCl_4^-(aq)+3H_2O_2(aq)\rightarrow 2Au(s)+3O_2(g)+8Cl^-(aq)+6H^+(aq) \quad \Delta E^\circ_{cell}= +0.307\ V. \quad (1)$$

The mixture was kept undisturbed for another 100 min before the separation of 3D-FLGMSs by centrifugation. The 3D-FLGMSs were thoroughly washed with hot DI water before keeping as an aqueous suspension for further characterizations.

Results and discussions

H_2O_2 Induced 3D-FLGMS Formation

H_2O_2 is well known as a strong oxidizing agent. However, its mild reducing capability is suitable for the formation of anisotropic nanostructures, particularly silver nanoplates and gold nanosheets. The utilization of low concentration H_2O_2 is the key parameter as it enables a slow reduction allowing the nucleation and growth of gold nanosheets under a kinetically controlled environment. This phenomenon provides the formation of plate-like seeds that will further grow into nanoplates. The liberated oxidizing species (e.g. O_2/Cl^-) act as strong oxidative etchant which selectively dissolves the unstable seeds and preserves the plate-like seeds.

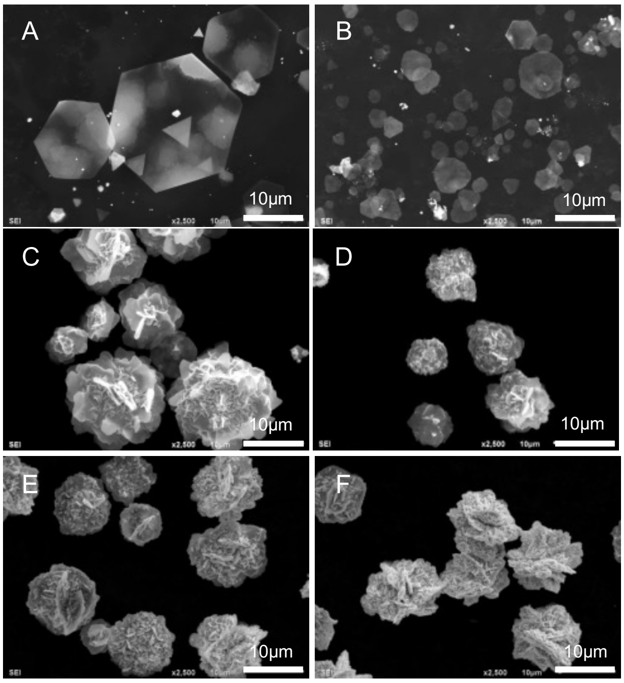

Figure 1 *SEM micrographs show morphological changes of gold nanostructures from nanosheets to 3D-FLGMS under the influence of the concentration of* H_2O_2*: (A) 3.2, (B) 32, (C) 320, (D) 970, (E) 1600 and (F) 3200 mM. The nanostructures were synthesized with 2.54 mM* $HAuCl_4$ *and 1% w/v starch.*

When a low concentration of H_2O_2 (3.2 mM) was employed, within 10 h, large gold nanosheets with an average lateral size of 9.2±5.2 μm (thickness of 20-50 nm) were produced as the major product (Figure 1A). The reaction time was determined by the fading of yellow colour of $HAuCl_4$ solution with the disappearance of O_2 bubbles. The clear solution implied that the $AuCl_4^-$ ions were completely consumed. Increasing H_2O_2 concentration from 3.2 to 32 mM decreases the reaction time to 8 h while small gold nanosheets with an average lateral size of 2.2±1.2 μm were created (Figure 1B). These observations on the generated gold nanosheets are in a good agreement with our previous work. As a high concentration of reducing agent was employed, the metal ions were rapidly reduced into Au nuclei in the early stage of the reaction. Therefore, the decrease of the particle size can be attributed to the insufficient of metal ions for the growth of gold nanosheets.

Interestingly, when the concentration of H_2O_2 was further increased to 320, 970, 1600, and 3200 mM, the complex structures defined as 3D-FLGMSs were produced within only 1 h (Figure 1C-F). According to the SEM images, morphology of 3D-FLGMSs is mainly stacking assembly of gold nanosheets (thickness of 40-110 nm, similar to petals of flowers). The morphological evolutions from nanosheets to 3D-FLGMSs were occurred when the concentration of H_2O_2 was over 320 mM. This observation suggests that high concentration of H_2O_2 is the key parameter that triggers the formation of 3D-FLGMSs. An adequate concentration of H_2O_2 is crucial for a rapid reduction that generates a large number of gold nanosheets. The nanosheets later undergo though aggregation and self-organization to 3D-FLGMSs. It should be noted that the surfaces of nanosheets were rough when the H_2O_2 concentration was higher than 1600 mM. These rough surfaces can normally occur in the system with fast growth rate.

Influence of Synthesis Parameters

As shown in the previous section, high concentration of H_2O_2 would be a crucial factor for the fabrication of 3D-FLGMS structure. We found that the molar ratio of $[H_2O_2]/[HAuCl_4]$ should be higher than ~60 to obtain the 3D-FLGMSs as shown below. Thus, employing the concentration of H_2O_2 3200 mM is preferred for the fabrication of 3D-FLGMSs as it can keep the value of molar ratio of $[H_2O_2]/[HAuCl_4]$ higher than 60 when the concentration of $HAuCl_4$ increases.

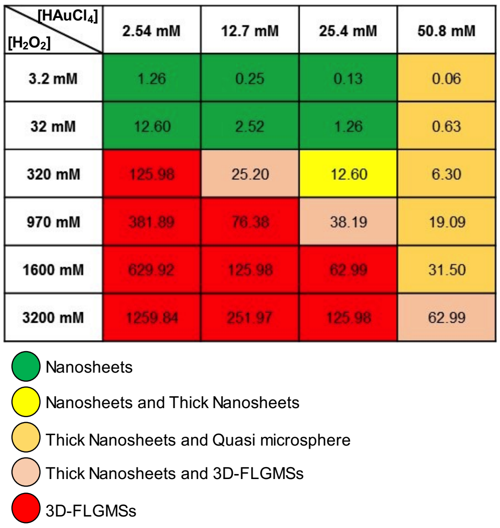

$[HAuCl_4]$ / $[H_2O_2]$	2.54 mM	12.7 mM	25.4 mM	50.8 mM
3.2 mM	1.26	0.25	0.13	0.06
32 mM	12.60	2.52	1.26	0.63
320 mM	125.98	25.20	12.60	6.30
970 mM	381.89	76.38	38.19	19.09
1600 mM	629.92	125.98	62.99	31.50
3200 mM	1259.84	251.97	125.98	62.99

● Nanosheets
● Nanosheets and Thick Nanosheets
● Thick Nanosheets and Quasi microsphere
● Thick Nanosheets and 3D-FLGMSs
● 3D-FLGMSs

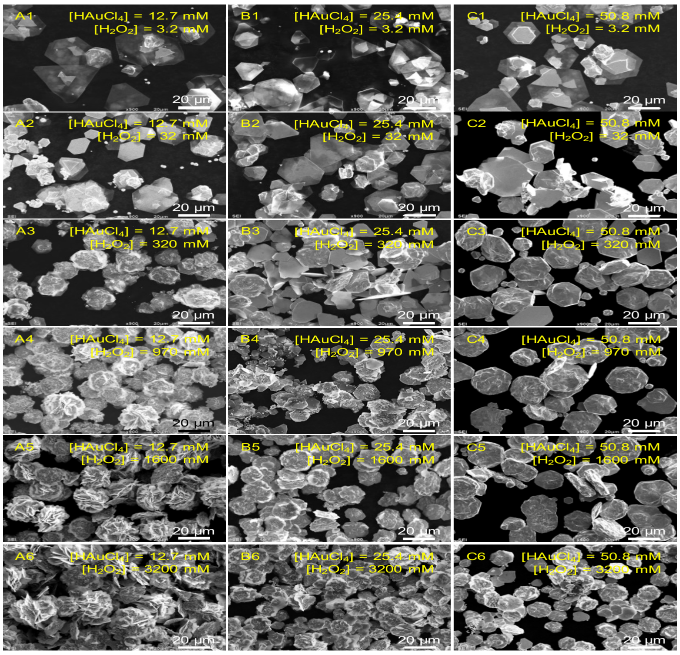

The influence of concentrations of $HAuCl_4$ on the fabrication of 3D-FLGMSs were explored by performing the reaction with 1% w/v starch and 3200 mM H_2O_2 using different concentrations of $HAuCl_4$. At low concentration of $HAuCl_4$ (2.54 mM, Figure 2A1), the 3D-FLGMSs with the average lateral size of 8.2±2.0 μm were produced. At the concentration of $HAuCl_4$ of 12.7 and 25.4 mM, the sufficient concentration of gold ions lead to the extensive growth of 3D-FLGMSs with increased particle sizes to 19.2±3.8 (Figure 2A2) and 17.4±3.7 μm (Figure 2A3), respectively. Surprisingly, the surfaces of the petal became smoother (see Figure 2B1−B3). This is due to the substantial formation of the oxidative etchant (e.g. O_2/Cl^-) which is capable to dissolve unstable crystal facets and leave the stable facets undisturbed. However, when the concentration of $HAuCl_4$ was further increased to 50.8 mM (Figure 2A4), the irregular-shape gold micro/nanosheets with small number of flattened flowers (thick-irregular-shape gold microsheets) and small quasi-microspheres (particle size of 1.0±0.2 μm) were generated due to an insufficient surface protection. The surface passivation of gold nanostructures can be diminished by the acid hydrolysis of long chain starch at high concentration of $HAuCl_4$. The observed phenomena imply that not only the ratio of $[H_2O_2]/[HAuCl_4]$ more than ~60 is required, but also the stabilizing power from starch that are an essential for the formation of the 3D-FLGMSs.

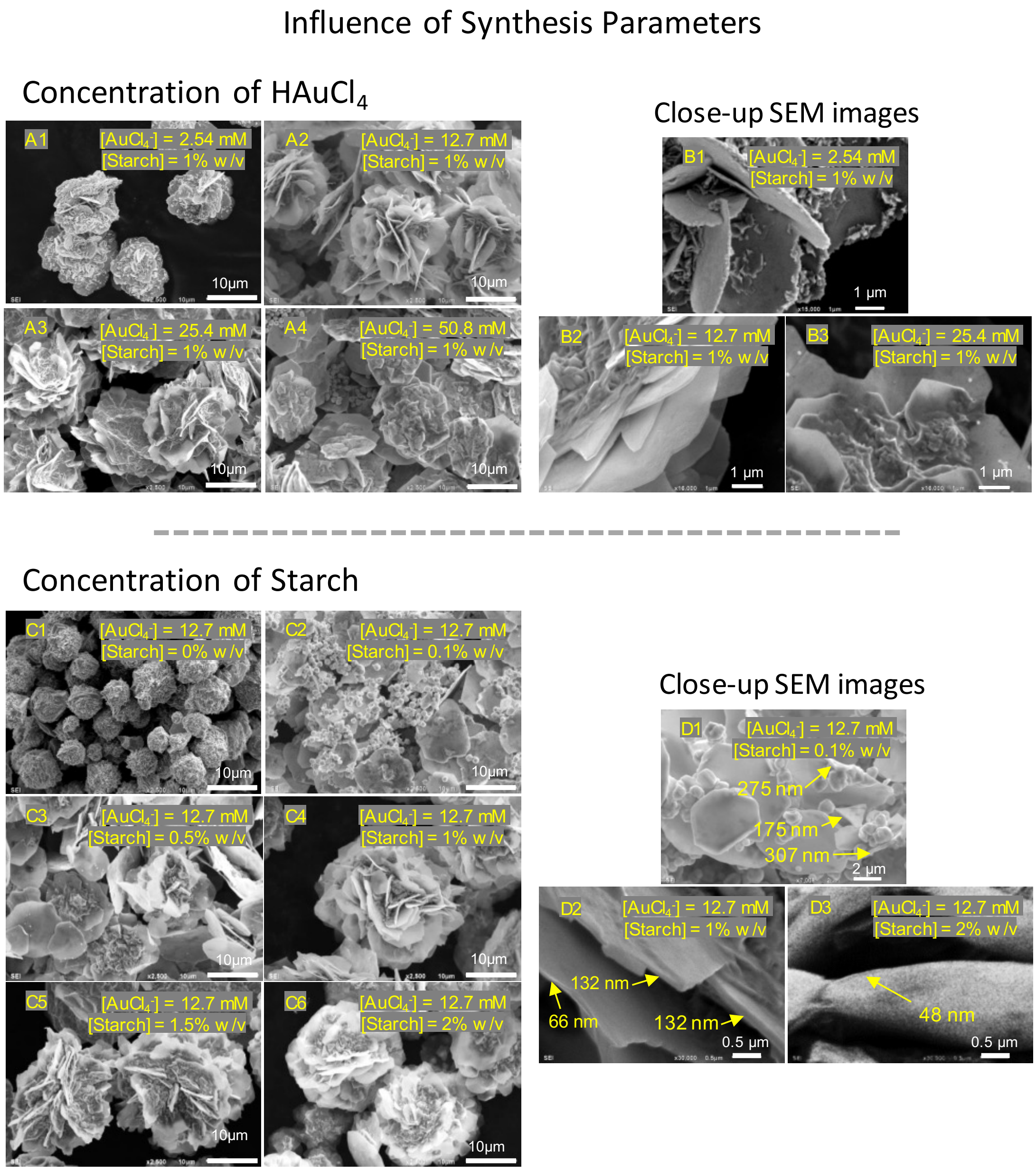

<u>Figure 2</u> *(A1-A4) SEM images show the effect of concentration of $HAuCl_4$ (2.54−50.8 mM) on the gold microstructures with zoomed SEM images (B1-B3) which present the surfaces morphology of 3D-FLGMSs affected by $HAuCl_4$ at 2.54, 12.7 and 25.4 mM, respectively. (C1-C6) SEM images show the effect of concentration of starch (0−2% w/v) on the gold structure with zoomed SEM images (D1-D3) which present the thickness of microplate/petal-like nanostructures of 3D-FLGMSs affected by concentration of starch at 0.1, 1 and 2% w/v, respectively. For all synthesis conditions, 3200 mM of H_2O_2 were used a reducing agent.*

The role of starch passivation power was confirmed by synthesis of 3D-FLGMSs using various concentrations of starch. The concentration of $HAuCl_4$ was fixed at 12.7 mM as the 3D-

FLGMSs with smooth surfaces were obtained by this condition. Without starch (Figure 2C1), quasi-microspheres with rough surfaces (average particle size of 5.0±1.6 μm) were the sole product. As the concentration of starch was increased to 0.1% w/v (Figure 2C2), irregular-shaped gold micro/nanosheets (particle size of 8.9±3.2 μm and thickness of 90-220 nm) and small microspheres (partial size of 1.0±0.2 μm) were produced. When the concentration of starch was increased to 0.5% w/v (Figure 2C3), the enhanced stabilization enables the formation of irregular gold nanosheets with an average size of 10.8±3.6 μm. The observed phenomena imply that an insufficient stabilization causes aggregations of the microspheres and a non-uniform growth on the basal planes of nanosheets. As greater concentrations of starch were employed (1%–2% w/v, Figure 2C4-C6), 3D-FLGMSs with lateral size as large as 30 μm were obtained as the main product. An adequate stabilization of starch induced the structural transformation from the quasi-microspheres and the irregular shaped gold micro/nanosheets to 3D-FLGMSs. This observation indicates that starch is not only an essential factor for the formation and growth of the 3D-FLGMSs, but also preventing the formation of microspheres.

There are several reports describing the role of starch in the formation of anisotropic gold nanostructures. Starch serves as an efficient passivating agent that promotes the formation of gold nanosheet. The selective absorption of starch on the {111} facet of gold nanosheets does not only promote the expansion of the {111} facet, but also regulate the thickness of nanosheets. The decrease of the thickness of nanosheets in 3D-FLGMSs was noticed when starch concentration increased (Figure 2D1-D3). This is due to the increase of passivation power by starch on the surfaces which inhibit the epitaxial growth of nanosheets. Raman spectroscopy was performed to assess the starch residuals on the surfaces of the nanosheets/petals after cleaning with DI water, hot DI water, and alkaline-peroxide solution (i.e., a strong bleaching solution of 30% H_2O_2 adjusted to pH 14 by 3 M NaOH). After washing with cold and hot DI water, starch molecules still remained on the surfaces. However, after cleaning with alkaline peroxide solution, the fingerprint of starch was vanished. This can imply that although starch had a very good adhesion on the surfaces of 3D-FLGMS petals, however, it can be easily removed to obtain the surface-clean 3D-FLGMSs.

As revealed in SEM images, the complex microstructures of 3D-FLGMSs would be constructed from the assembly of nanosheets. Generally, gold nanosheets exhibited the specific {111} facet exposure. The high exposure of {111} crystal facet can be revealed as the extremely high {111} intensity (Figure 3B). Very high values of intensity ratios of {111}/{200} and {111}/{220} suggest that the {111} facet is parallel to the surface of substrate during the XRD characterization (Table 1). In the case of 3D-FLGMSs, the XRD patterns (Figure 3A) clearly indicates the characteristic of the face-centered cubic (fcc) crystal of gold assigning to {111}, {200}, {220}, {311}, and {222} facets which perfectly match the JCPDS 04-0784 standard file (Figure 3). Compared with other facet intensities, the high intensity of {111} facet was noticed which correspond to the highly exposed {111} facet on the obtained structures. It should be noted that the 3D-FLGMSs show lower values of intensity ratio of {111}/{200} and {111}/{220} compared to those of nanosheet structures. This can be attributed the diverse-oriented nanosheets of the 3D-FLGMSs on the surface of substrate during the XRD characterization.

Table 1 *the ratios of {111}/{200} and {111}/{220} of different gold micro/nanostructures.*

Ratio / Structure	{111}/{200}	{111}/{220}
3D-FLGMSs	5.882	5.525
Nanosheets	19.607	27.027

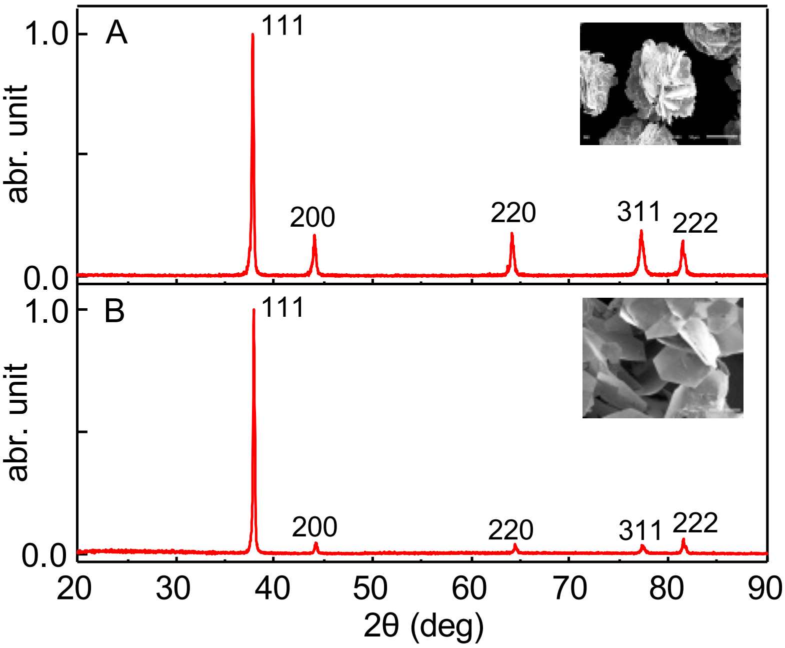

Figure 3. *XRD patterns of (A) 3D-FLGMSs and (B) gold nanosheets. The inset pictures indicate the corresponded SEM images.*

Growth mechanism of 3D-FLGMSs

In our synthesis system, the time-lapse digital photographs revealed the relative fast reaction as indicated by a complete consumption of gold ions within 20 min (i.e., the yellow solution turned colorless) together with the observation of tiny particles (Figure 4A-D). It is evidence that the reduction of Au(III) to Au(I) and Au(III) to Au(0) simultaneously occurs due to the electropositive reaction. After 24 min, the rapid appearances of red-brown suspensions together with a burst of oxygen bubbles represent the rapid formation and growth of 3D-FLGMSs (Figure 4E-K).

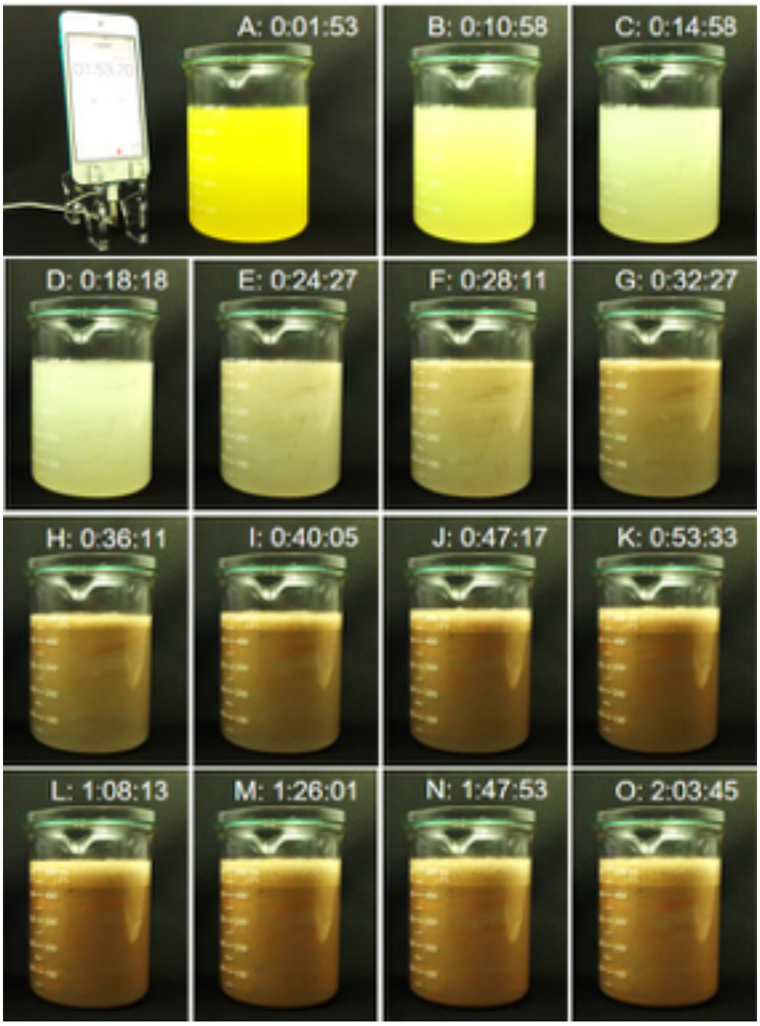

Figure 4 *Time-lapse digital photographs illustrate the progress of the reaction in a 3D-FLGMS synthesis. A demonstration of a large-scale preparation of 3D-FLGMS (500 mL solution with a gold metal content of 2.5 g) was conducted by reduction of 12.7 mM* $HAuCl_4$ *by 3.2 M* H_2O_2 *in 1% (w/v) starch. It should be noted that although the reaction was completed within 120 min, a large number of bubbles was observed due to the decomposition of the remaining* H_2O_2 *on gold surfaces. The pictures were captured by an iPhone 6s with time-lapse function.*

Although the gold ion precursors were completely consumed within first 20 min, the presence of oxygen bubbles was still observed. This observation implies that the reduction of gold ions by H_2O_2 still instantly occurs. The generated gold ions, which serve as metal supply for the growth of 3D-FLGMSs, might be from the dissolution of the unstable crystal facets in 3D-FLGMSs by a strong oxidative species (O_2/Cl^-).

Corroboration to the time-lapse digital photographs, we gained more insight understanding on the growth mechanism of the 3D-FLGMSs by performing time-dependent SEM observations. As shown in Figure 5A-C, the small gold nanosheets formed at the early stage and later grew into larger primary gold nanosheets. The existing of jagged edges in small gold nanosheets (Figure 5A) indicates that the growth of 3D-FLGMSs might involve the crystal growth via oriented attachment (OA) resulting in the lateral expansion of the nanosheets. Meanwhile, the epitaxial growth on the surfaces of former nanosheets could develop into new nanosheets (nanopetals), as shown in Figure 3D. The formation of starch-bound new nanosheets was later outgrowing from the nucleation sites on the basal plan of the former nanosheets (Figure 5E). The development of nanopetals continued until complete structures of 3D-FLGMSs were obtained. The rough surfaces of nanopetals on 3D-FLGMSs can be recognized. They might come from the uncompleted growth of the sheets as the metal ion supply was exhausted.

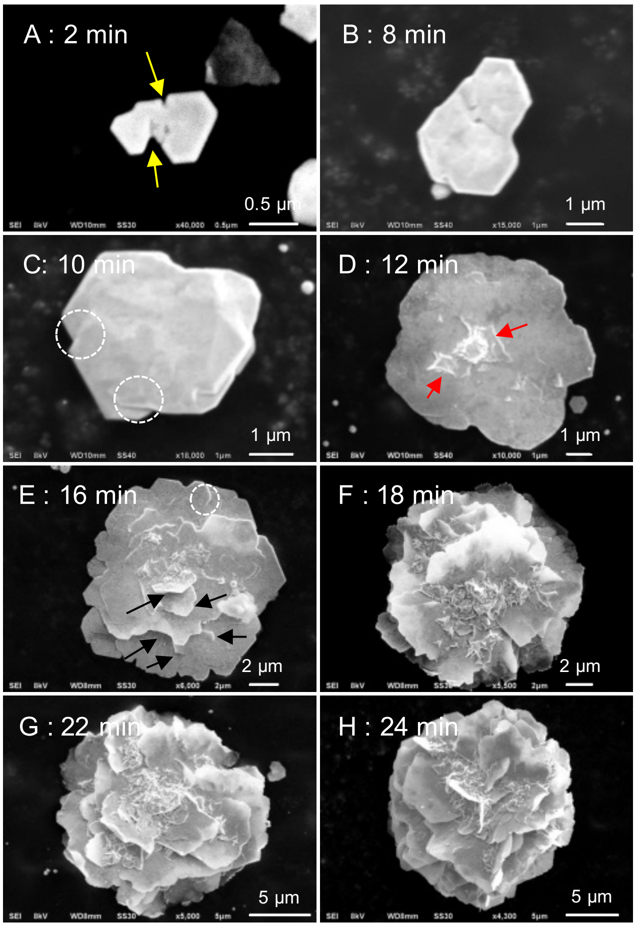

Figure 5 *Time-dependent SEM micrographs show the development of 3D-FLGMSs. The 3D-FLGMSs were synthesized using 25.4 mM* $HAuCl_4$ *and 3200 mM* H_2O_2 *in 1% w/v starch solution. The arrows in (A) indicate jagged edges, those in (D) indicate the epitaxial growth on the basal plan of nanosheets, while those in (E) indicate the petals outgrowth from the surfaces of the basal plan of nanosheets. The circles in (C) and (E) indicate the overlapped parts of nanosheets.*

We further performed HRTEM characterization to acquire the evidence of the formation of 3D-FLGMSs. The 3D-FLGMSs were disassembled to become small fractals of petal-like nanostructures using high power ultrasonication. Figure 6A and 6B show a TEM image and its corresponding SAED pattern of a petal-like nanostructure from 3D-FLGMSs, respectively. The hexagonal diffraction pattern was obtained by projecting the electron beam perpendicular to the basal plane of petal-like nanostructures. Bragg reflections of the Au face-centered cubic (fcc) crystal structure clearly shows the allowed {220} and the forbidden 1/3{422} planes which typically exist with the presence of twinned planes that are parallel to the {111} surfaces of nanoplates or nanosheets. The results suggest that the basal plane of petal-like nanostructures is actually {111} facet. Figure 4C shows the TEM image of a petal-like nanostructures of growing 3D-FLGMSs. HRTEM image with lattice fringe resolution at the edge of the growing nanopetal reveal the lattice fringe of ~2.5Å which correspond to 1/3{422} diffractions obtained from SAED. The stacking faults on the lattice fringe were noticed (Figure 6D). This shows that the growth of nanocrystal undergoes OA process which involves the direct coalescence of nanoparticles. This attachment provides the defects in the crystal structure, including twin, stacking faults and misorientation, which is possible to be preserved in the following growth process. Furthermore, the presence of strong surface adsorption by starch during the growth can promote OA in the initial growth state. Thus, the observations of the stacking faults in the nanopetals suggest that the growth of 3D-FLGMSs mainly involves the OA mechanism.

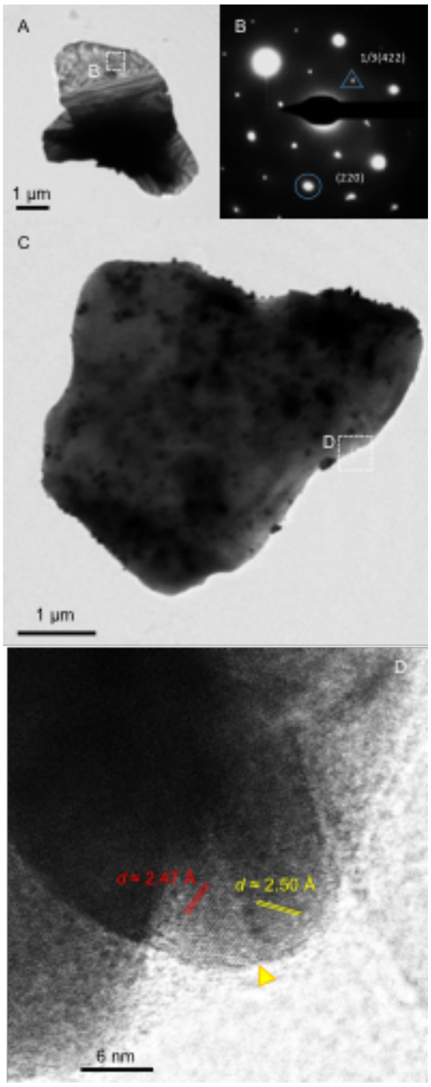

Figure 6 *(A) and (C) TEM images of small petal-like nanostructures of 3D-FLGMSs and growing 3D-FLGMSs, respectively. (B) The corresponding SAED pattern in (A). (D) HRTEM image with lattice fringe resolution at the edge of growing petal-like nanofractals of 3D-FLGMSs. The yellow arrowhead indicates the stacking faults.*

Based on the observed evidences from time-dependent study and time-lapse digital captures, we propose the growth mechanism of 3D-FLGMSs as shown in Figure 7. At the very early step, gold ions are rapidly reduced by H_2O_2 and subsequently grow to small gold nanosheets with starch-bounded surfaces. The massive generation of gold nanosheets, which is caused by employing of high concentration of metal precursor and reducing agent (H_2O_2), leads to the rise of total surface energy in the system. To minimize the overall surface energy, gold nanosheets undergo OA to form the large primary gold nanosheets preserving its lowest surface energy {111} facet. In addition, the crystalline boundaries (defects) created from the imperfect OA could act as active sites for heterogeneous growth. With an assistance of starch passivation, the new nanopetals could grow on former nanosheets. Alternative dissolution process of the nanosheets was also occurred by oxidative etching mechanism on the unstable facets of nanosheets. This process generates the gold ions to the system, but at the same time, they are also consequently used for the growth process. After the increased number of nanopetals, the formation of the complete structures of 3D-FLGMS is finally achieved.

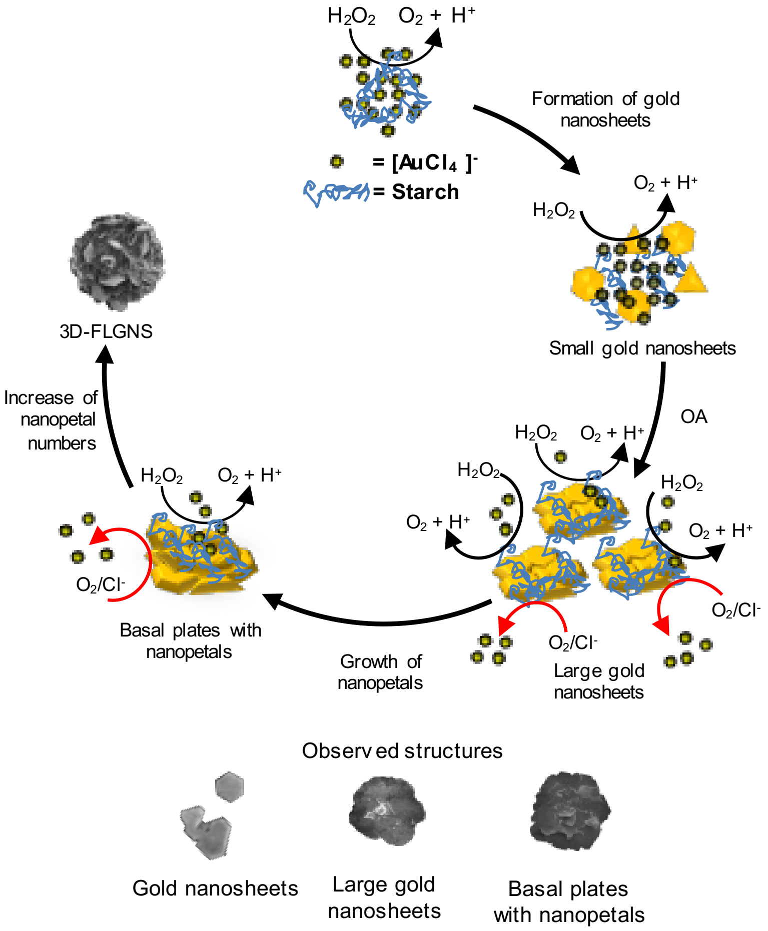

<u>Figure 7</u> *Scheme represents the proposed growth mechanism of 3D-FLGMS. Black arrows indicate the growing of 3D-FLGMS while red arrows present the etching process of 3D-FLGMS by* O_2/Cl^-.

SERS Activity on 3D-FLGMS

As discussed in the previous sections, the facile method for the fabrication of 3D-FLGMSs has been demonstrated. The developed method provides a 100% conversion of gold ions with good reproduced structures. Moreover, we further demonstrate potential applications of 3D-FLGMSs. There has been reported that the complex nanostructures, in particular dendrite structures, can be used as potential SERS substrates as their sharp corners, edges, and nanometre-scale junctions could create SERS hot spots. Due to the complex morphologies of 3D-FLGMSs, thus, we interest to explore the application of 3D-FLGMSs as a SERS substrate. 3D-FLGMSs exhibits not only the micrometre-size complex morphology but the great advantages as it can be easily handle under microscope as the sensing region can be precisely determined. Moreover, only small volume in sub-microliter range of the target analyte is required to be used in the detection. To investigate the SERS activity, 3D-FLGMSs were cleaned with an alkaline-peroxide solution to achieve starch-free surfaces. The aqueous-dispersed 3D-FLGMSs were dropped on aluminium-coated glass substrates. After drying in a desiccator for 24 h, Rhodamine 6G (R6G) with various concentrations (1 nM – 10 µM) were dropped on 3D-FLGMSs and dried at room temperature. A 10 µM of R6G on aluminium foil was used as a reference. SERS spectra were recorded using the excitation wavelength at 532 nm with the laser power of 1 mW, while the exposure time and the number exposure were fixed at 1 msec with 32 scans, respectively.

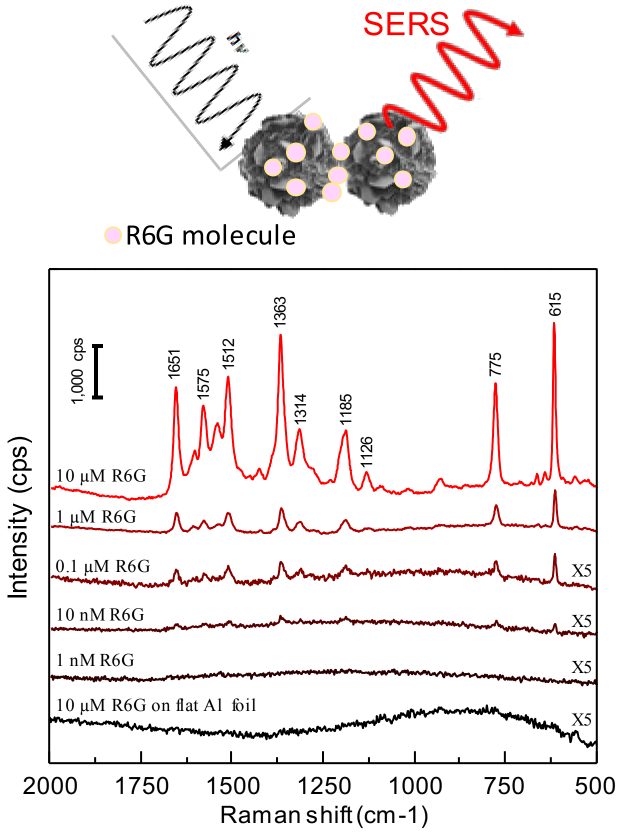

Figure 8 *SERS spectra of R6G, with different concentrations, deposited on the surfaces of 3D-FLGMS and Raman spectrum of R6G deposited on flat aluminum foil with an inset schematic illustrate the SERS of R6G on surfaces of 3D-FLGMS.*

Figure 8 shows the SERS spectra of R6G on flat aluminium substrates. Without 3D-FLGMSs, Raman signal of 10 μM R6G cannot be observed. Meanwhile, the well-defined vibrational fingerprints of R6G, which comprise of C-C-C in-plane bending (615 cm^{-1}), C-H out-of-plane bending (775 cm^{-1}), C-H in-plane bending (1126 and 1185 cm^{-1}), C-O-C stretching (1314 cm^{-1}), and C-C stretching of aromatic ring (1363, 1512, 1575, and 1651 cm^{-1}), were clearly observed from the SERS spectra of R6G deposited on 3D-FLGMSs. A further investigation was conducted in order to explore the lowest concentration of R6G that can be detected when using 3D-FLGMSs as SERS substrates. The SERS signal at 615 cm^{-1} was employed as it showed distinct feature with the highest intensity. The Raman shift at 615 cm^{-1} was observed even the concentration of R6G is as low as 100 nM. In addition, SERS activity of material depends on the number of hot spots in a specific surface area. Although Brunauer–Emmett–Teller (BET) analysis on our 3D-FLGMSs revealed that surface area is rather low (0.51 $m^2 \cdot g^{-1}$) but the enhancement of the Raman signal of R6G on the 3D-FLGMS could be attributed to the SERS hot spots created by the overlapping of the petal-like structures between the two flowers, the 3D nanogaps located between adjacent nanosheets and the nanometre-scale surface roughness. This

Conclusions

In summary, we have successfully developed a simple and efficient synthetic method for the fabrication of 3D-FLGMSs using H_2O_2 as the green reducing agent and starch as the stabilizer. The influence of the H_2O_2 and starch on the size, morphology and structural evolution of 3D-FLGMSs were systematically investigated. Shape evolution of 3D-FLGMSs using the green chemicals was revealed. By performing the synthesis at high concentration of H_2O_2, the formation of 3D-FLGMSs with the size as large as 30 μm can be achieved in a short period. Adequate amount of starch is essential for the formation of 3D-FLGMSs as it functions as a surface-passivating agent while promoting the growth of nanopetals. An insufficient stabilization leads to the formation of flat 3D-FLGMSs with large number of quasi-microspheres. Based on time-dependent study, the growth of 3D-FLGMSs involved the formation of gold nanosheets, self-assembly of gold nanosheets via OA, and epitaxial growth on the surfaces of gold nanosheets. The preliminary investigation on the application of 3D-FLGMSs as SERS substrates suggests that 3D-FLGMSs can be used as efficient SERS substrates.

Future works

The 3D-FLGMS can be used as a powerful SERS substrate. Therefore, it possible to apply the 3D-FLGMS as SERS substrate to enhance Raman signals of protein, DNA, RNA and other biomolecules in order to differentiate types of biomolecules and also quantify amount of the molecules.

งานวิจัยชิ้นที่ 2

Phase Transferring of Silver Nanoparticles to Organic Solvents using Modified Graphene Oxide as Carrier

In this work, we developed a simple, non-toxic, cost-effective, quick and environmentally friendly synthesis approach to fabricate graphene oxide based composite with silver nanoparticle (GO/AgNP) and the powerful protocol to modify them to form stable suspensions which can be well-dispersed in several organic solvents. Scheme 1 shows the overall protocol to transfer AgNPs into organic solvents using GO as a carrier.

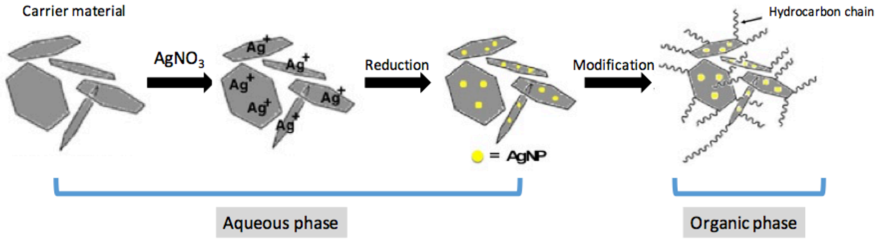

<u>Scheme 1</u> *the overall protocol to transfer AgNPs into organic solvents using GO as a carrier.*

The existence of AgNP on GO nanosheets was examined by several techniques such as UV-Vis spectroscopy, XRD, TGA, and TEM. Furthermore, the stability of AgNP decorated on GO was evaluated by the bath sonication. A hydrophobicity of the composites was increased using a primary amine with long hydrocarbon chain, oleylamine (OAm), to modify the surface of the GO/AgNP composites. The dispersion behavior and the stability of the modified GO/AgNPs in six organic solvents (e.g. toluene, *n*-butanol, iso-butyl acetate, ethyl acetate, acetonitrile, and ethylene glycol) were also investigated.

Preparation of GO/AgNP composites

The stock solution of 1,500 ppm $AgNO_3$ was prepared by dissolving 0.0778 g of $AgNO_3$ in 50 mL of DI water. 200 ppm of graphene oxide (GO) suspension was prepared by mixing 2.5 mL of GO suspension in 22.5 mL of DI water. The synthesis of GO/AgNP composites was performed by mixing 25 mL of the prepared 200 ppm GO with 25 mL of the stock solution of $AgNO_3$ and then immediately poured in 100 mL of DMF. The mixed solution was stirred and heated in sand bath with controlled temperature at 130-150 °C for 2 hrs. The reaction was incubated under ambient conditions until it cool down to the room temperature. The obtained GO/AgNP suspensions were then centrifuged at 5,000 rpm for 20 min and then washed the colloids of GO/AgNPs by DI water for several times in order to remove the excess silver ions (Ag^+) and DMF. The obtained GO/AgNP composites were dried at 60 °C for 3 hrs. The existence of silver nanoparticles (AgNPs) on GO were characterized by UV-Vis spectroscopy, transmission electron microscopy, X-ray diffraction and thermal gravitation analysis.

Preparation of GO-OAm and GO/AgNP-OAm

Oleylamine was used as a phase transferring agent to transfer GO into organic solvents. To transfer GO into organic solvents, the dried suspension of 200 ppm GO was modified by adding the oleylamine. The modified GO-OAm was then dispersed in organic solvents by sonication process. The various amounts of OAm was performed in order to determine the optimized condition for transferring GO in organic solvents. After obtaining the optimized amount of OAm, the appropriate amount of OAm was added to 2 mg of the GO/AgNP composites. The mixture was sonicated by bath sonication for 2 min to generate GO/AgNPs-OAm. To examine the dispersion behavior, the GO/AgNPs-OAm was dispersed in 5 mL of organic solvents; TOL, *n*-BuOH, *i*-BuOAc, EtOAc, ACN and EG with bath sonication (Elmasonic Model: P30H) for 1 hr, the GO/AgNPs-OAm was well suspended in organic solvents affording the formation of uniformed dispersed gray colloids.

Results and Discussions

The preparation of GO/AgNP composites

A preliminary investigation of the formation of the silver nanoparticles (AgNPs) using DMF as a reducing agent were carried out using UV-Vis spectroscopy. The reduction reaction using DMF as a reducing agent is shown below.

$$HCON(CH_3)_2 + 2Ag^+ + H_2O \xrightarrow{130\text{-}150\ ^\circ C} 2Ag^0 + CO_2 + (CH_3)_2NH + 2H^+ \quad \text{……. (1)}$$

The UV-Vis spectra of the reaction were monitored for 3 hours as shown in Fig. 1A. The appearance of characteristic localized surface Plasmon resonance band (LSPR) at ~430 nm indicates the formation of AgNPs generated since the reaction was prolonged for 1 hr. However, there was no visibly observable of the LSPR band after 3 hrs without any sufficient stabilizer, this observation might relate to the indications of sedimentation, aggregation and agglomeration of the generated AgNPs.

Next, graphene oxide (GO) nanosheets permeated with silver nanoparticles (AgNPs) were synthesized using DMF as a reducing agent. The prepared GO/AgNP composites were purified by centrifugation and washed with DI water for several times. The investigation of the formation of the AgNPs on GO sheet was carried out by several techniques. The UV-Vis spectra of the GO/AgNP composite compared with the bare GO suspensions is shown in Fig. 1B. The appearance of characteristic LSPR band at ~ 430 nm indicates the formation of AgNPs on GO nanosheet. On the other hand, only baseline shift without any characteristic peak was observed from the bare GO suspensions. Moreover, the stability of the deposited AgNPs on the GO nanosheet was also examined. The suspension of the GO/AgNP composites were strongly sonicated for 30 min. and then were centrifuged at 2,000 rpm for 10 min. Due to the centrifuge power, only the suspension of the GO/AgNP composites will be precipitated, while individual AgNPs still be dispersed in the supernatant. UV-Vis spectrum of the supernatant shows only baseline shift without any characteristic LSPR peaks of AgNPs. This suggests that AgNPs were strongly attached on GO sheets and were not detached from GO sheets by sonication process.

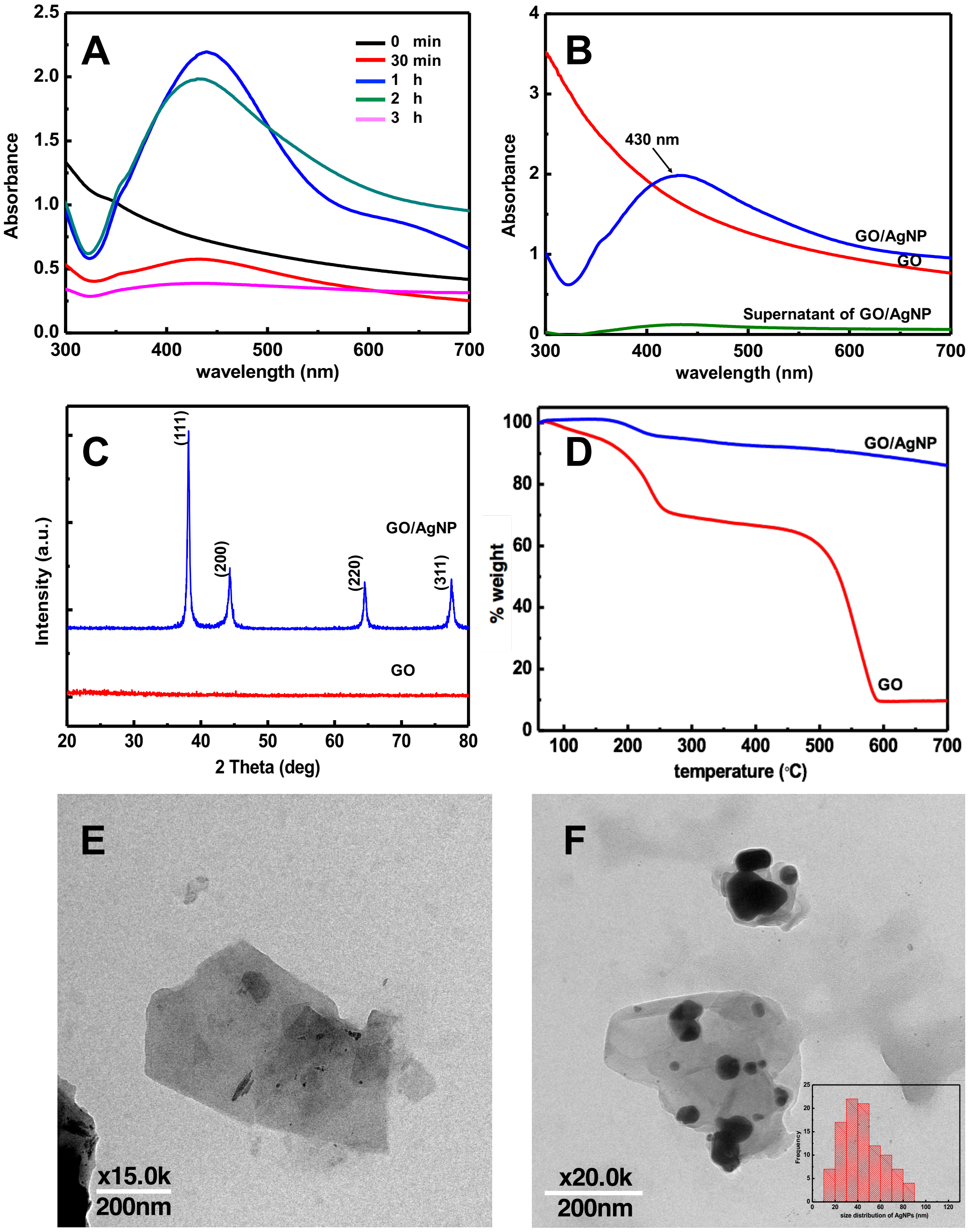

Figure. 1 *(A) UV-Vis spectra of the formation of AgNPs reduced by DMF with the reaction time 30 min, 1 hr, 2 hrs and 3 hrs. (B) UV-Vis spectra of the GO suspensions, the GO/AgNP composites and the supernatant of the GO/AgNP composite solution. (C) XRD patterns of the synthesized GO/AgNP composites compared with the GO suspensions, (D) TGA thermograms of GO and the GO/AgNP composites and TEM images of (E) GO suspensions and (F) the GO/AgNP composites including inset figure of size distribution of AgNPs.*

The purity of the AgNPs deposited on GO nanosheet is further examined by XRD analysis. The XRD patterns of the GO/AgNP composites are shown in Fig. 1C. The prominent peaks at 2θ values of 38.2°, 44.3°, 64.5° and 77.5° are assigned to the (111), (200), (220) and (311), respectively corresponding to crystalline planes of the face centered cubic (fcc) of metallic Ag (JCPDS no. 65-2871). The high intense diffraction peak observed at 38.2^{o}, corresponding to the crystalline Ag, represent that the nanoparticles are composed of pure crystalline Ag.

The level of deposition of AgNP on GO nanosheets was assessed by the thermal gravimetric analysis (TGA) under N_2 environment. The weight ratio of AgNP on GO nanosheets was evaluated by TGA thermograms of weight loss as a function of temperature. The TGA analysis curves of the GO suspension and GO/AgNP composite are shown in Fig. 1D. TGA thermogram of GO suspension shows two weight loss profiles at 150-250 °C and 480-500 °C. The weight loss profile (~20%) at 150-250 °C relates to the evaporation of the absorbed water molecules on GO surface while weight loss (~40%) at 480-500 °C was from the decomposition of oxygen-containing functional groups. However, TGA thermogram of GO/AgNP composites shows higher thermal stability. Only weight loss profile at 150-250 °C due to evaporated water was observed with only 5%. This smaller relative weight loss percentage suggests that there are enormous existed AgNPs on GO sheet. There is no weight loss profile at 500 °C. This phenomenon might relate to the strong interaction between oxygen functional groups and the generated AgNPs. Correspondingly, the anchoring amount of AgNPs on the GO sheet was approximately 80 wt% comparing to the bare GO sheet.

Fig. 1E shows the TEM images of a single layer GO nanosheet which was in form of flat layer with lateral size (~ 500 nm). On the other hand, the AgNPs represented by dark spots are homogeneously assembled on the sub-micro scale GO which were clearly noticed from TEM images of the GO/AgNP composites (Fig. 1F). The strong corrugation of GO surface after deposition of AgNPs with a serious aggregation was observed. This phenomenon evidently induces the aggregation of silver particles. In addition, the TEM images indicate that the average size of AgNPs is approximately 45 nm counted from 100 individual particles with a spherical geometry.

Phase transferring of graphene oxide

Generally, colloids of GO are well dispersed in water media. To transferring GO into organic media, improving the hydrophobic property of GO surface might be required. In this work, oleylamine (OAm) which was a primary amine with the long chain hydrocarbon ($C_{18}H_{35}NH_2$) was used as a phase transferring agent to transfer GO into organic media. Electrostatic interaction between oxygen rich functional groups on GO nanosheets and amine group of OAm were easily occurred. These strong interactions between GO and OAm (GO-OAm) was examined by the FT-IR spectral analysis as shown in Fig. 2A. The set of characteristic peaks of GO represents at ~3250 cm^{-1} (O-H stretching vibrations), at 1720 cm^{-1} (C=O stretching vibrations), at ~1610 cm^{-1}

(aromatic C=C stretching vibrations), and at ~1070 cm^{-1} (C-O-C stretching vibrations). The FT-IR spectra of OAm and GO-OAm show the strong intensity absorption band at ~2920 cm^{-1} and 2850 cm^{-1} corresponding to the C-H aliphatic stretching vibrations and the amine group (N-H) at ~1465 cm^{-1}. These observations confirm the interaction between amine group of OAm with the functional groups on GO sheet.

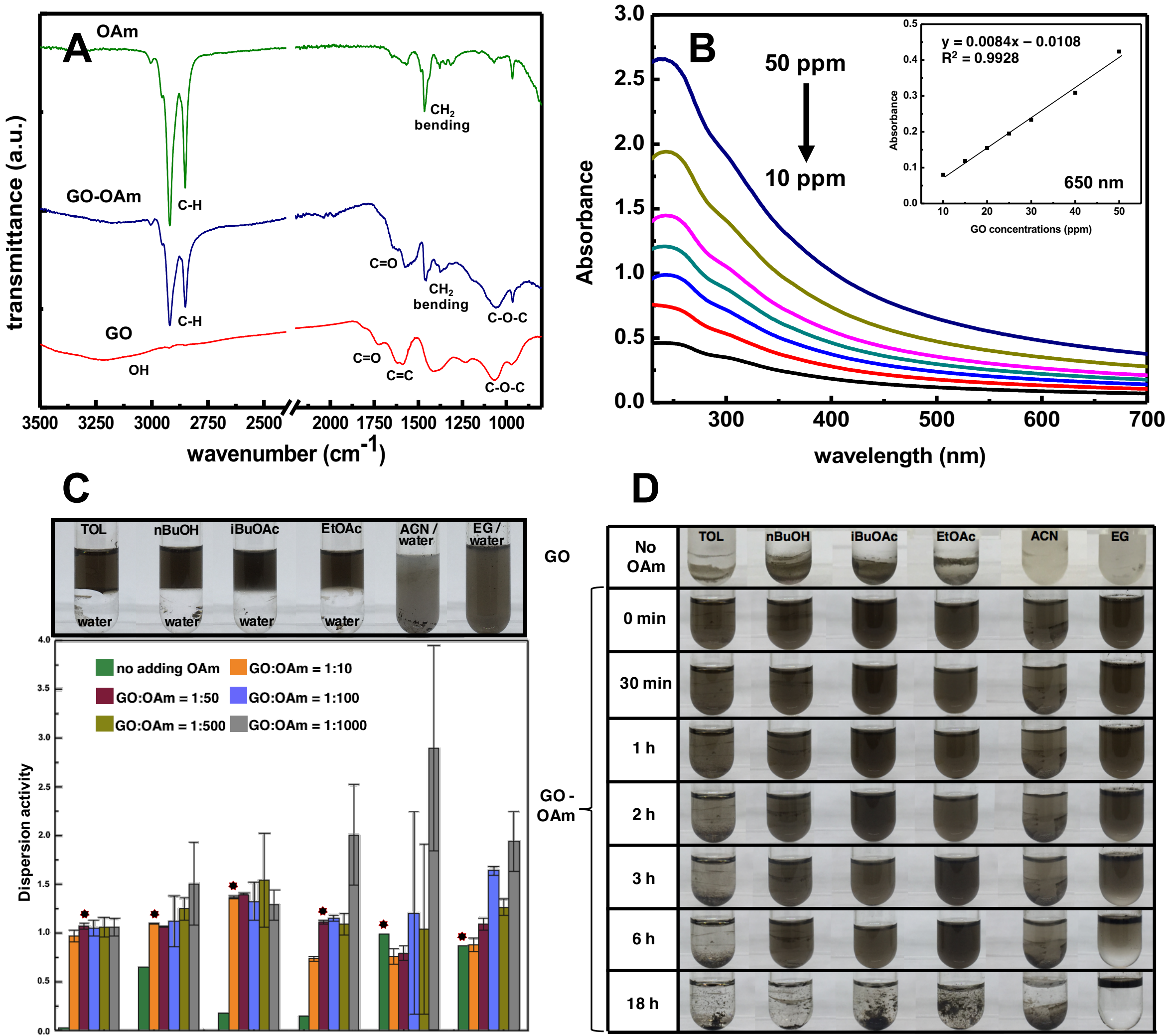

Figure. 2 *(A) FT-IR spectra of the GO, GO-OAm and OAm (B) UV-Vis spectra of the GO suspension with various concentrations (10 ppm to 50 ppm) with the inset image which displays the calibration curve constructed by collecting absorbance at 650 nm. vs. GO concentrations. (C) the dispersion activity of GO-OAm using various amounts of OAm in organic solvents. An appropriate amount of OAm used to transfer GO into organic solvents was marked with star symbol (*). (D) Digital images represent the dispersed GO and GO-OAm in several organic solvents immediately after sonication and after leaving them for 0-18 hours.*

Prior to study the dispersion behavior of GO-OAm in organic solvents, the dispersive efficiency of the GO suspension in water was preliminary investigated by using UV-Vis spectroscopy. The UV-Vis spectra of various concentrations (10 ppm to 50 ppm) of the GO suspensions in water were collected as shown in Fig. 2B. It can be seen there is no specific band on UV-visible spectra of GO colloidal solution but the background intensity was linearly related to the concentration of GO. The higher concentration of GO, the higher background intensity appears. An inset on Fig. 2B shows a calibration line with $R^2 > 0.99$ constructed by measuring the absorbance at 650 nm of GO colloidal solutions at different concentrations. This calibration curve was used as standard index to calculate dispersive efficiency of the GO-OAm in organic solvents.

To study the dispersion behavior of the GO-OAm in organic media, the complex of GO-OAm was distributed in different organic solvents (TOL, *n*-BuOH, *i*-BuOAc, EtOAc, ACN and EG). The variation of the dispersion behavior might be related to the compatibility of solvents (dipole moments, polarity, and surface tensions as shown in ESI table S1) and the hydrophobicity of the GO-OAm [27]. Therefore, the optimization of amount of OAm might be required in order to assess the maximum dispersion of GO in organic solvents. To reach an appropriate amount of OAm used to transfer GO into organic solvent, a dispersion activity calculated from the ratio of A'_{650} / A_{650}, where A'_{650} and A_{650} are the absorbance at 650 nm of GO-OAm dispersed in organic solvents and GO dispersed in water , respectively.

To optimize amount of OAm used to transfer GO into organic solvents, the weight ratios of GO:OAm were varied at 1:10, 1:50, 1:100, 1:500 and 1:1000, respectively. Fig. 2C shows the dispersion activity of GO-OAm using various amount of OAm in several organic solvents. The small index of dispersion activity represents a small proportion of GO that can be transferred to organic solvents. This reflects an insufficient of OAm for transferring GO into organic solvents. However, the high value of the dispersion activity with a large variation is observed when the larger amount of OAm was used. This observation might be originated from an excess amount of OAm which induces the aggregation/agglomeration of GO to form a multilayer GO sheets due to the hydrophobicity of long chain hydrocarbon on OAm molecules. Therefore, a suitable amount of OAm should be determined by giving dispersion activity of GO-OAm close to 1 with less variation. This means the dispersion behavior of GO-OAm in organic solvent is similar to the starting GO suspensions in water. In each organic solvent, an appropriate amount of OAm was determined (marking with star symbol). Inset of Fig. 2C displays the digital photographs of the dispersed GO-OAm taken in several organic solvents immediately after the sonication. To determine the degree of sedimentation, the digital images were again taken in the range of 0 – 18 hours. After sonication, the GO-OAm using an appropriate amount of OAm showed very good dispersion in all solvents: TOL, *n*-BuOH, *i*-BuOAc, EtOAc, ACN and EG. The water was added in order to separate organic phase and water phase. In case of CAN and EG, these solvents are homogenously soluble with water. The long-term stability was examined by leaving the suspensions undisturbed for 18 hours. The results clearly displayed that the starting GO was completely not dispersed in any organic solvents, while GO-OAm retained its excellent dispersibility in especially *n*-BuOH, *i*-BuOAc, EtOAc for at least 6 hours. In case of TOL, a precipitation of GO-OAm was observed after 2 hrs. The long-term stability of the GO-OAm might be majorly related to the polarity of the solvents where TOL provides the lowest polarity in the case. It is worth mentioning that the stability of the dispersion GO-OAm for 6 hours might adequate for the industrial and research applications. Moreover, the precipitated GO-OAm can be re-dispersed by bath sonication (Fig. 3) which is practically used in the industrial/manufacturing.

Figure 3 *: Redispersibility of GO/AgNP-OAm in organic solvents*

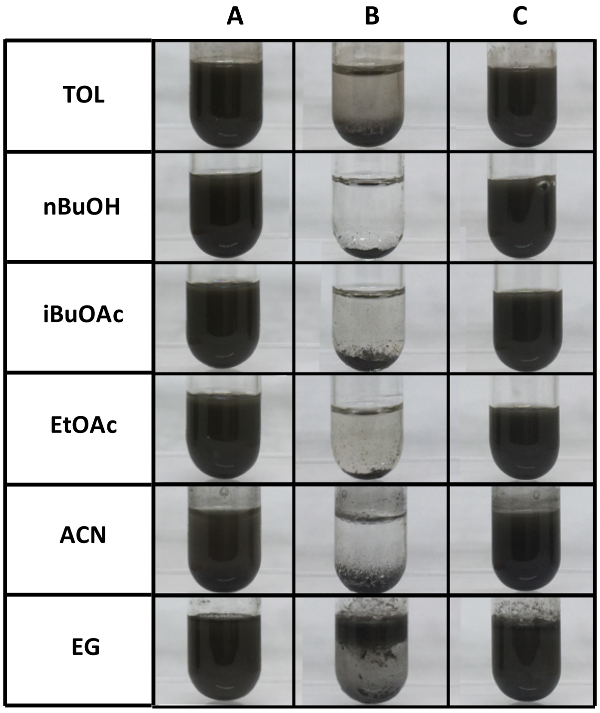

column A*: GO/AgNP-OAm was dispersed in organic solvents after sonication.*
column B*: GO/AgNP-OAm was dispersed in organic solvents for 18 hours.*
column C*: GO/AgNP-OAm was re-sonicated in organic solvents again after leaving for 18 hours.*

Phase transfer of graphene oxide-silver nanoparticle (GO/AgNP) composite

The transferring process for GO by using OAm as transferring agent was performed with the GO/AgNP composites. In our case, the AgNPs cannot be directly transferred into organic solvents using OAm as shown in ESI Fig S2. The optimized amount of OAm in each organic solvent was used to increase hydrophobicity of GO surface of the GO/AgNP composites and produce the GO/AgNPs-OAm. The presence of AgNPs on the GO/AgNPs-OAm in the organic solvents was investigated by UV-Visible spectroscopy as shown in Fig. 4A. The characteristic Plasmon bands of AgNPs at ~430 nm is clearly detected in all solvents. It should be noted that the dispersive efficiency of the GO/AgNPs-OAm might be different due to the solvent properties. This causes on the variation of baseline shifts in UV-Vis spectra. The decomposition profiles of GO-OAm and GO/AgNPs-OAm were assessed by the thermal gravimetric analysis (TGA) under N_2 environment. Fig. 4B shows the TGA thermograms of weight loss as a function of temperature. The TGA curves of GO-OAm and GO/AgNPs-OAm were also observed the weight loss profiles at 350-450 °C corresponding to the desorption of the range of C_1-C_3 hydrocarbon fragments. These fragments were referred to amine fragments; $C_1NH_2^+$ and $C_2NH_2^+$ of the OAm molecules. The anchoring amount of AgNPs on the GO nanosheets was approximately 35 wt% comparing to the GO-OAm. In addition, the digital images of the GO/AgNPs-OAm suspension in the organic solvents are shown in an inset of Fig. 3C. From the digital images, they are observed that the GO/AgNPs-OAm is well-dispersed in all organic solvents.

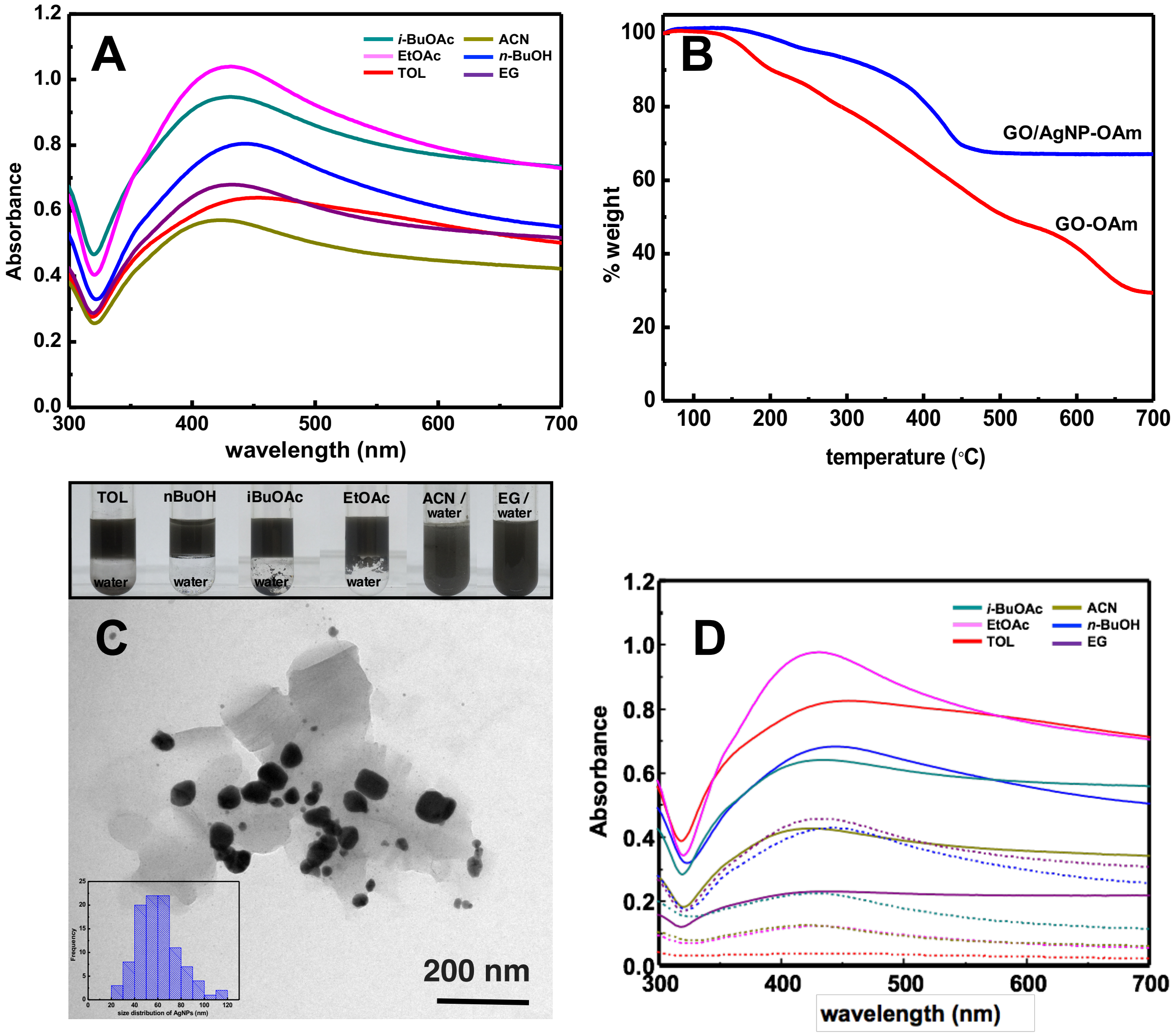

Figure. 4 *(A) UV-Vis spectra of the dispersion of the GO/AgNP-OAm in the organic solvents. (B) TGA thermograms of GO-OAm and the GO/AgNP-OAm. (C) TEM images of GO/AgNP-OAm in ethyl acetate (EtOAc) with the photographs represents the GO/AgNP-OAm suspension in several organic solvents immediately after sonication and (D) UV-Vis spectra of the dispersion of the GO/AgNP-OAm pellet in organic solvents (solid lines) and the normalized supernatant of GO/AgNP-OAm composites (dot lines).*

To assess the morphology, the GO/AgNP-OAm in EtOAc was investigated by TEM as shown in Fig 4C. It can be seen that the AgNPs still remain on GO nanosheets after transferring to the organic solvent. However, these particles seem to be disaggregated with the unfolding of GO nanosheets. The unfolding mechanism of GO sheets might be induced by the increasing of the hydrophobicity of GO nanosheets from long hydrocarbon chain of OA. From the observation on TEM images, AgNPs might be detached from an unfolded GO nanosheets. To test the stability of the AgNPs deposited on the transferred GO/AgNPs-OAm, the suspension of GO/AgNPs-OAm in organic solvents was sonicated and then followed by centrifuging at 2,000 rpm for 10 min. The supernatant was collected for analyzing while the sediment pellets were re-dispersed in the organic solvents. These two fractions were analyzed by UV-Vis spectroscopy. Fig. 4D shows UV-Vis spectra of the supernatant (dot lines) and re-dispersed GO/AgNPs-OAm (solid line). It can be seen that the absorbance of supernatant was mostly lower than the re-dispersed GO/AgNPs-OAm in TOL, n-BuOH, i-BuOAc, EtOAc and ACN. These observations suggest that AgNPs were still remained on GO sheets. However, the Plasmon band of AgNPs (~ 430 nm) was observed in the the supernatant from n-BuOH, EtOAc and i-BuOAc. This suggests that the fractional AgNPs on the GO/AgNPs-OAm were partially detached by sonication process.

After phase transferring, XRD measurements were performed to monitor the stability of AgNP on GO sheets after storing for 6 months (Sep 2016-May 2017). The diffraction patterns of the GO/AgNP-OAm in toluene after storing for 6 months and the fresh GO/AgNP-OAm are shown in Fig. 5. It can be seen that XRD patterns are not changed and still in a good agreement with a standard XRD patterns of the pure Ag (JCPDS no. 65-2871). This suggests that the AgNPs on the GO sheet are very stable even when they had been stored for 6 months.

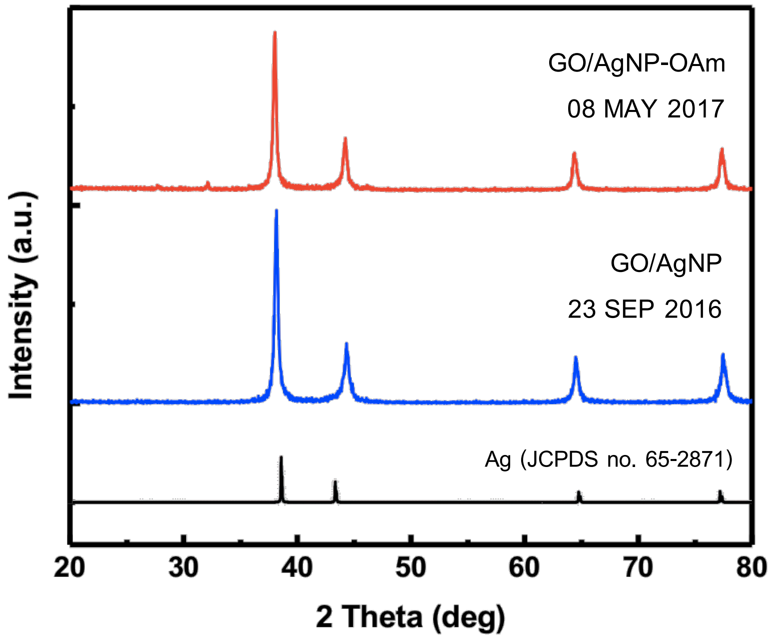

Figure 5 *: The diffraction patterns of the GO/AgNP-OAm in toluene after storing for 6 months (Sep 2016-May 2017) and the fresh GO/AgNP-OAm*

Conclusions

We successfully developed the phase transferring process to transfer the AgNPs into the organic solvents by using GO as a carrier material. The process carries out only two steps: the formation of AgNPs on GO surface through chemical reaction by using DMF as a reducing agent, and then the GO/AgNP composites were modified its surface by oleylamine to increase the hydrophobicity of the composites. The AgNPs were uniformly generated and assembled on a surface of GO sheets with highly stability according to the strong interaction between tremendous oxygen-functional groups on GO and the AgNP particle. These AgNP particles on GO sheet cannot be detached by an ultrasonic. The modified GO/AgNP with oleylamine to form GO/AgNP-OAm is highly dispersed in the organic solvents for at least 6 hours. However, the sediments of GO/AgNP-OAm can be re-dispersed using ultrasonic without any detraction of AgNPs. This developed phase transfer method opens an alternative way to transfer AgNPs into organic solvents with simplicity and high efficiency, moreover, it suitable to be scaled up for the industrial applications.

Future works

Due to the synthesis protocol, the applications of those AgNPs was not imited to the industrial and commercial products using water-based solvent. Our purposed protocol of transferring AgNPs into organic solvents were successfully developed. These particles are well-dispersed in organic solvents. This opens-up a new window of applications in polymers, coating materials and textiles which might require organic solvents as a media. These materials can be functionalized to be appropriate to tremendous applications in several practical fields including nanomedicide as antibacterial agents, catalysis as a promising heterogeneous catalyst, energy as a component in Li batteries, electronic, optical sensors, and environmental applications.

เอกสารแนบหมายเลข 3

Output จากโครงการวิจัยที่ได้รับทุนจาก สกว.

1. ผลงานตีพิมพ์ในวารสารวิชาการนานาชาติ (ระบุชื่อผู้แต่ง ชื่อเรื่อง ชื่อวารสาร ปี เล่มที่ เลขที่ และหน้า) หรือผลงานตามที่คาดไว้ในสัญญาโครงการ

งานวิจัยทั้งสองชิ้นนี้ได้รับการตีพิมพ์ในวารสารวิชาการระดับนานาชาติ โดยหัวหน้าโครงการวิจัยเป็นผู้รับผิดชอบผลงาน (corresponding author) ดังนี้
(manuscript ฉบับเต็มอยู่ในภาคผนวกของรายงานฉบับสมบูรณ์)

1.1) S. Nootchanat, C. Lertvachirapaiboon, V. Amornkitbamrung, P. Uppachai, S. Ekgasit, **K. Wongravee*** “Shape evolution of 3D flower-like gold microstructures from gold nanosheets via oriented attachment” *Materials & Design*, **2017**, 125, 158-166. (Impact factor = 4.364)

1.2) O. Wong-u-ra, S. Ekgasit, **K. Wongravee*** “Phase transferring of silver nanoparticles to organic solvents using modified graphene oxide as carrier” *Materials Chemistry and Physics*, **2017**, 199, 348-355. (Impact factor = 2.084)

2. การนำผลงานวิจัยไปใช้ประโยชน์
   - เชิงพาณิชย์ (มีการนำไปผลิต/ขาย/ก่อให้เกิดรายได้ หรือมีการนำไปประยุกต์ใช้โดยภาคธุรกิจ/บุคคลทั่วไป)
     ไม่มี
   - เชิงนโยบาย (มีการกำหนดนโยบายอิงงานวิจัย/เกิดมาตรการใหม่/เปลี่ยนแปลงระเบียบข้อบังคับหรือวิธีทำงาน)
     ไม่มี
   - เชิงสาธารณะ (มีเครือข่ายความร่วมมือ/สร้างกระแสความสนใจในวงกว้าง)
     ไม่มี
   - เชิงวิชาการ (มีการพัฒนาการเรียนการสอน/สร้างนักวิจัยใหม่)
     งานวิจัยนี้ได้สร้างนักวิจัยใหม่ เป็นนักวิจัยหลังปริญญาเอก จำนวน 1 คน และนิสิตระดับปริญญาโท อีก 1 คน

3. อื่นๆ (เช่น ผลงานตีพิมพ์ในวารสารวิชาการในประเทศ การเสนอผลงานในที่ประชุมวิชาการ หนังสือ การจดสิทธิบัตร)

3.1 เสนอผลงานเรื่อง “Highly dispersed graphene oxide/silver nanoparticle (GO/AgNP) composite in organic solvents” the 42nd Congress on Science and Technology of Thailand (STT 42), Bangkok, Thailand (Proceeding)

3.2 เสนอผลงานเรื่อง “Dispersion of graphene oxide and silver nanoparticles (GO/AgNPs) composite in organic solvents” Pure and Applied Chemistry International Conference 2016, Thailand.

Materials Chemistry and Physics 199 (2017) 348–355

Contents lists available at ScienceDirect

Materials Chemistry and Physics

journal homepage: www.elsevier.com/locate/matchemphys

Phase transferring of silver nanoparticles to organic solvents using modified graphene oxide as carrier

Oraporn Wong-u-ra [a], Sanong Ekgasit [b], Kanet Wongravee [b], *

[a] Program of Petrochemistry and Polymer Science, Faculty of Science, Chulalongkorn University, 254 Phayathai Road, Patumwan, Bangkok, 10330, Thailand
[b] Sensor Research Unit (SRU), Department of Chemistry, Faculty of Science, Chulalongkorn University, Bangkok, 10330, Thailand

HIGHLIGHTS

- Innovative phase transfer process of anisotropic silver nanoparticles is proposed.
- Phase transferring process using graphene oxide as carrier is presented.
- Dispersive behaviors of the GO/AgNP composite in various organic solvents.

GRAPHICAL ABSTRACT

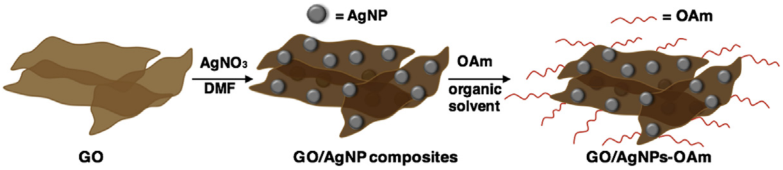

ARTICLE INFO

Article history:
Received 23 December 2016
Received in revised form
31 May 2017
Accepted 2 July 2017
Available online 3 July 2017

Keywords:
Graphene oxide
Phase transfer
Silver nanoparticles
Organic solvent

ABSTRACT

An innovative phase transferring process of anisotropic silver nanoparticles (AgNPs) from aqueous to a wide range of organic solvents (e.g. toluene, n-butanol, iso-butyl acetate, ethyl-acetate, acetonitrile and ethylene glycol) was described. In the developed process, AgNPs were transferred to the organic solvents by using graphene oxide (GO) as a carrier. The transferring process was utilized by only two straightforward steps. Firstly, the composite of graphene oxide-silver nanoparticles (GO/AgNPs) were synthesized using N,N′ dimethylformamide (DMF) as a reducing agent. The existence, purity and stability of AgNPs on the GO sheets were examined by UV–visible spectroscopy, FTIR spectroscopy, XRD, and TEM. Secondly, the composite GO/AgNP were modified with oleylamine (OAm) in order to improve hydrophobicity. To reach the maximum phase transfer efficiency, an appropriate amount of OAm was carefully optimized. The dispersion behaviors of the composite GO/AgNP modified with OAm (GO/AgNP-OAm) in the organic solvents were investigated. It was found that the GO/AgNP-OAm are uniformly dispersed in the organic solvents for at least 18 h after sonication. The developed phase transfer method has the features of simplicity and high efficiency, moreover, it suitable to be scaled up for the industrial application.

1. Introduction

Noble metal nanoparticles especially silver nanoparticles (AgNPs) is a promising class of functional materials which have tremendous applications in several practical fields including nanomedicide as antibacterial agents [1–3], catalysis as a promising heterogeneous catalyst [4–7], energy as a component in Li batteries [8], electronic [9], optical sensors [10], and environmental applications [11,12] due to their size- and shape-dependent optical, electrical, electronic and antibacterial properties. Therefore, a number of protocols have been proposed for synthesis silver nanoparticles in both polar (e.g. water) [13–15] and nonpolar organic solvents [16–18] for a widely usage in the several productions. However, due to the metal precursor ($AgNO_3$), most of the previous protocols were preferably performed in either water or

---

* Corresponding author.
E-mail address: kanet.w@chula.ac.th (K. Wongravee).

http://dx.doi.org/10.1016/j.matchemphys.2017.07.014

water-misible solvents. In the aqueous solvents, AgNPs are generally synthesized via the chemical reduction of silver ions with a reducing agent and control size and shape by an additional stabilizer [19–21]. Due to the synthesis protocol, the applications of those AgNPs was limited to the industrial and commercial products using water-based solvent. If the AgNPs were successfully synthesized and well-dispersed in organic solvents, it will open-up a new window of applications in polymers, coating materials and textiles which might require organic solvents as a media. However, to synthesize silver nanoparticles in organic solvents, a synthesis protocol is complicated and should be well-designed. For a practical usage of AgNPs, the transferring protocol of AgNPs is a potential alternative way to transfer AgNPs in aqueous solution to organic solvents [22–24]. Many authors reported the transferring process of silver nanoparticles into an organic phase by hydrophobization of the particle surface using various ligands such as alkylamines [25,26], ionic surfactants [27,28], amide coupling agents [29], etc. Such phase transfer procedures are very useful as aqueous phase synthesis of silver nanoparticles is relatively simple, inexpensive, and more reproducible, and furthermore, shape and size can be easily controlled using suitable stabilizers. However, there is a few severe limitations of the transferring process as (i) amount of transferring agents should be carefully optimized as they can be possibly from double layers around the particle, (ii) only small size of the particles might possibly be transferred and (iii) surface of the particle are dirty with the covered transferring agent molecules.

To overcome these limitations, the carrier system has been proposed to transfer the AgNPs to organic solvents. The system uses a carrier material as a transferring agent instead of using the surfactants. However, the type of carrier material should be well-considered as it should provide the functional groups to stabilize AgNPs, no loss on the properties of AgNPs, inert to any chemical reaction. From the literature overviews, the graphene oxide (GO) has emerged as a material that is often used to support and stabilize AgNPs for the preparation of novel nanocomposites for catalyst [30], antibacterial [31], SERS substrate [32], and sensors [33]. GO is not only providing strong interactions with the AgNPs but also enhances the properties of AgNPs [34]. According to the electronic charge of AgNP and oxygen rich functional groups on the GO, the generated AgNPs could be stabilized on the GO sheet and these functional group can be modified in order to increase hydrophobicity for transferring them into non-polar solvents. Therefore, GO might be considered as a good carrier material to transfer the AgNPs to organic media. Until now, no data exists to concern the phase transfer of AgNPs into organic solvents using GO as a carrier. Furthermore, this might be the first to report the phase transfer of the composite GO/AgNPs to be well dispersed in organic media. If the transferring protocol of the GO/AgNP composites is successfully developed, this will open up the new applications of the composites in electronics, polymers, coating etc.

In this work, we developed a simple, non-toxic, cost-effective, quick and environmentally friendly synthesis approach to fabricate graphene oxide based composite with silver nanoparticle (GO/AgNP) and the powerful protocol to modify them to form stable suspensions which can be well-dispersed in several organic solvents. Scheme 1 shows the overall protocol to transfer AgNPs into organic solvents using GO as a carrier. This proposed protocol provides several advantages such as (i) this protocol might not be affected from the uniformity of the AgNPs, (ii) the composite GO/AgNP can be stored in solid form and re-dispersed by sonication before using, (iii) the stability of AgNPs deposited on GO is very high (not oxidized to silver oxide), and (iv) it provides an appropriate color (gray metallic) instead of yellow which suitable in some commercial products.

The existence of AgNPs on GO nanosheets was examined by several techniques such as UV–Vis spectroscopy, XRD, TGA, and TEM. Furthermore, the stability of AgNPs decorated on GO was evaluated by the bath sonication. A hydrophobicity of the composites was increased using a primary amine with long hydrocarbon chain, oleylamine (OAm), to modify the surface of the GO/AgNP composites. The dispersion behavior and the stability of the modified GO/AgNPs in six organic solvents (e.g. toluene, *n*-butanol, iso-butyl acetate, ethyl acetate, acetonitrile, and ethylene glycol) were also investigated.

2. Experimental

2.1. Chemicals and materials

2 mg/mL of graphene oxide nanocolloids (GO) and oleylamine (OAm) were purchased from Sigma-Aldrich company. Ethanol (EtOH), ethyl acetate (EtOAc), and acetonitrile (ACN) were obtained from Merck (Thailand), while dimethylformamide (DMF), toluene (TOL) and ethylene glycol (EG) were purchased from Carlo Erba. Isobutyl acetate (*i*-BuOAc) and n-butanol (*n*-BuOH) were purchased from BDH chemicals and RCI Labscan Limited (Thailand), respectively. Silver nitrate ($AgNO_3$) was obtained from Aencore chemical company. All reagents and solvents were in analytical grade and were used without further purification. All glassware and magnetic bars were cleaned with detergent and followed by deionized (DI) water.

2.2. Preparation of GO/AgNP composites

The stock solution of 1500 ppm $AgNO_3$ was prepared by dissolving 0.075 g of $AgNO_3$ in 50 mL of DI water. 200 ppm of graphene oxide (GO) suspension was prepared by mixing 2.5 mL of GO suspension in 22.5 mL of DI water. The synthesis of GO/AgNP composites was performed by mixing 25 mL of the prepared 200 ppm GO with 25 mL of the stock solution of $AgNO_3$ and then immediately poured in 100 mL of DMF. The mixed solution was stirred and heated in sand bath with controlled temperature at 130–150 °C for 2 h. The reaction was incubated under ambient conditions until it cool down to the room temperature. The obtained GO/AgNP suspensions were then centrifuged at 5000 rpm for 20 min and then washed the colloids of GO/AgNPs by DI water for several times in order to remove the excess silver ions (Ag^+) and DMF. The obtained GO/AgNP composites were dried at 60 °C for 3 h. The existence of silver nanoparticles (AgNPs) on GO were characterized by UV–Vis spectroscopy, transmission electron microscopy, X-ray diffraction and thermal gravitation analysis.

2.3. Preparation of GO-OAm and GO/AgNPs-OAm

Oleylamine was used as a phase transferring agent to transfer GO into organic solvents. To transfer GO into organic solvents, the dried suspension of 200 ppm GO was modified by adding the oleylamine. The modified GO-OAm was then dispersed in organic solvents by sonication process. The various amounts of OAm was performed in order to determine the optimized condition for transferring GO in organic solvents. After obtaining the optimized amount of OAm, the appropriate amount of OAm was added to 2 mg of the GO/AgNP composites. The mixture was sonicated by bath sonication for 2 min to generate GO/AgNPs-OAm. To examine the dispersion behavior, the GO/AgNPs-OAm was dispersed in 5 mL of organic solvents; TOL, *n*-BuOH, *i*-BuOAc, EtOAc, ACN and EG with bath sonication (Elmasonic Model: P30H) for 1 h, the GO/AgNPs-OAm was well suspended in organic solvents affording the formation of uniformed dispersed gray colloids.

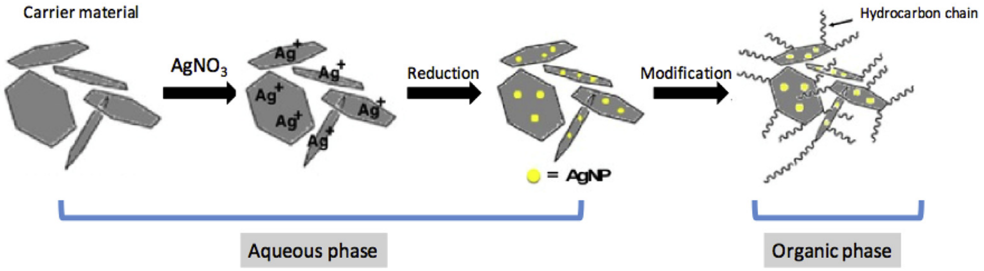

Scheme 1. The overall protocol to transfer AgNPs into organic solvents using GO as a carrier.

2.4. *Characterization*

The morphology and decomposition profiles of GO and GO/AgNP composites were examined by transmission electron microscopy (Hitachi Model: H-7650) and thermal gravitation analysis (Perkin Elmer Model: pyris 1TGA) with heating rate 20 °C/min and temperature 60–700 °C, respectively. The formation of AgNPs on GO surface was characterized by UV–visible spectroscopy (Thermo Fisher Scientific Model: G10S) and X-ray diffraction patterns were collected by an X-ray diffractometer (Rigaku D/MAX-2200) with a scanning rate of 0.02 deg/min, using Cu Ka irradiation (0.154 nm, 40 kV, 30 mA). The functional groups of GO, GO-OAm, GO/AgNP composite and GO/AgNPs-OAm was characterized by Fourier-transform infrared spectra (Nicolet 6700).

3. Results and discussion

3.1. *The preparation of GO/AgNP composites*

A preliminary investigation of the formation of the silver nanoparticles using DMF as a reducing agent were carried out using UV–Vis spectroscopy. The reduction reaction using DMF as a reducing agent is shown below [35].

$$HCON(CH_3)_2 + 2Ag^+ + H_2O \xrightarrow{130-150^\circ C} 2Ag^0 + (CO_2) + (CH_2)_2NH + 2H^+ \quad (1)$$

The UV–Vis spectra of the reaction were monitored for 3 h as shown in Fig. 1A. The appearance of characteristic localized surface Plasmon resonance band (LSPR) at ~430 nm indicates the formation of AgNPs generated since the reaction was prolonged for 1 h. However, there was no visibly observable of the LSPR band after 3 h without any sufficient stabilizer, this observation might relate to the indications of sedimentation, aggregation and agglomeration of the generated AgNPs as shown in ESI Fig. S1.

Next, GO nanosheets permeated with AgNPs were synthesized using DMF as a reducing agent. The prepared GO/AgNP composites were purified by centrifugation and washed with DI water for several times. The investigation of the formation of the AgNPs on GO sheet was carried out by several techniques. The UV–Vis spectra of the GO/AgNP composite compared with the bare GO suspensions is shown in Fig. 1B. The appearance of characteristic LSPR band at ~430 nm indicates the formation of AgNPs on GO nanosheet. On the other hand, only baseline shift without any characteristic peak was observed from the bare GO suspensions. Moreover, the stability of the deposited AgNPs on the GO nanosheet was also examined. The suspension of the GO/AgNP composites were strongly sonicated for 30 min and then were centrifuged at 2000 rpm for 10 min. Due to the centrifuge power, only the suspension of the GO/AgNP composites will be precipitated, while individual AgNPs still be dispersed in the supernatant. UV–Vis spectrum of the supernatant shows only baseline shift without any characteristic LSPR peaks of AgNPs. This suggests that AgNPs were strongly attached on GO sheets and were not detached from GO sheets by sonication process.

The purity of the AgNPs deposited on GO nanosheet is further examined by XRD analysis. The XRD patterns of the GO/AgNP composites are shown in Fig. 1C. The prominent peaks at 2θ values of 38.2°, 44.3°, 64.5° and 77.5° are assigned to the (111), (200), (220) and (311), respectively corresponding to crystalline planes of the face centered cubic (fcc) of metallic Ag (JCPDS no. 65–2871). The high intense diffraction peak observed at 38.2°, corresponding to the crystalline Ag, represent that the nanoparticles are composed of pure crystalline Ag.

The level of deposition of AgNP on GO nanosheets was assessed by the thermal gravimetric analysis (TGA) under N_2 environment. The weight ratio of AgNP on GO nanosheets was evaluated by TGA thermograms of weight loss as a function of temperature. The TGA analysis curves of the GO suspension and GO/AgNP composites are shown in Fig. 1D. TGA thermogram of GO suspension shows two weight loss profiles at 150–250 °C and 480–500 °C. The weight loss profile (~20%) at 150–250 °C relates to the evaporation of the absorbed water molecules on GO surface while weight loss (~40%) at 480–500 °C was from the decomposition of oxygen-containing functional groups [36]. However, TGA thermogram of GO/AgNP composites shows higher thermal stability. Only weight loss profile at 150–250 °C due to evaporated water was observed with only 5%. This smaller relative weight loss percentage suggests that there are enormous existed AgNPs on GO sheet. There is no weight loss profile at 500 °C. This phenomenon might relate to the strong interaction between oxygen functional groups and the generated AgNPs. Correspondingly, the anchoring amount of AgNPs on the GO sheet was approximately 80 wt% comparing to the bare GO sheet.

Fig. 1E shows the TEM images of a single layer GO nanosheet which was in form of flat layer with lateral size (~500 nm). On the other hand, the AgNPs represented by dark spots are homogeneously assembled on the sub-micro scale GO which were clearly noticed from TEM images of the GO/AgNP composites (Fig. 1F). The strong corrugation of GO surface after deposition of AgNPs with a serious aggregation was observed. This phenomenon evidently induces the aggregation of silver particles. In addition, the TEM images indicate that the average size of AgNPs is approximately 45 nm counted from 100 individual particles with a spherical geometry.

3.2. *Phase transferring of graphene oxide*

Generally, colloids of GO are well dispersed in water media. To transferring GO into organic media, improving the hydrophobic property of GO surface might be required. In this work, oleylamine (OAm) which was a primary amine with the long chain hydrocarbon ($C_{18}H_{35}NH_2$) was used as a phase transferring agent to transfer

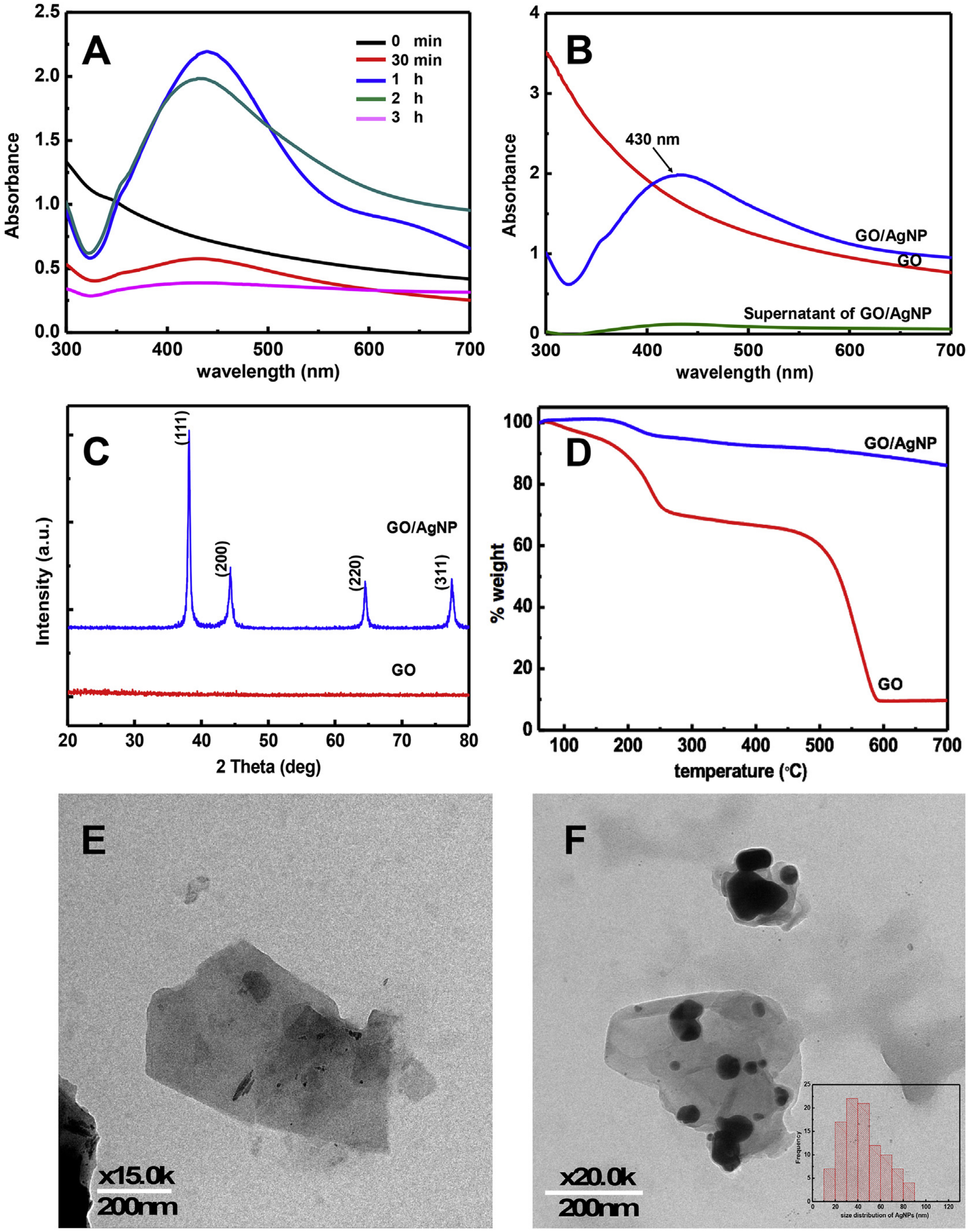

Fig. 1. (A) UV–Vis spectra of the formation of AgNPs reduced by DMF with the reaction time 30 min, 1 h, 2 h and 3 h (B) UV–Vis spectra of the GO suspensions, the GO/AgNP composites and the supernatant of the GO/AgNP composite solution. (C) XRD patterns of the synthesized GO/AgNP composites compared with the GO suspensions, (D) TGA thermograms of GO and the GO/AgNP composites and TEM images of (E) GO suspensions and (F) the GO/AgNP composites including inset figure of size distribution of AgNPs.

GO into organic media. Electrostatic interaction between oxygen rich functional groups on GO nanosheets and amine group of OAm were easily occurred [37]. These strong interactions between GO and OAm (GO-OAm) was examined by the FT-IR spectral analysis as shown in Fig. 2A. The set of characteristic peaks of GO represents at ~3250 cm^{-1} (O–H stretching vibrations), at 1720 cm^{-1} (C=O stretching vibrations), at ~1610 cm^{-1} (aromatic C=C stretching vibrations), and at ~1070 cm^{-1} (C–O–C stretching vibrations). The FT-IR spectra of OAm and GO-OAm show the strong intensity absorption band at ~2920 cm^{-1} and 2850 cm^{-1} corresponding to the C–H aliphatic stretching vibrations and the amine group (N–H) at ~1465 cm^{-1}. These observations confirm the interaction between amine group of OAm with the functional groups on GO sheet.

Prior to study the dispersion behavior of GO-OAm in organic solvents, the dispersive efficiency of the GO suspension in water was preliminary investigated by using UV–Vis spectroscopy. The UV–Vis spectra of various concentrations (10 ppm–50 ppm) of the GO suspensions in water were collected as shown in Fig. 2B. It can be seen there is no specific band on UV–visible spectra of GO colloidal solution but the background intensity was linearly related to the concentration of GO. The higher concentration of GO, the higher background intensity appears. An inset on Fig. 2B shows a

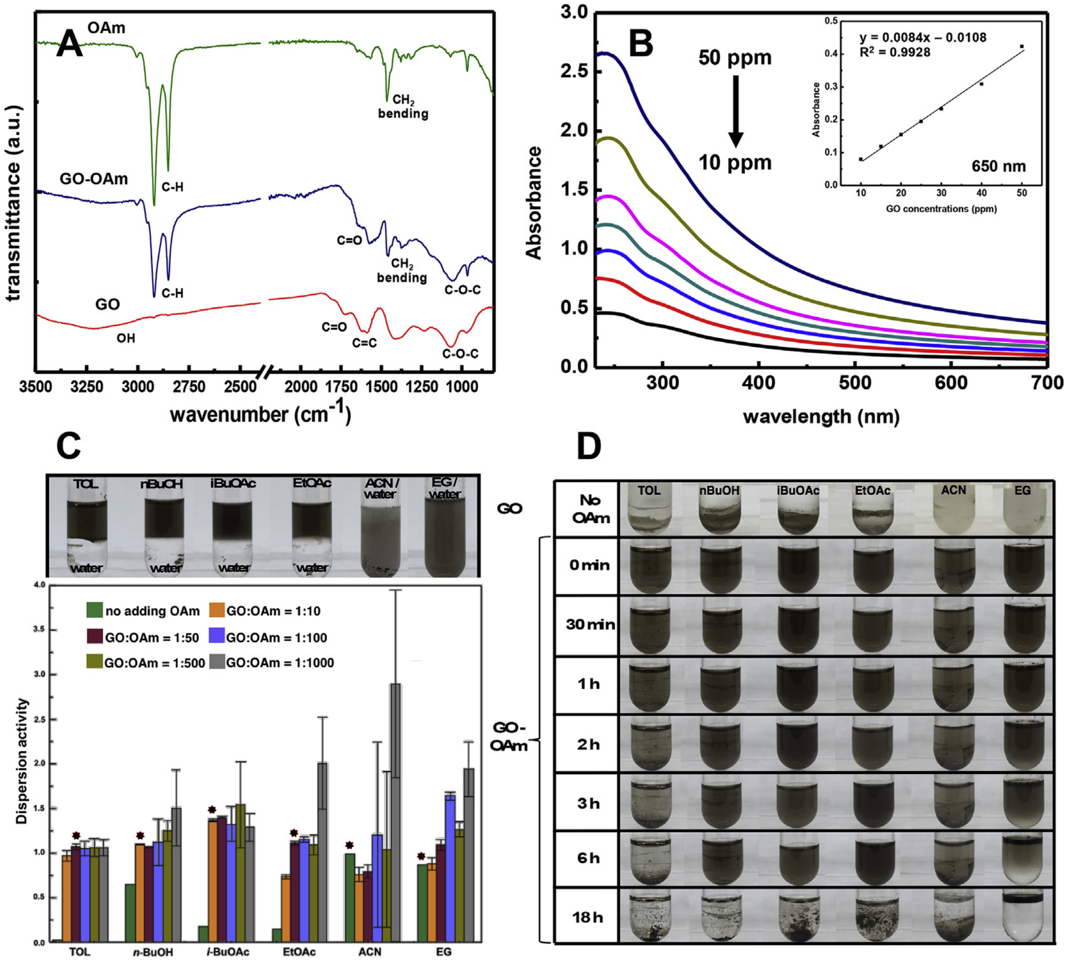

Fig. 2. (A) FT-IR spectra of the GO, GO-OAm and OAm (B) UV–Vis spectra of the GO suspension with various concentrations (10 ppm–50 ppm) with the inset image which displays the calibration curve constructed by collecting absorbance at 650 nm vs. GO concentrations. (C) the dispersion activity of GO-OAm using various amounts of OAm in organic solvents. An appropriate amount of OAm used to transfer GO into organic solvents was marked with star symbol (*). (D) Digital images represent the dispersed GO and GO-OAm in several organic solvents immediately after sonication and after leaving them for 0–18 h.

calibration line with $R^2 > 0.99$ constructed by measuring the absorbance at 650 nm of GO colloidal solutions at different concentrations. This calibration curve was used as standard index to calculate dispersive efficiency of the GO-OAm in organic solvents.

To study the dispersion behavior of the GO-OAm in organic media, the complex of GO-OAm was distributed in different organic solvents (TOL, *n*-BuOH, *i*-BuOAc, EtOAc, ACN and EG). The variation of the dispersion behavior might be related to the compatibility of solvents (dipole moments, polarity, and surface tensions as shown in ESI Table S1) and the hydrophobicity of the GO-OAm [38]. Therefore, the optimization of amount of OAm might be required in order to assess the maximum dispersion of GO in organic solvents. To reach an appropriate amount of OAm used to transfer GO into organic solvent, a dispersion activity calculated from the ratio of A'_{650}/A_{650}, where A'_{650} and A_{650} are the absorbance at 650 nm of GO-OAm dispersed in organic solvents and GO dispersed in water, respectively.

To optimize amount of OAm used to transfer GO into organic solvents, the weight ratios of GO:OAm were varied at 1:10, 1:50, 1:100, 1:500 and 1:1000, respectively. Fig. 2C shows the dispersion activity of GO-OAm using various amount of OAm in several organic solvents. The small index of dispersion activity represents a small proportion of GO that can be transferred to organic solvents. This reflects an insufficient of OAm for transferring GO into organic solvents. However, the high value of the dispersion activity with a large variation is observed when the larger amount of OAm was used. This observation might be originated from an excess amount of OAm which induces the aggregation/agglomeration of GO to form a multilayer GO sheets due to the hydrophobicity of long chain hydrocarbon on OAm molecules. Therefore, a suitable amount of OAm should be determined by giving dispersion activity of GO-OAm close to 1 with less variation. This means the dispersion behavior of GO-OAm in organic solvent is similar to the starting GO suspensions in water. In each organic solvent, an appropriate amount of OAm was determined (marking with star symbol). Inset of Fig. 2C displays the digital photographs of the dispersed GO-OAm taken in several organic solvents immediately after the sonication. To determine the degree of sedimentation, the digital images were again taken in the range of 0–18 h. After sonication, the GO-OAm using an appropriate amount of OAm showed very good dispersion in all solvents: TOL, *n*-BuOH, *i*-BuOAc, EtOAc, ACN and EG. The water was added in order to separate organic phase and water phase. In case of CAN and EG, these solvents are homogenously soluble with water. The long-term stability was examined by leaving the suspensions undisturbed for 18 h. The results clearly displayed that the starting GO was completely not dispersed in any organic solvents, while GO-OAm retained its excellent dispersibility in especially *n*-BuOH, *i*-BuOAc, EtOAc for at least 6 h. In case of TOL, a precipitation of GO-OAm was observed after 2 h. The long-term stability of the GO-OAm might be majorly related to the polarity of the solvents where TOL provides the lowest polarity in the case. It is worth mentioning that the stability of the dispersion GO-OAm for 6 h might adequate for the industrial and research applications. Moreover, the precipitated GO-OAm can be re-dispersed by bath sonication (ESI Fig. S1) which is practically used in the industrial/manufacturing.

3.3. Phase transfer of graphene oxide-silver nanoparticle (GO/AgNP) composites

The transferring process for GO by using OAm as transferring agent was performed with the GO/AgNP composites. In our case, the AgNPs cannot be directly transferred into organic solvents using OAm as shown in ESI Fig. S2. The optimized amount of OAm in each organic solvent was used to increase hydrophobicity of GO surface of the GO/AgNP composites and produce the GO/AgNPs-OAm. The presence of AgNPs on the GO/AgNPs-OAm in the organic solvents was investigated by UV–Visible spectroscopy as shown in Fig. 3A. The characteristic Plasmon bands of AgNPs at ~430 nm is clearly detected in all solvents. It should be noted that the dispersive efficiency of the GO/AgNPs-OAm might be different due to the solvent properties. This causes on the variation of baseline shifts in UV–Vis spectra. The decomposition profiles of GO-OAm and GO/AgNPs-OAm were assessed by the thermal gravimetric analysis (TGA) under N_2 environment. Fig. 3B shows the TGA thermograms of weight loss as a function of temperature. The TGA curves of GO-OAm and GO/AgNPs-OAm were also observed the weight loss profiles at 350–450 °C corresponding to the desorption of the range of C_1–C_3 hydrocarbon fragments. These fragments were referred to amine fragments; $C_1NH_2^+$ and $C_2NH_2^+$ of the OAm molecules. The anchoring amount of AgNPs on the GO nanosheets was approximately 35 wt% comparing to the GO-OAm. In addition, the digital images of the GO/AgNPs-OAm suspension in the organic solvents are shown in an inset of Fig. 3C. From the digital images, they are observed that the GO/AgNPs-OAm is well-dispersed in all organic solvents. To evaluate the stability of the dispersion of the GO/AgNPs-OAm, the suspension solution was monitored undisturbed for 18 h by capturing the images as shown in ESI Fig. S2. From Fig. S2, the long-term stability of GO/AgNPs-OAm was observed in especially iBuOAc, EtOAc, ACN and EG for at least 18 h.

To assess the morphology, the GO/AgNPs-OAm in EtOAc was investigated by TEM as shown in Fig. 3C. It can be seen that the AgNPs still remain on GO nanosheets after transferring to the organic solvent. However, these particles seem to be disaggregated with the unfolding of GO nanosheets. The unfolding mechanism of GO sheets might be induced by the increasing of the hydrophobicity of GO nanosheets from long hydrocarbon chain of OAm. From the observation on TEM images, AgNPs might be detached from an unfolded GO nanosheets. To test the stability of the AgNPs

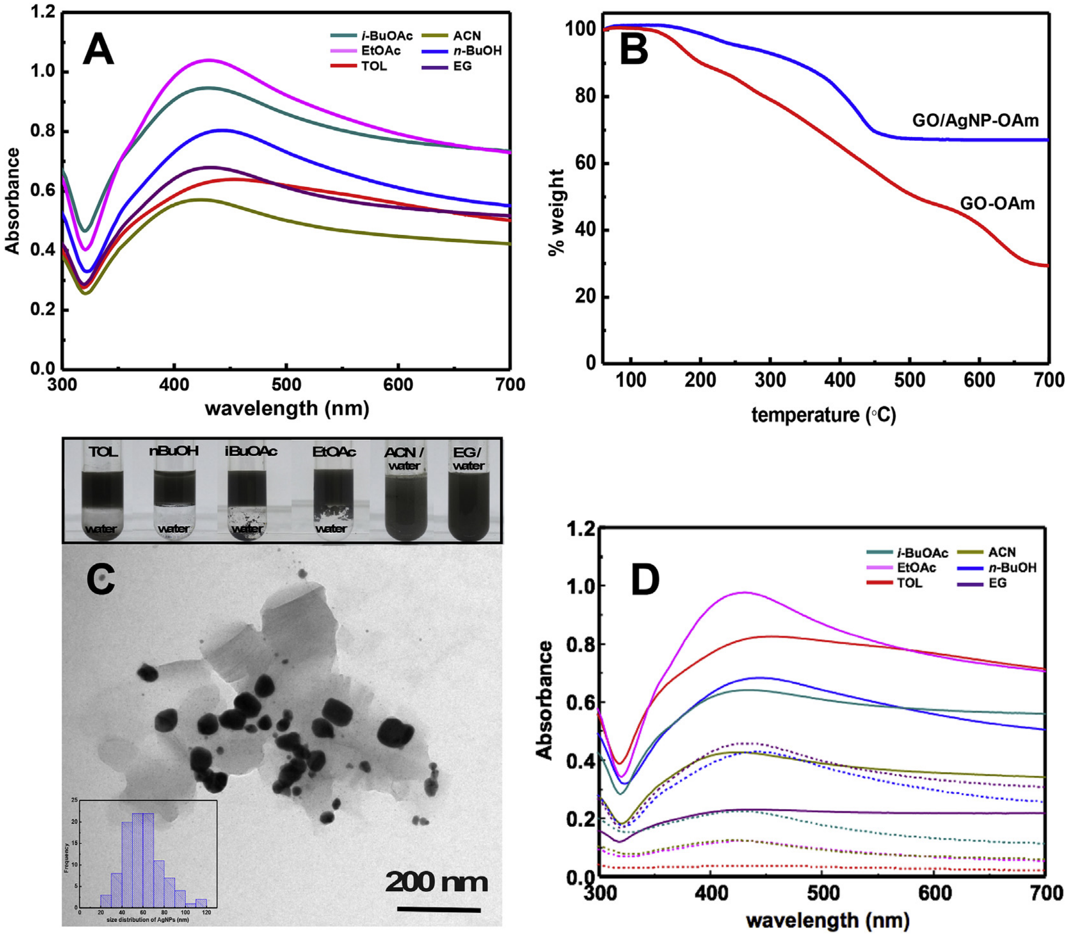

Fig. 3. (A) UV–Vis spectra of the dispersion of the GO/AgNP-OAm in the organic solvents. (B) TGA thermograms of GO-OAm and the GO/AgNP-OAm. (C) TEM images of GO/AgNP-OAm in ethyl acetate (EtOAc) with the photographs represents the GO/AgNP-OAm suspension in several organic solvents immediately after sonication and (D) UV–Vis spectra of the dispersion of the GO/AgNP-OAm pellet in organic solvents (solid lines) and the normalized supernatant of GO/AgNP-OAm composites (dot lines).

deposited on the transferred GO/AgNPs-OAm, the suspension of GO/AgNPs-OAm in organic solvents was sonicated and then followed by centrifuging at 2000 rpm for 10 min. The supernatant was collected for analyzing while the sediment pellets were re-dispersed in the organic solvents. These two fractions were analyzed by UV–Vis spectroscopy. Fig. 3D shows UV–Vis spectra of the supernatant (dot lines) and re-dispersed GO/AgNPs-OAm (solid line). It can be seen that the absorbance of supernatant was mostly lower than the re-dispersed GO/AgNPs-OAm in TOL, n-BuOH, i-BuOAc, EtOAc and ACN. These observations suggest that AgNPs were still remained on GO sheets. However, the Plasmon band of AgNPs (~430 nm) was observed in the supernatant from n-BuOH, EtOAc and i-BuOAc. This suggests that the fractional AgNPs on the GO/AgNPs-OAm were partially detached by sonication process.

After phase transferring, XRD measurements were performed to monitor the stability of AgNP on GO sheets after storing for 6 months (Sep 2016-May 2017). The diffraction patterns of the GO/AgNPs-OAm in toluene after storing for 6 months and the fresh GO/AgNPs-OAm are shown in ESI Fig. S5. It can be seen that XRD patterns are not changed and still in a good agreement with a standard XRD patterns of the pure Ag (JCPDS no. 65–2871). This suggests that the AgNPs on the GO sheet are very stable even when they had been stored for 6 months.

4. Conclusions

We successfully developed the phase transferring process to transfer the AgNPs into the organic solvents by using GO as a carrier material. The process carries out only two steps: the formation of AgNPs on GO surface through chemical reaction by using DMF as a reducing agent, and then the GO/AgNP composites were modified its surface by oleylamine (OAm) to increase the hydrophobicity of the composites. The AgNPs were uniformly generated and assembled on a surface of GO sheets with highly stability according to the strong interaction between tremendous oxygen-functional groups on GO and the AgNP particle. These AgNP particles on GO sheet cannot be detached by an ultrasonic. The modified GO/AgNP with oleylamine to form GO/AgNPs-OAm is highly dispersed in the organic solvents for at least 6 h. However, the sediments of GO/AgNPs-OAm can be re-dispersed using ultrasonic without any detraction of AgNPs. This developed phase transfer method opens an alternative way to transfer AgNPs into organic solvents with simplicity and high efficiency, moreover, it suitable to be scaled up for the industrial applications.

Acknowledgements

The study is financially supported by International Research Integration: Chula Research scholar, Ratchadaphiseksomphot Endowment Fund and Thailand Research Fund (TRG 5880238). S. Ekgasit would like to thank National Research University Project, Office of Higher Education Commission (NRU59-044-AM). Finally, authors would like to delicate the manuscript for “In remembrance of His Majesty King Bhumibol Adulyadej (1927–2016), for his lifetime dedication to Thailand”.

Appendix A. Supplementary data

Supplementary data related to this article can be found at http://dx.doi.org/10.1016/j.matchemphys.2017.07.014.

References

[1] K. Zheng, M.I. Setyawati, T.P. Lim, D.T. Leong, J. Xie, Antimicrobial cluster bombs/silver nanoclusters packed with daptomycin, ACS Nano 10 (2016) 7934–7942.

[2] M. Guzman, J. Dille, S. Godet, Synthesis and antibacterial activity of silver nanoparticles against gram-positive and gram-negative bacteria, Nanomedicine Nanotechnol. Biol. Med. 8 (2012) 37–45.

[3] X.R. Song, N. Goswami, H.H. Yang, J. Xie, Functionalization of metal nanoclusters for biomedical applications, Analyst 141 (2016) 3126–3140.

[4] C.C.M. Neumann, E. Laborda, K. Tschulik, K.R. Ward, R.G. Compton, Performance of silver nanoparticles in the catalysis of the oxygen reduction reaction in neutral media: efficiency limitation due to hydrogen peroxide escape, Nano Res. 6 (2013) 511–524.

[5] H. Chaudhuri, S. Dash, A. Sarkar, Single-Step room-temperature in situ syntheses of sulfonic acid functionalized SBA-16 with ordered large pores/potential applications in dye adsorption and heterogeneous catalysis, Ind. Eng. Chem. Res. 56 (2017) 2943–2957.

[6] N. Goswani, Q. Yao, T. Chen, J. Xie, Mechanistic exploration and controlled synthesis of precise thiolate-gold nanoclusters, Coord. Chem. Rev. 329 (2016) 1–15.

[7] Y. Liu, Q. Yao, X. Wu, T. Chen, Y. Ma, C.N. Ong, J. Xie, Gold nanocluster sensitized TiO_2 nanotube arrays for visible-light driven photoelectrocatalytic removal of antibiotic tetracycline, Nanoscale 8 (2016) 10145–10151.

[8] M. Lu, J. Qu, Q. Yao, C. Xu, Y. Zhan, J. Xie, J.Y. Lee, Exploring metal nanoclusters for lithium–oxygen batteries, ACS Appl. Mater. Interfaces 7 (2015) 5488–5496.

[9] A.H. Alshehri, M. Jakubowska, A. Młożniak, M. Horaczek, D. Rudka, C. Free, J.D. Carey, Enhanced electrical conductivity of silver nanoparticles for high frequency electronic applications, ACS Appl. Mater. Interfaces 4 (2012) 7007–7010.

[10] S. Pandey, G.K. Goswami, K.K. Nanda, Green synthesis of biopolymer–silver nanoparticle nanocomposite: an optical sensor for ammonia detection, Int. J. Biol. Macromol. 51 (2012) 583–589.

[11] Q. Liu, Zh Zhou, G. Qiu, J. Li, J. Xie, J.Y. Lee, Surface reaction route to increase the loading of antimicrobial Ag nanoparticles in forward osmosis membranes, ACS Sustain. Chem. Eng. 3 (2015) 2959–2966.

[12] J. Li, T. Zhao, T. Chen, Y. Liu, C.N. Ong, J. Xie, Engineering noble metal nanomaterials for environmental applications, Nanoscale 7 (2015) 7502–7519.

[13] H. Wang, X. Qiao, J. Chen, S. Ding, Preparation of silver nanoparticles by chemical reduction method, Colloids Surfaces A Physicochem. Eng. Aspects 256 (2005) 111–115.

[14] A. Panáček, L. Kvítek, R. Prucek, M. Kolář, R. Večeřová, N. Pizúrová, V.K. Sharma, T. Nevěčná, R. Zbořil, Silver colloid nanoparticles: synthesis, characterization and their antibacterial activity, J. Phys. Chem. B 110 (2006) 16248.

[15] S. Iravani, H. Korbekandi, S.V. Mirmohammadi, B. Zolfaghari, Synthesis of silver nanoparticles: chemical, physical and biological methods, Res. Pharm. Sci. 9 (2014) 385–406.

[16] W. Zhang, X. Qiao, J. Chen, H. Wang, Preparation of silver nanoparticles in water-in-oil AOT reverse micelles, J. Colloid Interface Sci. 302 (2006) 370–373.

[17] C. Jiang, L. Li, P.W.T. Pong, Controlled convective self-assembly of silver nanoparticles in volatile organic solvent and its application in electronics, RSC Adv. 5 (2015) 98747–98756.

[18] L. Lu, X. An, Silver nanoparticles synthesis using H_2 as reducing agent in toluene–supercritical CO_2 microemulsion, J. Supercrit. Fluids 99 (2015) 29–37.

[19] R. Dondi, W. Su, G.A. Griffith, G. Clark, G.A. Burley, Highly size- and shape-controlled synthesis of silver nanoparticles via a templated tollens reaction, Small 8 (2012) 770–776.

[20] S. Agnihotri, S. Mukherji, S. Mukherji, Size-controlled silver nanoparticles synthesized over the range 5-100 nm using the same protocol and their antibacterial efficacy, RSC Adv. 4 (2014) 3974–3983.

[21] N.G. Bastús, F. Merkoçi, J. Piella, V. Puntes, Synthesis of highly monodisperse citrate-stabilized silver nanoparticles of up to 200 nm: kinetic control and catalytic properties, Chem. Mater 26 (2014) 2836.

[22] J. Yang, J.Y. Lee, J.Y. Ying, Phase transfer and its applications in nanotechnology, Chem. Soc. Rev. 40 (2011) 1672–1696.

[23] J. Yang, J.Y. Lee, H.P. Too, A general phase transfer protocol for synthesizing alkylamine-stabilized nanoparticles of noble metals, Anal. Chim. Acta 588 (2007) 34–41.

[24] Y. Wei, J. Yang, J.Y. Ying, Reversible phase transfer of quantum dots and metal nanoparticles, Chem. Commun. 46 (2010) 3179–3181.

[25] X. Wang, S. Xu, J. Zhou, W. Xu, A rapid phase transfer method for nanoparticles using alkylamine stabilizers, J. Colloid Interface Sci. 348 (2010) 24–28.

[26] M.G. Soliman, B. Pelaz, W.J. Parak, P. del Pino, Phase transfer and polymer coating methods toward improving the stability of metallic nanoparticles for biological applications, Chem. Mater 27 (2015) 990–997.

[27] S.-Y. Zhao, S.-H. Chen, D.-G. Li, X.-G. Yang, H.-Y. Ma, A convenient phase transfer route for Ag nanoparticles, Phys. E 23 (2004) 92–96.

[28] C.P. Joshi, T.P. Bigioni, Model for the phase transfer of nanoparticles using ionic surfactants, Langmuir 30 (2014) 13837–13843.

[29] L. Liu, T.L. Kelly, Phase transfer of triangular silver nanoprisms from aqueous to organic solvent by an amide coupling reaction, Langmuir 29 (2013) 7052–7060.

[30] J.D. Kim, T. Palani, M.R. Kumar, S. Lee, H.C. Choi, Preparation of reusable Ag-decorated graphene oxide catalysts for decarboxylative cycloaddition, J. Mater. Chem. 22 (2012) 20665–20670.

[31] A.F. de Faria, F. Perreault, E. Shaulsky, L.H. Arias Chavez, M. Elimelech, Antimicrobial electrospun biopolymer nanofiber mats functionalized with graphene oxide–silver nanocomposites, ACS Appl. Mater. Interfaces 7 (2015) 12751–12759.

[32] S. Vijay Kumar, N.M. Huang, H.N. Lim, A.R. Marlinda, I. Harrison, C.H. Chia, One-step size-controlled synthesis of functional graphene oxide/silver nanocomposites at room temperature, Chem. Eng. J. 219 (2013) 217–224.

[33] S. Liu, J. Tian, L. Wang, X. Sun, Microwave-assisted rapid synthesis of Ag nanoparticles/graphene nanosheet composites and their application for hydrogen peroxide detection, J. Nanoparticle. Res. 13 (2011) 4539–4548.

[34] M. Sawangphruk, P. Srimuk, P. Chiochan, T. Sangsri, P. Siwayaprahm, Synthesis and antifungal activity of reduced graphene oxide nanosheets, Carbon 50 (2012) 5156–5161.

[35] I. Pastoriza-Santos, L.M. Liz-Marzán, N,N-Dimethylformamide as a reaction medium for metal nanoparticle synthesis, Adv. Funct. Mater 19 (2009) 679–688.

[36] M.S. Shafeeyan, W.M.A.W. Daud, A. Houshmand, A. Shamiri, A review on surface modification of activated carbon for carbon dioxide adsorption, J. Anal. Appl. Pyrolysis 89 (2010) 143–151.

[37] M.J. Manard, P.R. Kemper, M.T. Bowers, Binding interactions of mono- and diatomic silver cations with small alkenes: experiment and theory, Inter. J. Mass Spectrom. 241 (2005) 109–117.

[38] W. Yu, H. Xie, X. Wang, X. Wang, Highly efficient method for preparing homogeneous and stable colloids containing graphene oxide, Nanoscale Res. Lett. 6 (2011) 47.

Electronic Supporting Information

Phase transferring of Silver Nanoparticles to Organic Solvents using Modified Graphene Oxide as Carrier

Oraporn Wong-u-ra[1], Sanong Ekgasit[2], Kanet Wongravee[*,2]

[1]Program of Petrochemistry and Polymer Science, Faculty of Science, Chulalongkorn University, 254 Phayathai Road, Patumwan, Bangkok 10330, Thailand.

[2] Sensor Research Unit (SRU), Department of Chemistry, Faculty of Science, Chulalongkorn University, Bangkok, 10330, Thailand.

*corresponding author : kanet.w@chula.ac.th

Table

Table S1: Properties of solvents including polarity, dipole moments, surface tensions

Figures

Fig S1 The TEM images of the composite GO/AgNP after 3 hrs of the reduction reaction.

Fig S2 UV-visible spectrum of AgNP (black) and GO/AgNP (blue) in water solution and AgNP-OAm (red) and GO/AgNP-OAm (green) after modified with oleylamine in ethyl acetate.

Fig S3 Redispersibility of GO/AgNP-OAm in organic solvents

Fig S4 Captured digital images represent the digital photographs of the dispersed GO/AgNP and GO/AgNP-OAm in several organic solvents immediately after sonication and after leaving them for 0-18 hours.

Fig S5 : The diffraction patterns of the GO/AgNP-OAm in toluene after storing for 6 months (Sep 2016-May 2017) and the fresh GO/AgNP-OAm

Table S1: Properties of solvents including polarity, dipole moments, surface tensions

Solvents	**Polarity index (P′)**	**Dipole moment**	**Surface tension (mN/m)**	**Solubility in water (%w/w)**	**Dielectric constant**
DI water	10.2	1.87	72.8	-	80.1
toluene (TOL)	2.4	0.31	28.5	0.051	2.38
n-butanol (nBuOH)	3.9	1.75	24.6	0.43	
i-butyl acetate (iBuOAc)	4.0	1.84	25.1	7.87	5.01
ethyl acetate (EtOAc)	4.4	1.88	23.8	8.7	6.02
acetonitrile (ACN)	5.8	3.44	19.10	100	37.5
ethylene glycol (EG)		2.31	47.7	100	

https://people.chem.umass.edu/xray/solvent.html
http://macro.lsu.edu/howto/solvents/Polarity%20index.htm

Fig S1 The TEM images of the composite GO/AgNP after 3 hrs of the reduction reaction.

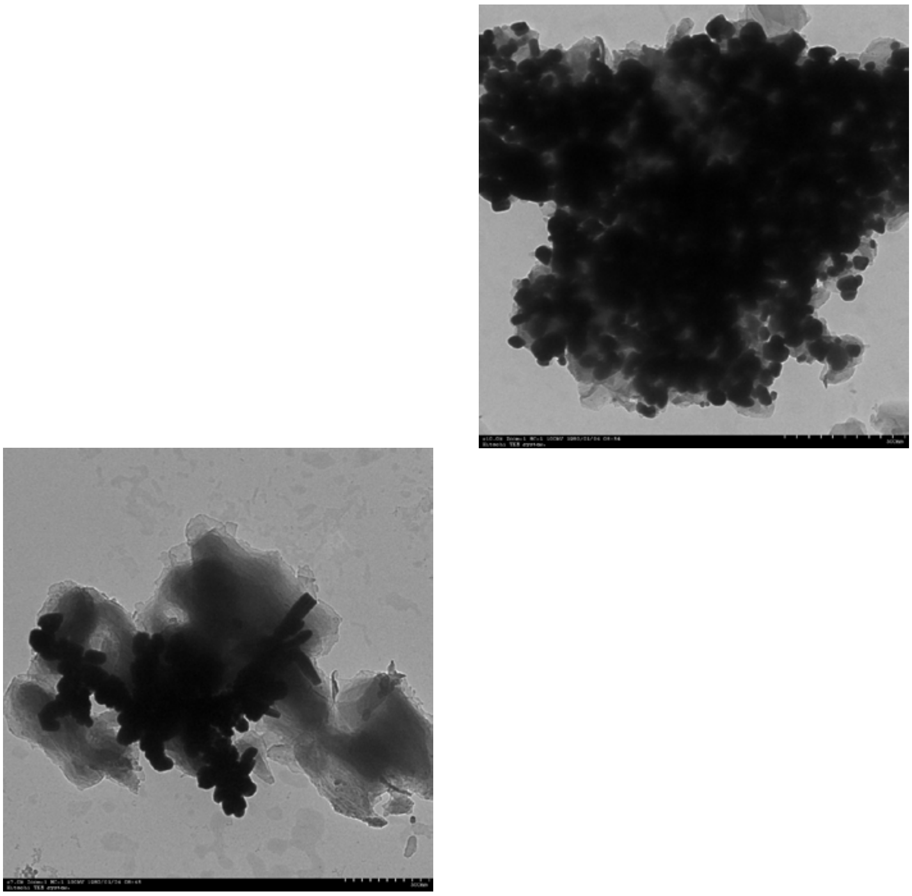

These TEM images clearly show that there are some aggregation or agglomeration of AgNP particles on GO sheets. After 3 hrs, an enormous AgNP particles was generated and the stabilization power of GO sheets might not be adequate to stabilize those AgNPs. These phenomena will induce the aggregation and agglomeration of the AgNPs

Fig S2 UV-visible spectrum of AgNP (black) and GO/AgNP (blue) in water solution and AgNP-OAm (red) and GO/AgNP-OAm (green) after modified with oleylamine in ethyl acetate.

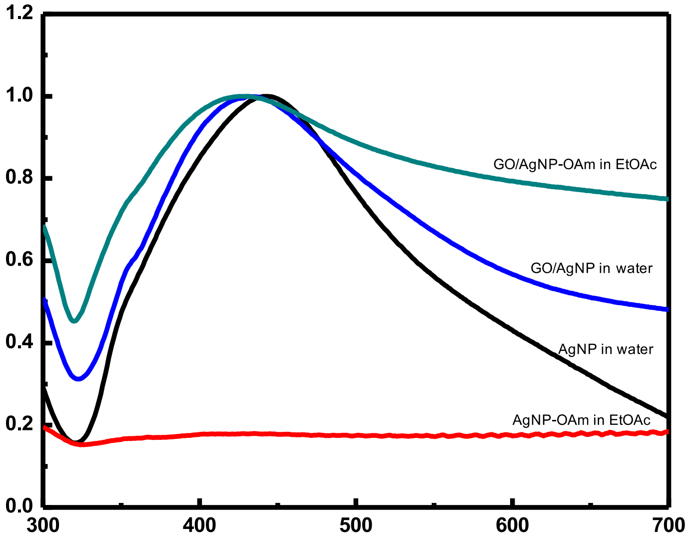

From UV-visible spectra, it can be seen that AgNPs cannot be directly transferred to organic solvent directly by using oleylamine. The characteristic LSPR of AgNPs cannot be observed after transferring the AgNP-OAm to ethyl acetate (red spectrum). In case of using OAm to transfer the composite of GO/AgNP, the LSPR peak of AgNPs is clearly observed after transferring to ethyl acetate (green spectrum).

We already discussed that there are some drawbacks to directly transfer AgNPs using OAm as transferring agent because amount of OAm should be well optimized. The OAm micelle on AgNP surface cannot be formed if an insufficient amount of OAm was used. On the other hand, an excess amount of OAm will possibly induce the formation of double layers of OAm on AgNP surface which inhibits the transferring process. Therefore, only particle with appropriate (small) size can be transferred. Therefore, the using GO as carrier assisted by OAm to transfer AgNPs into organic solvents was proposed to overcome these limitations.

Fig S3 : Redispersibility of GO/AgNP-OAm in organic solvents

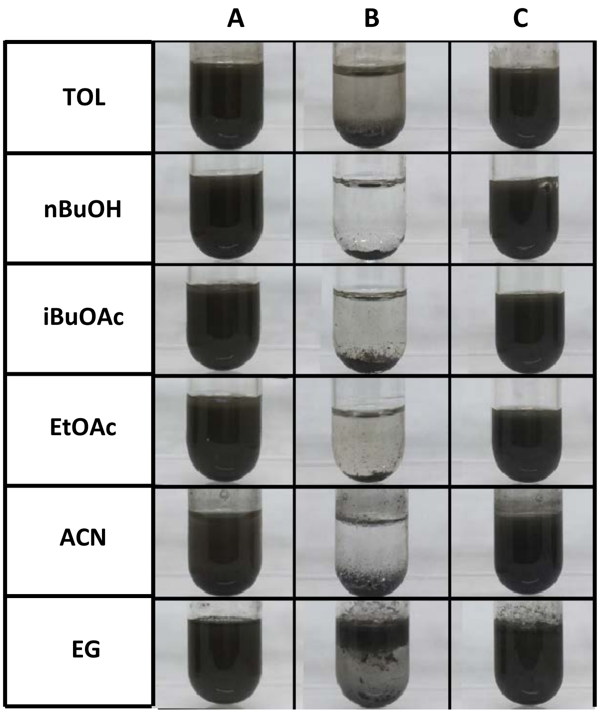

column A: GO/AgNP-OAm was dispersed in organic solvents after sonication.

column B: GO/AgNP-OAm was dispersed in organic solvents for 18 hours.

column C: GO/AgNP-OAm was re-sonicated in organic solvents again after leaving for 18 hours.

Fig S4 : Captured digital images represent the digital photographs of the dispersed GO/AgNP and GO/AgNP-OAm in several organic solvents immediately after sonication and after leaving them for 0-18 hours.

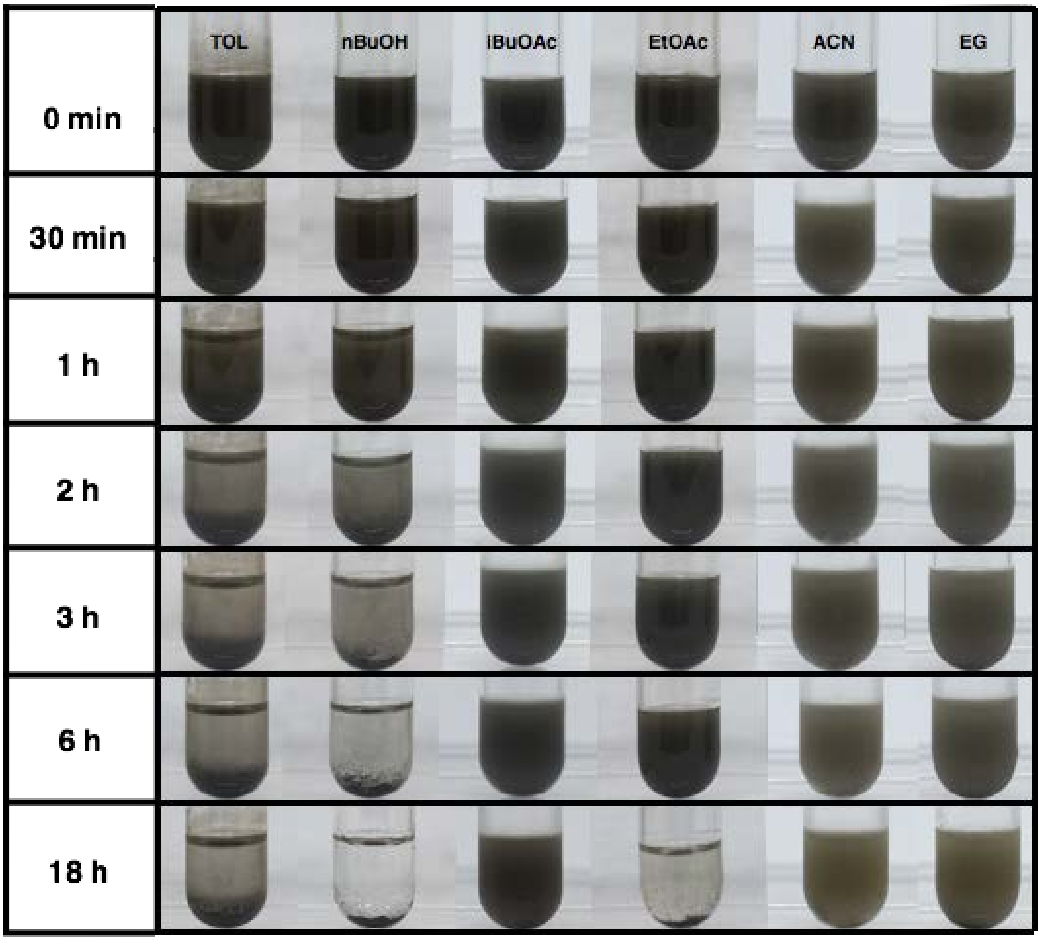

Fig S5 : The diffraction patterns of the GO/AgNP-OAm in toluene after storing for 6 months (Sep 2016-May 2017) and the fresh GO/AgNP-OAm

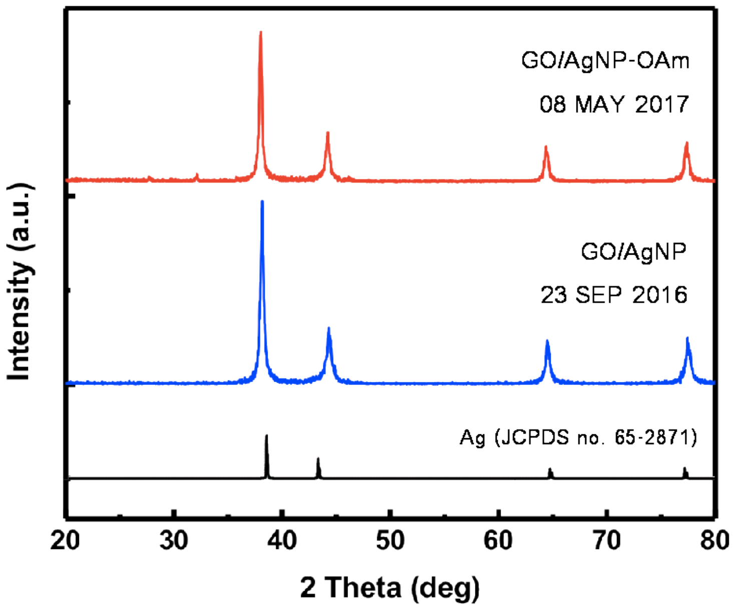

Materials & Design 125 (2017) 158–166

Contents lists available at ScienceDirect

Materials & Design

journal homepage: www.elsevier.com/locate/matdes

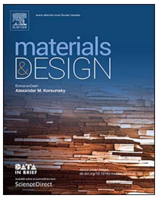

Shape evolution of 3D flower-like gold microstructures from gold nanosheets via oriented attachment

Supeera Nootchanat[a], Chutiparn Lertvachirapaiboon[b], Vittaya Amornkitbamrung[c], Pikaned Uppachai[d], Sanong Ekgasit[a], Kanet Wongravee[a,*]

[a] *Sensor Research Unit, Department of Chemistry, Faculty of Science, Chulalongkorn University, 254 Phyathai Road, Patumwan, Bangkok 10330, Thailand*
[b] *Graduate School of Science and Technology, Niigata University, 8050, Ikarashi 2-nocho, Nishi-ku, Niigata 950-2181, Japan*
[c] *Integrated Nanotechnology Research Center, Khon Kaen University, Khon Kaen 40000, Thailand*
[d] *Department of Applied Physics, Faculty of Engineering, Rajamangala University of Technology Isan, Khon Kaen Campus, Khon Kaen 40000, Thailand*

ARTICLE INFO

Keywords:
Flower-like gold microstructures
Gold nanosheets
Hydrogen peroxide
Oriented attachment
Nanostructures
SERS

ABSTRACT

Herein, we present a shape evolution of 3D flower-like gold microstructures (3D-FLGMSs) from gold nanosheets induced by H_2O_2 with the presence of starch. A systematic investigation of the influence of the parameters on the size, morphology and structural evolution of 3D-FLGMSs was presented. Under the starch-stabilized environment, H_2O_2 plays a key role on the formation of 3D-FLGMSs as it promotes a rapid generation of small nanosheets with starch-bound {111} facet at the very early stage. At a high concentration of H_2O_2, the nanosheets undergo oriented attachment and transform into a large primary gold nanosheets with imperfect facet-binding. The oriented attachment (OA) and subsequent epitaxial growth of nanopetals from the imperfects turns the primary nanosheets into 3D-FLGMSs with lateral size as large as 30 μm within 120 min. Without starch, quasi-microspheres of gold with diameters of 5–7 μm are the sole product. In addition, the 3D-FLGMSs can be employed as SERS substrates which allow the detection limit of Rhodamine 6G (R6G) at the concentration as low as 0.1 μM. The developed green synthetic method utilizes non-toxic reducing and stabilizing agents while limiting the discharge of harmful chemical wastes.

GRAPHICAL ABSTRACT

The shape evolution of flower-like gold microstructures from gold nanosheets via oriented attachment induced by H_2O_2 with the presence of starch.

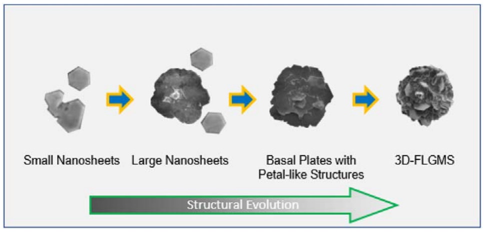

Highlights

- Flower-like gold microstructures were fabricated with 100% conversion of gold ions.
- The growth mechanism of flower-like gold microstructures has been revealed.
- The synthesis protocol is cost-effective, efficient and environmentally friendly.
- The flower-like gold microstructures can be used as potential SERs substrate.

---

[*] Corresponding author.
E-mail address: kanet.w@chula.ac.th (K. Wongravee).

http://dx.doi.org/10.1016/j.matdes.2017.04.012
Received 31 December 2016; Received in revised form 3 April 2017; Accepted 4 April 2017

1. Introduction

In the past decade, synthesis and fabrication of structural-controlled metal nanostructures have been extensively studied [1,2] due to their potential applications as catalysts [3], sensors [4], and photovoltaic devices [5]. The applications take advantages of the unique size- and shape-dependent properties of the nanostructures which are not existing in the bulk materials or spherical nanostructures [6].

Gold nanostructures have continuously been the centre of attention as it can be engineered into various morphologies, such as spheres [7,8], rods [9,10], wires [11], sheets [12,13], polyhedrons [14], stars [15], and dendrites [16], with distinctively high chemical stability. Among numerous gold nanostructures, flower-like gold structures (FLGSs) with sub-micrometre size consist of various sub-structures such as nanogrooves, sharp edges and tips. The sub-structures provide not only high surface area, but also numbers of nanometre-scale junctions and interconnections, which can serve as hotspots for surface-enhanced Raman spectroscopy (SERS) [17]. The FLGSs have been used as substrates for SERS [18–20] and electrochemical catalysts [21,22]. Furthermore, FLGSs exhibited potential usages as nanocarriers of DNA for cellular uptake, drug or gene delivers and contrasting agents as they provide acceptable cytotoxicity toward cells in toxicological investigations [23,24].

Various techniques for the fabrication of FLGSs have been developed, particularly electrochemical [20,21,25] and wet chemical procedures [18,19,23,24,26,27]. The wet chemical approaches seem to be the most practical choice as the complicated instruments are not required and the process can be easily scaled up. A development of simple, effective, fast and green protocol using environmentally benign method and low cost chemicals is still a challenge. In general, additives (i.e., capping agents, shape-directing agents, and stabilizers) play a pivotal role as it directs the formation of anisotropic nanostructures. The specific absorption of the additive molecules on the particular crystal facets of nanoparticles leads to the modification of the surface energy and consequently alters their growth rate [17] to generate particles with shape selectivity. Various additives (i.e., 2-[4-(2-hydroxyethly)-1-piperazinyl] ethanesulfonic acid (HEPES) [28], dopamine [19], poly(vinyl pyrrolidone) (PVP), sodium dodecyl sulfate (SDS) [27], and gum Arabic [24]) have been employed. Although there were several successful techniques for FLGSs fabrications, only a few demonstrated a basic understanding on the growth mechanism of the FLGSs structure. As discussed in our previous work on the synthesis of gold nanosheets using H_2O_2 as a reducing agent and starch as a green stabilizer [12], a very low concentration of H_2O_2 leads to a selective preservation and growth of high anisotropic gold nanosheets as starch preferentially adsorbed and then prevented the growth on the {111} basal planes. Tridib Kumar Sarma et al. [29]. reported the change in shape from spherical to triangular and to hexagonal particles by increasing initial concentration of $HAuCl_4$ in the presence of H_2O_2 and starch with assisted ultrasonic waves. From the work, it suggested that the ratio of $[H_2O_2]/[HAuCl_4]$ might be an important factor for the shape selectivity. Decreasing of the ratio by increasing concentration of $HAuCl_4$ induced the formation of plate shapes. Interestingly, we found that a complex structure (flower-like structure) could be generated instead of the nanosheets when high concentration H_2O_2 was involved. This indicates that the concentration of H_2O_2 and the high ratio of $[H_2O_2]/[HAuCl_4]$ plays a pivotal role in the complex structure formation. However, in this system, the shape evolution roles of this complex structure are still unclear.

In this study, we report the shape evolution pathways of 3D flower-like gold microstructures (3D-FLGMSs) from the nanosheets. The influences of the concentration of H_2O_2, starch and molar ratio of $[H_2O_2]/[HAuCl_4]$ were systematically investigated in detail. The developed method for the fabrication of 3D-FLGMSs is simple, effective, fast, green and efficient with industrial-scale production capability. To our knowledge, this is the first for the preparation of such a complex microstructure of 3D-FLGMSs using H_2O_2 as a green reducing agent and starch as stabilizer. It could serve as a challenge for the fabrication of microstructures using a simple chemical approach. Furthermore, a potential application of 3D-FLGMSs as SERS substrate was demonstrated.

2. Experimental

2.1. Chemicals

Nitric acid (HNO_3, 65% w/v), hydrochloric acid (HCl, 37% w/v), sodium hydroxide (NaOH), soluble starch and hydrogen peroxide (H_2O_2, 30% w/w) were purchased from Merck (Thailand). All chemicals were analytical grade and were used as received. A solution of tetrachloroauric (III) acid ($HAuCl_4$, 0.5 M) employed as gold metal precursors, was prepared from a stock solution of concentrated $HAuCl_4$ solution. The stock solution was prepared using a method described elsewhere [12]. Prior to use, all glassware and magnetic bars were carefully rinsed with aqua regia in order to get rid of any metallic residuals before cleaning with liquid detergent and rinsing with deionized (DI) water.

2.2. Preparation of 3D-FLGMSs

The 3D-FLGMSs were synthesized by a simple wet chemical method using H_2O_2 as a reducing agent and starch as a stabilizer. Briefly, starch solution (25 mL, 2% w/v) and $HAuCl_4$ (1.25 mL, 0.5 M) were mixed under vigorous stirring for 30 min. The volume of the mixture was adjusted to 33.3 mL using deionized water and stirred for another 30 min before an instantly addition of H_2O_2 (16.7 mL, 30% w/w). The solution was stirred for another 5 min and kept in ambient condition without disturbance. Within 20 min, the golden yellow solution turned colorless with a concomitant formation of dark-brown solid 3D-FLGMSs together with a formation of many oxygen bubbles according to the following redox reaction [12,13].

$$2AuCl_4^-(aq) + 3H_2O_2(aq) \rightarrow 2Au(s) + 3O_2(g) + 8Cl^-(aq) + 6H^+(aq)$$
$$\Delta E^{\circ}_{cell} = +0.307\ \text{V}. \qquad (1)$$

The mixture was kept undisturbed for another 100 min before the separation of 3D-FLGMSs by centrifugation. The 3D-FLGMSs were thoroughly washed with hot DI water before keeping as an aqueous suspension for further characterizations.

2.3. Characterizations

The morphologies of 3D-FLGMSs were observed by a scanning electron microscope (SEM) model JEOL JSM-6510A with accelerating voltage of 20 kV under high vacuum mode. The crystallographic information and the X-ray diffraction (XRD) pattern of 3D-FLGMSs were analysed using an XRD diffractometer model Rigaku D/MAX-2200 (Cu K_α radiation) operated at 40 kV and 30 mA. The diffraction angle was in range of 20–90° with the step size of 0.2°. High-resolution transmission electron micrographs and selected area electron diffraction (SAED) patterns of nanocrystals were monitored by a high-resolution transmission electron microscope (HRTEM) model FEI Tecnai G2 20 using LaB_6 filament with operating of 200 kV.

3. Results and discussion

3.1. H_2O_2 induced 3D-FLGMS formation

H_2O_2 is well known as a strong oxidizing agent. However, its mild reducing capability is suitable for the formation of anisotropic nanostructures, particularly silver nanoplates [30,31] and gold nanosheets [12,13]. The utilization of low concentration H_2O_2 is the key parameter

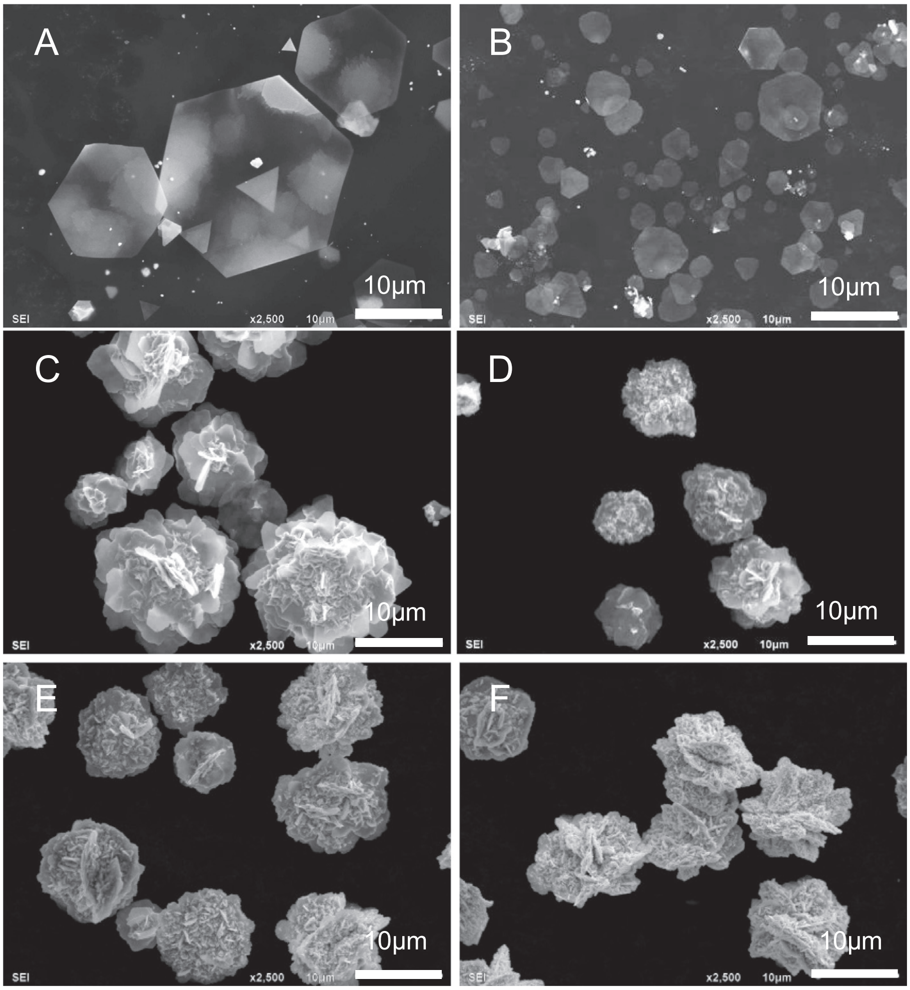

Fig. 1. SEM micrographs show morphological changes of gold microstructures from nanosheets to 3D-FLGMS under the influence of the concentration of H_2O_2: (A) 3.2, (B) 32, (C) 320, (D) 970, (E) 1600 and (F) 3200 mM. The microstructures were synthesized with 2.54 mM $HAuCl_4$ and 1% w/v starch.

as it enables a slow reduction allowing the nucleation and growth of gold nanosheets under a kinetically controlled environment [12]. This phenomenon provides the formation of plate-like seeds that will further grow into nanoplates [32,33]. The liberated oxidizing species (e.g. O_2/Cl^-) act as strong oxidative etchant which selectively dissolves the unstable seeds and preserves the plate-like seeds [12].

When a low concentration of H_2O_2 (3.2 mM) was employed, within 10 h, large gold nanosheets with an average lateral size of 9.2 ± 5.2 μm (thickness of 20–50 nm) were produced as the major product (Fig. 1A). The reaction time was determined by the fading of yellow colour of $HAuCl_4$ solution with the disappearance of O_2 bubbles. The clear solution implied that the $AuCl_4^-$ ions were completely consumed. Increasing H_2O_2 concentration from 3.2 to 32 mM decreases the reaction time to 8 h while small gold nanosheets with an average lateral size of 2.2 ± 1.2 μm were created (Fig. 1B). These observations on the generated gold nanosheets are in a good agreement with our previous work [12]. As a high concentration of reducing agent was employed, the metal ions were rapidly reduced into Au nuclei in the early stage of the reaction. Therefore, the decrease of the particle size can be attributed to the insufficient of metal ions for the growth of gold nanosheets.

Interestingly, when the concentration of H_2O_2 was further increased to 320, 970, 1600, and 3200 mM, the complex structures defined as 3D-FLGMSs were produced within only 1 h (Fig. 1C–F). According to the SEM images, morphology of 3D-FLGMSs is mainly stacking assembly of gold nanosheets (thickness of 40–110 nm, similar to petals of flowers). The morphological evolutions from nanosheets to 3D-FLGMSs were occurred when the concentration of H_2O_2 was over 320 mM. This observation suggests that high concentration of H_2O_2 is the key parameter that triggers the formation of 3D-FLGMSs. An adequate concentration of H_2O_2 is crucial for a rapid reduction that generates a large number of gold nanosheets. The nanosheets later undergo though aggregation and self-organization to 3D-FLGMSs. It should be noted that the surfaces of nanosheets were rough when the H_2O_2 concentration was higher than 1600 mM. These rough surfaces can normally occur in the system with fast growth rate [34].

3.2. Influence of synthesis parameters

As shown in the previous section, high concentration of H_2O_2 would be a crucial factor for the fabrication of 3D-FLGMS structure. We found that the molar ratio of $[H_2O_2]/[HAuCl_4]$ should be higher than ~60 to obtain the 3D-FLGMSs (Fig. S1 and Table S1). Thus, employing the concentration of H_2O_2 3200 mM is preferred for the fabrication of 3D-FLGMSs as it can keep the value of molar ratio of $[H_2O_2]/[HAuCl_4]$ higher than 60 when the concentration of $HAuCl_4$ increases.

The influence of concentrations of $HAuCl_4$ on the fabrication of 3D-FLGMSs were explored by performing the reaction with 1% w/v starch and 3200 mM H_2O_2 using different concentrations of $HAuCl_4$. At low concentration of $HAuCl_4$ (2.54 mM, Fig. 2A1), the 3D-FLGMSs with the average lateral size of 8.2 ± 2.0 μm were produced. At the concentration of $HAuCl_4$ of 12.7 and 25.4 mM, the sufficient concentration of gold ions lead to the extensive growth of 3D-FLGMSs with increased particle sizes to 19.2 ± 3.8 (Fig. 2A2) and 17.4 ± 3.7 μm (Fig. 2A3),

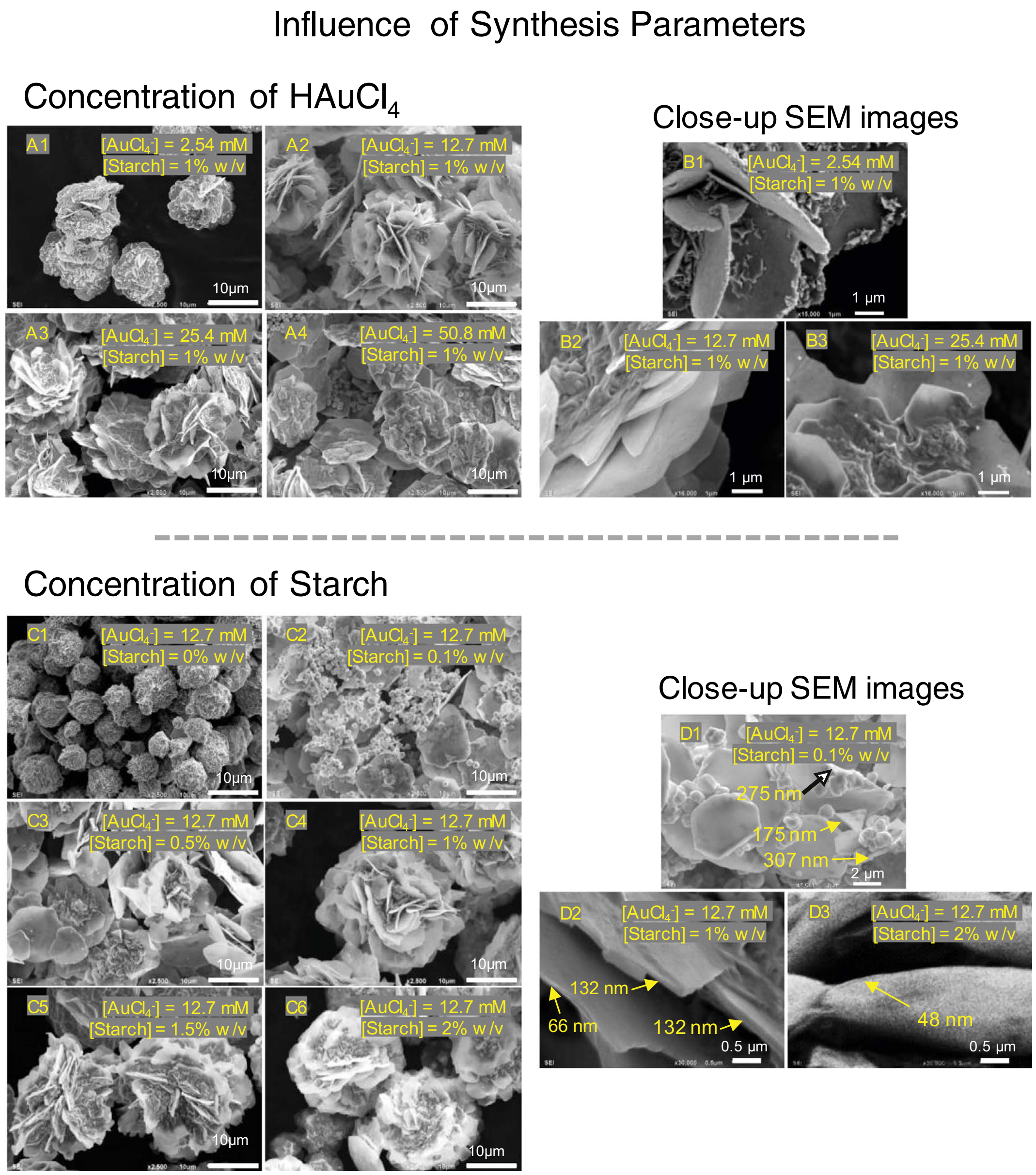

Fig. 2. (A1–A4) SEM images show the effect of concentration of $HAuCl_4$ (2.54–50.8 mM) on the gold microstructures with zoomed SEM images (B1–B3) which present the surfaces morphology of 3D-FLGMSs affected by $HAuCl_4$ at 2.54, 12.7 and 25.4 mM, respectively. (C1–C6) SEM images show the effect of concentration of starch (0–2% w/v) on the gold structure with zoomed SEM images (D1–D3) which present the thickness of microplate/petal-like nanostructures of 3D-FLGMSs affected by concentration of starch at 0.1, 1 and 2% w/v, respectively. For all synthesis conditions, 3200 mM of H_2O_2 were used a reducing agent.

respectively. Surprisingly, the surfaces of the petal became smoother (see Fig. 2B1–B3). This is due to the substantial formation of the oxidative etchant (e.g. O_2/Cl^-) which is capable to dissolve unstable crystal facets and leave the stable facets undisturbed [35,36]. However, when the concentration of $HAuCl_4$ was further increased to 50.8 mM (Fig. 2A4), the irregular-shape gold micro/nanosheets with small number of flattened flowers (thick-irregular-shape gold microsheets) and small quasi-microspheres (particle size of 1.0 ± 0.2 μm) were generated due to an insufficient surface protection. The surface passivation of gold nanostructures can be diminished by the acid hydrolysis of long chain starch at high concentration of $HAuCl_4$ [12,37–39]. The observed phenomena imply that not only the ratio of $[H_2O_2]/[HAuCl_4]$ more than ~60 is required, but also the stabilizing power from starch that are an essential for the formation of the 3D-FLGMSs.

The role of starch passivation power was confirmed by synthesis of 3D-FLGMSs using various concentrations of starch. The concentration of $HAuCl_4$ was fixed at 12.7 mM as the 3D-FLGMSs with smooth surfaces were obtained by this condition. Without starch (Figure 2C1), quasi-microspheres with rough surfaces (average particle size of 5.0 ± 1.6 μm) were the sole product. As the concentration of starch was increased to 0.1% w/v (Fig. 2C2), irregular-shaped gold micro/nanosheets (particle size of 8.9 ± 3.2 μm and thickness of 90–220 nm) and small microspheres (partial size of 1.0 ± 0.2 μm) were produced. When the concentration of starch was increased to 0.5% w/v (Fig. 2C3), the enhanced stabilization enables the formation of irregular gold nanosheets with an average size of 10.8 ± 3.6 μm. The observed phenomena imply that an insufficient stabilization causes aggregations of the microspheres and a non-uniform growth on the basal planes of nanosheets. As greater concentrations of starch were employed (1%–2% w/v, Fig. 2C4–C6), 3D-FLGMSs with lateral size as large as 30 μm were obtained as the main product. An adequate stabilization of starch induced the structural transformation from the quasi-microspheres and the irregular shaped gold micro/nanosheets to 3D-FLGMSs. This observation indicates that starch is not only an essential factor for the formation and growth of the 3D-FLGMSs, but also preventing the formation of microspheres.

There are several reports describing the role of starch in the formation of anisotropic gold nanostructures. Starch serves as an efficient passivating agent that promotes the formation of gold nanosheet [12,40,41]. The selective absorption of starch on the {111} facet of gold nanosheets does not only promote the expansion of the {111} facet, but also regulate the thickness of nanosheets [12,41]. The decrease of the thickness of nanosheets in 3D-FLGMSs was noticed when starch concentration increased (Fig. 2D1–D3). This is due to the increase of passivation power by starch on the surfaces which inhibit the epitaxial growth of nanosheets. Raman spectroscopy was performed to assess the starch residuals on the surfaces of the nanosheets/petals after cleaning with DI water, hot DI water, and alkaline-peroxide solution (i.e., a strong bleaching solution of 30% H_2O_2 adjusted to pH 14 by 3 M NaOH). After washing with cold and hot DI water, starch molecules still remained on the surfaces (Fig. S2). However, after cleaning with alkaline peroxide solution, the fingerprint of starch was vanished. This can imply that although starch had a very good adhesion on the surfaces of 3D-FLGMS petals, however, it can be easily removed to obtain the surface-clean 3D-FLGMSs.

As revealed in SEM images, the complex microstructures of 3D-FLGMSs would be constructed from the assembly of nanosheets. Generally, gold nanosheets exhibited the specific {111} facet exposure. The high exposure of {111} crystal facet can be revealed as the extremely high {111} intensity (Fig. S3B). Very high values of intensity ratios of {111}/{200} and {111}/{220} suggest that the {111} facet is parallel to the surface of substrate during the XRD characterization (Table S2) [12,42]. In the case of 3D-FLGMSs, the XRD patterns (Fig. S3A) clearly indicates the characteristic of the face-centered cubic (fcc) crystal of gold assigning to {111}, {200}, {220}, {311}, and {222} facets which perfectly match the JCPDS 04-0784 standard file (Fig. S4) [19,42]. Compared with other facet intensities, the high intensity of {111} facet was noticed which correspond to the highly exposed {111} facet on the obtained structures. It should be noted that the 3D-FLGMSs show lower values of intensity ratio of {111}/{200} and {111}/{220} compared to those of nanosheet structures. This can be attributed the diverse-oriented nanosheets of the 3D-FLGMSs on the surface of substrate during the XRD characterization.

3.3. Growth mechanism of 3D-FLGMSs

In our synthesis system, the time-lapse digital photographs revealed the relative fast reaction as indicated by a complete consumption of gold ions within 20 min (i.e., the yellow solution turned colorless) together with the observation of tiny particles (Fig. S5A–D). It is evidence that the reduction of Au(III) to Au(I) and Au(III) to Au(0) simultaneously occurs due to the electropositive reaction [12,43–46]. After 24 min, the rapid appearances of red-brown suspensions together with a burst of oxygen bubbles represent the rapid formation and growth of 3D-FLGMSs (Fig. S5E–K). Although the gold ion precursors were completely consumed within first 20 min, the presence of oxygen bubbles was still observed. This observation implies that the reduction of gold ions by H_2O_2 still instantly occurs. The generated gold ions, which serve as metal supply for the growth of 3D-FLGMSs, might be from the dissolution of the unstable crystal facets in 3D-FLGMSs by a strong oxidative species (O_2/Cl^-) [35]. Corroboration to the time-lapse digital photographs, we gained more insight understanding on the growth mechanism of the 3D-FLGMSs by performing time-dependent SEM observations. As shown in Fig. 3A–C, the small gold nanosheets formed at the early stage and later grew into larger primary gold nanosheets. The existing of jagged edges in small gold nanosheets (Fig. 3A) indicates that the growth of 3D-FLGMSs might involve the crystal growth via oriented attachment (OA) resulting in the lateral expansion of the nanosheets [47]. Meanwhile, the epitaxial growth on the surfaces of former nanosheets could develop into new nanosheets (nanopetals), as shown in Fig. 3D. The formation of starch-bound new nanosheets was later outgrowing from the nucleation sites on the basal plan of the former nanosheets (Fig. 3E). The development of nanopetals continued until complete structures of 3D-FLGMSs were obtained. The rough surfaces of nanopetals on 3D-FLGMSs can be recognized. They might come from the uncompleted growth of the sheets as the metal ion supply was exhausted.

We further performed HRTEM characterization to acquire the evidence of the formation of 3D-FLGMSs. The 3D-FLGMSs were disassembled to become small fractals of petal-like nanostructures using high power ultrasonication (Fig. S6). Fig. 4A and B show a TEM image and its corresponding SAED pattern of a petal-like nanostructure from 3D-FLGMSs, respectively. The hexagonal diffraction pattern was obtained by projecting the electron beam perpendicular to the basal plane of petal-like nanostructures. Bragg reflections of the Au face-centered cubic (fcc) crystal structure clearly shows the allowed {220} and the forbidden 1/3{422} planes which typically exist with the presence of twinned planes that are parallel to the {111} surfaces of nanoplates or nanosheets [12,13,48]. The results suggest that the basal plane of petal-like nanostructures is actually {111} facet. Fig. 4C shows the TEM image of a petal-like nanostructures of growing 3D-FLGMSs. HRTEM image with lattice fringe resolution at the edge of the growing nanopetal reveal the lattice fringe of ~2.5 Å which correspond to 1/3{422} diffractions obtained from SAED. The stacking faults on the lattice fringe were noticed (Fig. 4D). This shows that the growth of nanocrystal undergoes OA process which involves the direct coalescence of nanoparticles. This attachment provides the defects in the crystal structure, including twin, stacking faults and misorientation, which is possible to be preserved in the following growth process [49]. Furthermore, the presence of strong surface adsorption by starch during the growth can promote OA in the initial growth state [49]. Thus, the observations of the stacking faults in the nanopetals suggest that the growth of 3D-FLGMSs mainly involves the OA mechanism.

Based on the observed evidences from time-dependent study and time-lapse digital captures, we propose the growth mechanism of 3D-FLGMSs as shown in Fig. 5. At the very early step, gold ions are rapidly reduced by H_2O_2 and subsequently grow to small gold nanosheets with starch-bounded surfaces. The massive generation of gold nanosheets, which is caused by employing of high concentration of metal precursor and reducing agent (H_2O_2), leads to the rise of total surface energy in the system. To minimize the overall surface energy, gold nanosheets undergo OA to form the large primary gold nanosheets preserving its lowest surface energy {111} facet [50,51]. In addition, the crystalline boundaries (defects) created from the imperfect OA could act as active sites for heterogeneous growth [52,53]. With an assistance of starch passivation, the new nanopetals could grow on former nanosheets. Alternative dissolution process of the nanosheets was also occurred by oxidative etching mechanism on the unstable facets of nanosheets. This process generates the gold ions to the system, but at the same time, they are also consequently used for the growth process. After the increased number of nanopetals, the formation of the complete structures of 3D-FLGMS is finally achieved.

3.4. SERS activity on 3D-FLGMS

As discussed in the previous sections, the facile method for the fabrication of 3D-FLGMSs has been demonstrated. The developed method provides a 100% conversion of gold ions with good reproduced structures (Figs. S7 and S8). Moreover, we further demonstrate potential applications of 3D-FLGMSs. There has been reported that the complex nanostructures, in particular dendrite structures, can be used as potential SERS substrates as their sharp corners, edges, and nanometre-scale junctions could create SERS hot spots [17,54]. Due to the complex morphologies of 3D-FLGMSs, thus, we interest to explore the application of 3D-FLGMSs as a SERS substrate. 3D-FLGMSs exhibits

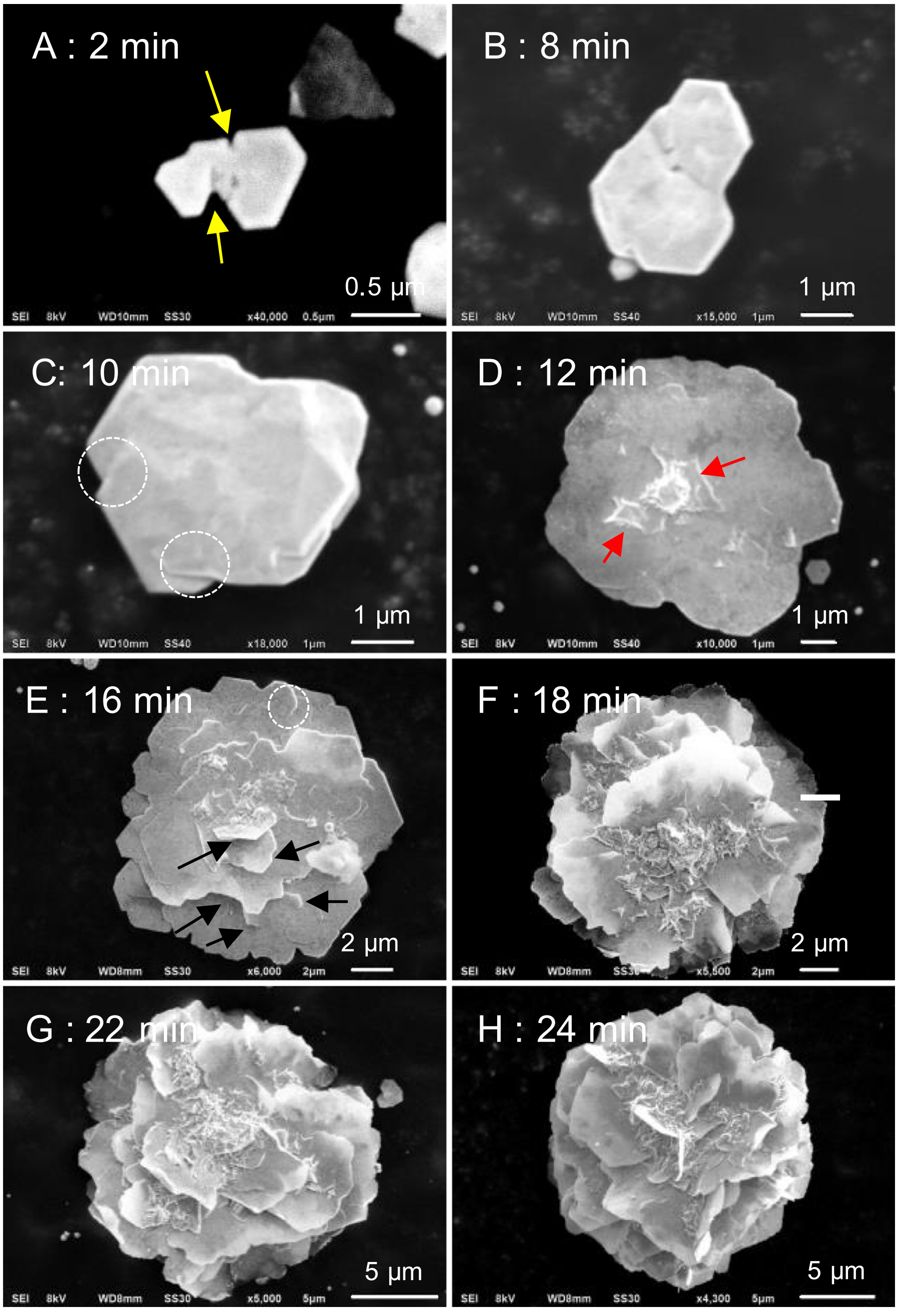

Fig. 3. Time-dependent SEM micrographs show the development of 3D-FLGMSs. The 3D-FLGMSs were synthesized using 25.4 mM $HAuCl_4$ and 3200 mM H_2O_2 in 1% w/v starch solution. The arrows in (A) indicate jagged edges, those in (D) indicate the epitaxial growth on the basal plan of nanosheets, while those in (E) indicate the petals outgrowth from the surfaces of the basal plan of nanosheets. The circles in (C) and (E) indicate the overlapped parts of nanosheets.

not only the micrometre-size complex morphology but the great advantages as it can be easily handle under microscope as the sensing region can be precisely determined. Moreover, only small volume in sub-microliter range of the target analyte is required to be used in the detection. To investigate the SERS activity, 3D-FLGMSs were cleaned with an alkaline-peroxide solution to achieve starch-free surfaces. The aqueous-dispersed 3D-FLGMSs were dropped on aluminium-coated glass substrates. After drying in a desiccator for 24 h, Rhodamine 6G (R6G) with various concentrations (1 nM–10 μM) were dropped on 3D-FLGMSs and dried at room temperature. A 10 μM of R6G on aluminium foil was used as a reference. SERS spectra were recorded using the excitation wavelength at 532 nm with the laser power of 1 mW, while the exposure time and the number exposure were fixed at 1 ms with 32 scans, respectively.

Fig. 6 shows the SERS spectra of R6G on flat aluminium substrates. Without 3D-FLGMSs, Raman signal of 10 μM R6G cannot be observed. Meanwhile, the well-defined vibrational fingerprints of R6G, which comprise of C—C—C in-plane bending (615 cm^{-1}), C—H out-of-plane bending (775 cm^{-1}), C—H in-plane bending (1126 and 1185 cm^{-1}), C—O—C stretching (1314 cm^{-1}), and C—C stretching of aromatic ring (1363, 1512, 1575, and 1651 cm^{-1}) [55], were clearly observed from the SERS spectra of R6G deposited on 3D-FLGMSs. A further investigation was conducted in order to explore the lowest concentration of R6G that can be detected when using 3D-FLGMSs as SERS substrates. The SERS signal at 615 cm^{-1} was employed as it showed distinct feature with the highest intensity. The Raman shift at 615 cm^{-1} was observed even the concentration of R6G is as low as 100 nM. In addition, SERS activity of material depends on the number of hot spots in a specific

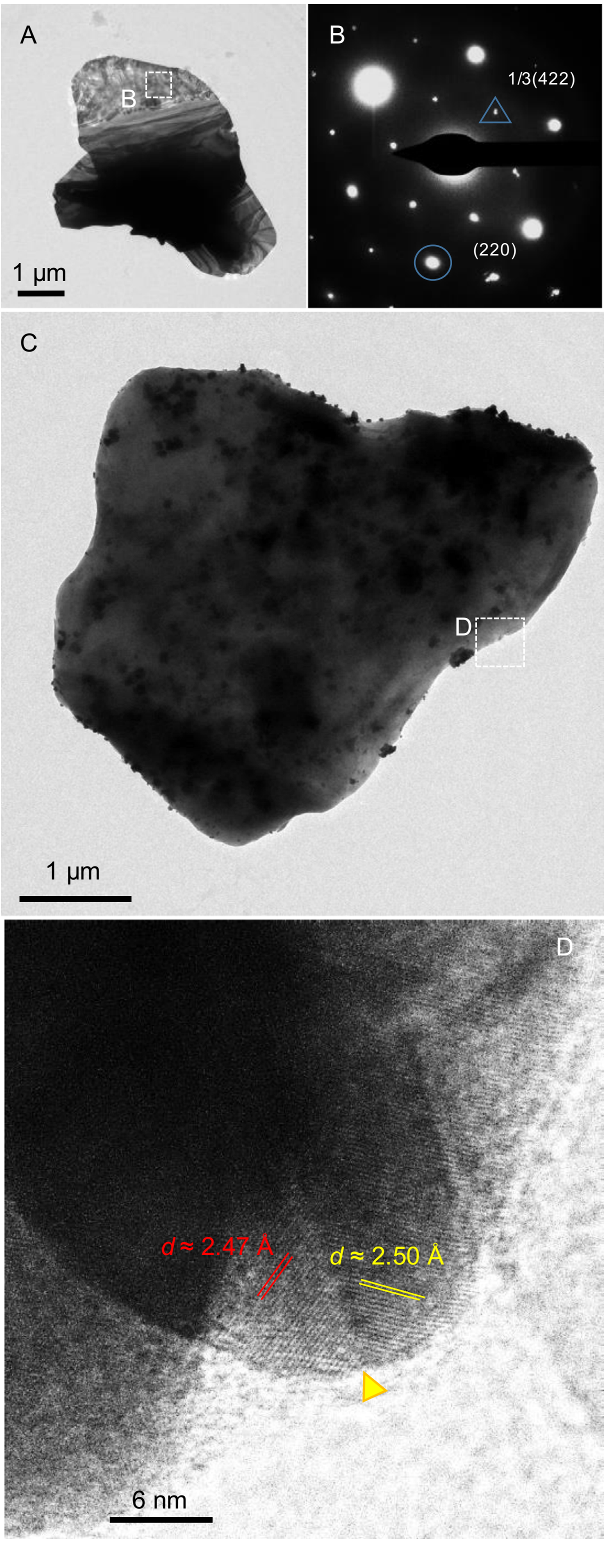

Fig. 4. (A) and (C) TEM images of small petal-like nanostructures of 3D-FLGMSs and growing 3D-FLGMSs, respectively. (B) The corresponding SAED pattern in (A). (D) HRTEM image with lattice fringe resolution at the edge of growing petal-like nanofractals of 3D-FLGMSs. The yellow arrowhead indicates the stacking faults. (For interpretation of the references to colour in this figure legend, the reader is referred to the web version of this article.)

surface area [56,57]. Although Brunauer–Emmett–Teller (BET) analysis on our 3D-FLGMSs revealed that surface area is rather low (0.51 $m^2 \cdot g^{-1}$) but the enhancement of the Raman signal of R6G on the 3D-FLGMS could be attributed to the SERS hot spots created by the

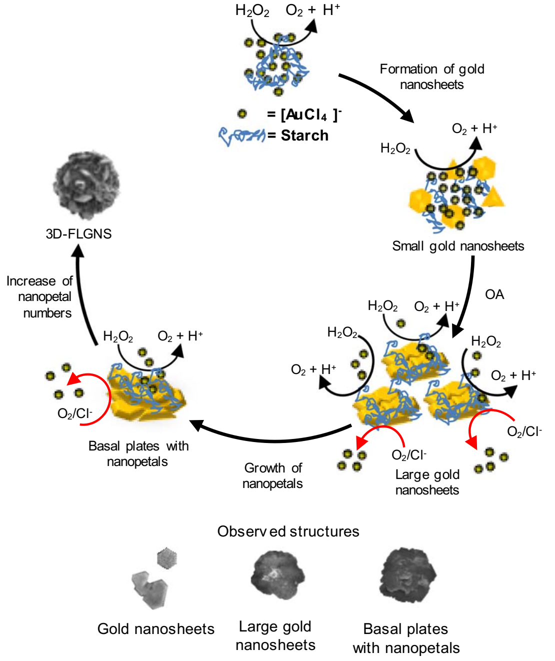

Fig. 5. Scheme represents the proposed growth mechanism of 3D-FLGMS. Black arrows indicate the growing of 3D-FLGMS while red arrows present the etching process of 3D-FLGMS by O_2/Cl^-. (For interpretation of the references to colour in this figure legend, the reader is referred to the web version of this article.)

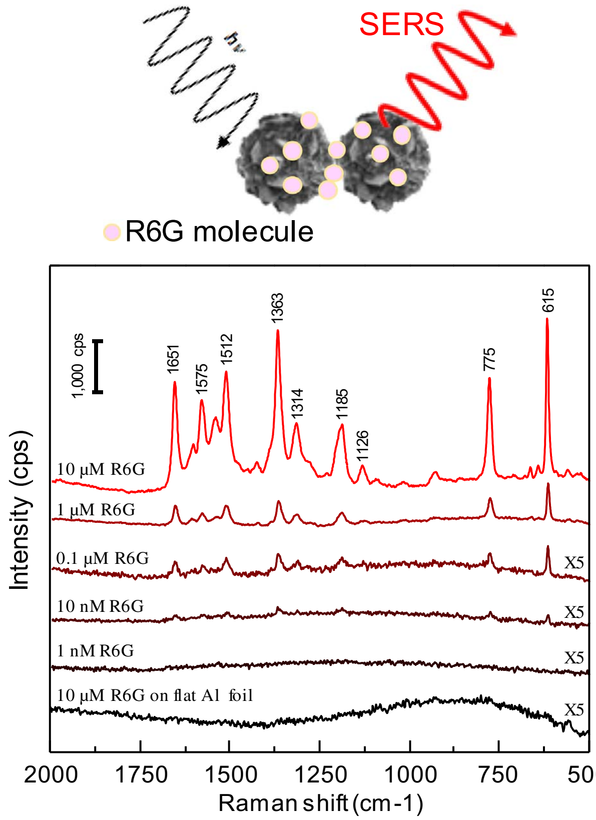

Fig. 6. SERS spectra of R6G, with different concentrations, deposited on the surfaces of 3D-FLGMS and Raman spectrum of R6G deposited on flat aluminium foil with an inset schematic illustrate the SERS of R6G on surfaces of 3D-FLGMS.

overlapping of the petal-like structures between the two flowers, the 3D nanogaps located between adjacent nanosheets [58] and the nanometre-scale surface roughness [59]. This preliminary investigation of

SERS activity of 3D-FLGMSs suggests that the fabricated 3D-FLGMSs can be used as an efficient SERS substrate for trace chemical analysis.

4. Conclusions

In summary, we have successfully developed a simple and efficient synthetic method for the fabrication of 3D-FLGMSs using H_2O_2 as the green reducing agent and starch as the stabilizer. The influence of the H_2O_2 and starch on the size, morphology and structural evolution of 3D-FLGMSs were systematically investigated. Shape evolution of 3D-FLGMSs using the green chemicals was revealed. By performing the synthesis at high concentration of H_2O_2, the formation of 3D-FLGMSs with the size as large as 30 μm can be achieved in a short period. Adequate amount of starch is essential for the formation of 3D-FLGMSs as it functions as a surface-passivating agent while promoting the growth of nanopetals. An insufficient stabilization leads to the formation of flat 3D-FLGMSs with large number of quasi-microspheres. Based on time-dependent study, the growth of 3D-FLGMSs involved the formation of gold nanosheets, self-assembly of gold nanosheets via OA, and epitaxial growth on the surfaces of gold nanosheets. The preliminary investigation on the application of 3D-FLGMSs as SERS substrates suggests that 3D-FLGMSs can be used as efficient SERS substrates.

Author contributions

The manuscript was written through contributions of all authors. All authors have given approval to the final version of the manuscript.

Notes

The authors declare no competing financial interest.

Acknowledgements

This research was supported by National Research University Project, Office of Higher Education Commission and Chulalongkorn University (WCU-58-008-FW). S. Nootchanat is a postdoctoral fellow supported by Rachadapisek Sompote Endowment Fund, Chulalongkorn University. K. Wongravee thanks Grant for International Research Integration: Chula Research scholar, Ratchadaphiseksomphot Endowment Fund and Thailand Research Fund (TRG 5880238). Finally, authors would like to delicate the manuscript for “In remembrance of His Majesty King Bhumibol Adulyadej (1927–2016), for his life-time dedication to Thailand”.

Appendix A. Supplementary data

The Supporting Information is available including (1) SEM micrographs showing the influence of concentration of $HAuCl_4$ and H_2O_2 on morphology of gold micro/nanostructures, (2) Table illustrates the relationship of molar ratio of $[H_2O_2]/[HAuCl_4]$ and the morphology of gold micro/nanostructures, (3) Raman spectra indicating the present of starch molecule on the surfaces of 3D-FLGMS, (4) XRD patterns of mixed shape H_2O_2-reduced gold microparticles, gold nanosheets and 3D-FLGMS, (5) The standard XRD pattern of gold (JCPDS 04-0748) and (6) Time-lapse digital photographs indicating large-scale synthesis of 3D-FLGMS, (7) Digital photographs represent the colour of supernatants from the 3D-FLGMS solution, and (8) SEM images show the morphology of 3D-FLGMSs obtained from five different production batches. Supplementary data associated with this article can be found in the online version, at doi:http://dx.doi.org/10.1016/j.matdes.2017.04.012.

References

[1] Z. Wu, S. Yang, W. Wu, Shape control of inorganic nanoparticles from solution, Nano 8 (2016) 1237–1259.

[2] H. Duan, D. Wang, Y. Li, Green chemistry for nanoparticle synthesis, Chem. Soc. Rev. 44 (2015) 5778–5792.

[3] X. Shen, W. Liu, X. Gao, Z. Lu, X. Wu, X. Gao, Mechanisms of oxidase and superoxide dismutation-like activities of gold, silver, platinum, and palladium, and their alloys: a general way to the activation of molecular oxygen, J. Am. Chem. Soc. 137 (2015) 15882–15891.

[4] B. Sepúlveda, P.C. Angelomé, L.M. Lechuga, L.M. Liz-Marzán, LSPR-based nanobiosensors, Nano Today 4 (2009) 244–251.

[5] Z. Lu, X. Pan, Y. Ma, Y. Li, L. Zheng, D. Zhang, Q. Xu, Z. Chen, S. Wang, B. Qu, F. Liu, Y. Huang, L. Xiao, Q. Gong, Plasmonic-enhanced perovskite solar cells using alloy popcorn nanoparticles, RSC Adv. 5 (2015) 11175–11179.

[6] M. Bechelany, P. Brodard, J. Elias, A. Brioude, J. Michler, L. Philippe, Simple synthetic route for SERS-active gold nanoparticles substrate with controlled shape and organization, Langmuir 26 (2010) 14364–14371.

[7] N.G. Bastús, J. Comenge, V.C. Puntes, Kinetically controlled seeded growth synthesis of citrate-stabilized gold nanoparticles of up to 200 nm: size focusing versus Ostwald ripening, Langmuir 27 (2011) 11098–11105.

[8] J. Kimling, M. Maier, B. Okenve, V. Kotaidis, H. Ballot, A. Plech, Turkevich method for gold nanoparticle synthesis revisited, J. Phys. Chem. B 110 (2006) 15700–15707.

[9] W. Xiong, D. Sikdar, L.W. Yap, P. Guo, M. Premaratne, X. Li, W. Cheng, Matryoshka-caged gold nanorods: synthesis, plasmonic properties, and catalytic activity, Nano Res. 9 (2016) 415–423.

[10] Y. Huang, K. Xia, N. He, Z. Lu, L. Zhang, Y. Deng, L. Nie, Size-tunable synthesis of gold nanorods using pyrogallol as a reducing agent, Sci. China: Chem. 58 (2015) 1759–1765.

[11] A. Loubat, L.-M. Lacroix, A. Robert, M. Impéror-Clerc, R. Poteau, L. Maron, R. Arenal, B. Pansu, G. Viau, Ultrathin gold nanowires: soft-templating versus liquid phase synthesis, a quantitative study, J. Phys. Chem. C 119 (2015) 4422–4430.

[12] S. Nootchanat, C. Thammacharoen, B. Lohwongwatana, S. Ekgasit, Formation of large H_2O_2-reduced gold nanosheets via starch-induced two-dimensional oriented attachment, RSC Adv. 3 (2013) 3707–3716.

[13] B. Tangeysh, K. Moore Tibbetts, J.H. Odhner, B.B. Wayland, R.J. Levis, Triangular gold nanoplate growth by oriented attachment of Au seeds generated by strong field laser reduction, Nano Lett. 15 (2015) 3377–3382.

[14] Y. Liu, J. Zhou, X. Yuan, T. Jiang, L. Petti, L. Zhou, P. Mormile, Hydrothermal synthesis of gold polyhedral nanocrystals by varying surfactant concentration and their LSPR and SERS properties, RSC Adv. 5 (2015) 68668–68675.

[15] W. Niu, Y.A.A. Chua, W. Zhang, H. Huang, X. Lu, Highly symmetric gold nanostars: crystallographic control and surface-enhanced Raman scattering property, J. Am. Chem. Soc. 137 (2015) 10460–10463.

[16] T. Xia, H. Luo, S. Wang, J. Liu, G. Yu, R. Wang, Large-scale synthesis of gold dendritic nanostructures for surface enhanced Raman scattering, CrystEngComm 17 (2015) 4200–4204.

[17] D. Huang, X. Bai, L. Zheng, Ultrafast preparation of three-dimensional dendritic gold nanostructures in aqueous solution and their applications in catalysis and SERS, J. Phys. Chem. C 115 (2011) 14641–14647.

[18] W. Jia, J. Li, G. Lin, L. Jiang, Two-step synthesis of narrow size distribution nanoflowers using a tree-type multi-amine-head surfactant as a template, Cryst. Growth Des. 11 (2011) 3822–3827.

[19] S. Yi, L. Sun, S.C. Lenaghan, Y. Wang, X. Chong, Z. Zhang, M. Zhang, One-step synthesis of dendritic gold nanoflowers with high surface-enhanced Raman scattering (SERS) properties, RSC Adv. 3 (2013) 10139–10144.

[20] K. Ju-Hyun, K. Taejoon, Y. Seung Min, L. Sang Yup, K. Bongsoo, C. Yang-Kyu, A well-ordered flower-like gold nanostructure for integrated sensors via surface-enhanced Raman scattering, Nanotechnology 20 (2009) 235302.

[21] A.K. Das, C.R. Raj, Facile growth of flower-like Au nanocrystals and electroanalysis of biomolecules, J. Electroanal. Chem. 638 (2010) 189–194.

[22] B.K. Jena, C.R. Raj, Synthesis of flower-like gold nanoparticles and their electrocatalytic activity towards the oxidation of methanol and the reduction of oxygen, Langmuir 23 (2007) 4064–4070.

[23] Z. Wang, J. Zhang, J.M. Ekman, P.J.A. Kenis, Y. Lu, DNA-mediated control of metal nanoparticle shape: one-pot synthesis and cellular uptake of highly stable and functional gold nanoflowers, Nano Lett. 10 (2010) 1886–1891.

[24] L. Wang, C.-H. Liu, Y. Nemoto, N. Fukata, K.C.W. Wu, Y. Yamauchi, Rapid synthesis of biocompatible gold nanoflowers with tailored surface textures with the assistance of amino acid molecules, RSC Adv. 2 (2012) 4608–4611.

[25] M. Li, G. Zhao, R. Geng, H. Hu, Facile electrocatalytic redox of hemoglobin by flower-like gold nanoparticles on boron-doped diamond surface, Bioelectrochemistry 74 (2008) 217–221.

[26] W. Wang, X. Yang, H. Cui, Growth mechanism of flowerlike gold nanostructures: surface plasmon resonance (SPR) and resonance rayleigh scattering (RRS) approaches to growth monitoring, J. Phys. Chem. C 112 (2008) 16348–16353.

[27] Y. Ren, C. Xu, M. Wu, M. Niu, Y. Fang, Controlled synthesis of gold nanoflowers assisted by poly(vinyl pyrrolidone)–sodium dodecyl sulfate aggregations, Colloids Surf. A Physicochem. Eng. Asp. 380 (2011) 222–228.

[28] J. Xie, Q. Zhang, J.Y. Lee, D.I.C. Wang, The synthesis of SERS-active gold nanoflower tags for in vivo applications, ACS Nano 2 (2008) 2473–2480.

[29] T.K. Sarma, A. Chattopadhyay, Starch-mediated shape-selective synthesis of Au nanoparticles with tunable longitudinal plasmon resonance, Langmuir 20 (2004) 3520–3524.

[30] T. Parnklang, B. Lamlua, H. Gatemala, C. Thammacharoen, S. Kuimalee, B. Lohwongwatana, S. Ekgasit, Shape transformation of silver nanospheres to silver nanoplates induced by redox reaction of hydrogen peroxide, Mater. Chem. Phys. 153 (2015) 127–134.
[31] T. Parnklang, C. Lertvachirapaiboon, P. Pienpinijtham, K. Wongravee, C. Thammacharoen, S. Ekgasit, H_2O_2-triggered shape transformation of silver nanospheres to nanoprisms with controllable longitudinal LSPR wavelengths, RSC Adv. 3 (2013) 12886–12894.
[32] B. Lim, P.H.C. Camargo, Y. Xia, Mechanistic study of the synthesis of au nanotadpoles, nanokites, and microplates by reducing aqueous $HAuCl_4$ with poly (vinyl pyrrolidone), Langmuir 24 (2008) 10437–10442.
[33] Y. Xiong, Y. Xia, Shape-controlled synthesis of metal nanostructures: the case of palladium, Adv. Mater. 19 (2007) 3385–3391.
[34] T.-S. Deng, J.E.S. van der Hoeven, A.O. Yalcin, H.W. Zandbergen, M.A. van Huis, A. van Blaaderen, Oxidative etching and metal overgrowth of gold nanorods within mesoporous silica shells, Chem. Mater. 27 (2015) 7196–7203.
[35] G. Mettela, G.U. Kulkarni, Facet selective etching of Au microcrystallites, Nano Res. 8 (2015) 2925–2934.
[36] Z. Guo, Y. Zhang, A. Xu, M. Wang, L. Huang, K. Xu, N. Gu, Layered assemblies of single crystal gold nanoplates: direct room temperature synthesis and mechanistic study, J. Phys. Chem. C 112 (2008) 12638–12645.
[37] L. Kunlan, X. Lixin, L. Jun, P. Jun, C. Guoying, X. Zuwei, Salt-assisted acid hydrolysis of starch to D-glucose under microwave irradiation, Carbohydr. Res. 331 (2001) 9–12.
[38] H.-J. Chung, H.-Y. Jeong, S.-T. Lim, Effects of acid hydrolysis and defatting on crystallinity and pasting properties of freeze-thawed high amylose corn starch, Carbohydr. Polym. 54 (2003) 449–455.
[39] W. Shujun, Y. Jinglin, Y. Jiugao, P. Jiping, L. Hongyan, Structure characterization of c-type starch granule by acid hydrolysis, Food Hydrocoll. 22 (2008) 1283–1290.
[40] P. Pienpinijtham, X.X. Han, T. Suzuki, C. Thammacharoen, S. Ekgasit, Y. Ozaki, Micrometer-sized gold nanoplates: starch-mediated photochemical reduction synthesis and possibility of application to tip-enhanced Raman scattering (TERS), Phys. Chem. Chem. Phys. 14 (2012) 9636–9641.
[41] H. Hu, J. Zhou, Q. Kong, C. Li, Two-dimensional Au nanocrystals: shape/size controlling synthesis, morphologies, and applications, Part. Part. Syst. Charact. 32 (2015) 796–808.
[42] X. Sun, S. Dong, E. Wang, High-yield synthesis of large single-crystalline gold nanoplates through a polyamine process, Langmuir 21 (2005) 4710–4712.
[43] L. Scarabelli, M. Grzelczak, L.M. Liz-Marzán, Tuning gold nanorod synthesis through prereduction with salicylic acid, Chem. Mater. 25 (2013) 4232–4238.
[44] L. Scarabelli, M. Coronado-Puchau, J.J. Giner-Casares, J. Langer, L.M. Liz-Marzán, Monodisperse gold nanotriangles: size control, large-scale self-assembly, and performance in surface-enhanced Raman scattering, ACS Nano 8 (2014) 5833–5842.
[45] J. Rodríguez-Fernández, J. Pérez-Juste, P. Mulvaney, L.M. Liz-Marzán, Spatially-directed oxidation of gold nanoparticles by Au(iii) − CTAB complexes, J. Phys. Chem. B 109 (2005) 14257–14261.
[46] J. Pérez-Juste, L.M. Liz-Marzán, S. Carnie, D.Y.C. Chan, P. Mulvaney, Electric-field-directed growth of gold nanorods in aqueous surfactant solutions, Adv. Funct. Mater. 14 (2004) 571–579.
[47] Z. Liu, H. Zhou, Y.S. Lim, J.-H. Song, L. Piao, S.-H. Kim, Synthesis of silver nanoplates by two-dimensional oriented attachment, Langmuir 28 (2012) 9244–9249.
[48] T. Minami, R. Nishiyabu, M. Iyoda, Y. Kubo, Shape-controllable gold nanocrystallization using an amphiphilic polythiophene, Chem. Commun. 46 (2010) 8603–8605.
[49] J. Zhang, F. Huang, Z. Lin, Progress of nanocrystalline growth kinetics based on oriented attachment, Nano 2 (2010) 18–34.
[50] X. Xue, R.L. Penn, E.R. Leite, F. Huang, Z. Lin, Crystal growth by oriented attachment: kinetic models and control factors, CrystEngComm 16 (2014) 1419–1429.
[51] M. Niederberger, H. Colfen, Oriented attachment and mesocrystals: non-classical crystallization mechanisms based on nanoparticle assembly, Phys. Chem. Chem. Phys. 8 (2006) 3271–3287.
[52] R.L. Penn, J.F. Banfield, Imperfect oriented attachment: dislocation generation in defect-free nanocrystals, Science 281 (1998) 969–971.
[53] Y. Sun, L. Wang, X. Yu, K. Chen, Facile synthesis of flower-like 3D ZnO superstructures via solution route, CrystEngComm 14 (2012) 3199–3204.
[54] D. Joseph, K.E. Geckeler, Surfactant-directed multiple anisotropic gold nanostructures: synthesis and surface-enhanced Raman scattering, Langmuir 25 (2009) 13224–13231.
[55] T. Vosgröne, A.J. Meixner, Surface- and resonance-enhanced micro-Raman spectroscopy of xanthene dyes: from the ensemble to single molecules, ChemPhysChem 6 (2005) 154–163.
[56] P. Pienpinijtham, P. Sornprasit, K. Wongravee, C. Thammacharoen, S. Ekgasit, Gold microsheets having nano/microporous structures fabricated by ultrasonic-assisted cyclic galvanic replacement, RSC Adv. 5 (2015) 78315–78323.
[57] D. Radziuk, H. Moehwald, Prospects for plasmonic hot spots in single molecule SERS towards the chemical imaging of live cells, Phys. Chem. Chem. Phys. 17 (2015) 21072–21093.
[58] K. Jung, J. Hahn, S. In, Y. Bae, H. Lee, P.V. Pikhitsa, K. Ahn, K. Ha, J.-K. Lee, N. Park, M. Choi, Hotspot-engineered 3D multipetal flower assemblies for surface-enhanced Raman spectroscopy, Adv. Mater. 26 (2014) 5924–5929.
[59] H. Liang, Z. Li, W. Wang, Y. Wu, H. Xu, Highly surface-roughened “flower-like” silver nanoparticles for extremely sensitive substrates of surface-enhanced Raman scattering, Adv. Mater. 21 (2009) 4614–4618.

Supplementary Material

Shape evolution of 3D Flower-like Gold Microstructures from Gold Nanosheets via Oriented Attachment

Supeera Nootchanat[a], Chutiparn Lertvachirapaiboon[b], Vittaya Amornkitbamrung[c] Pikaned Uppachai[d], Sanong Ekgasit[a] and Kanet Wongravee*, [a]

[a] Sensor Research Unit, Department of Chemistry, Faculty of Science, Chulalongkorn University, 254 Phyathai Road, Patumwan, Bangkok 10330, Thailand

[b] Graduate School of Science and Technology, Niigata University, 8050, Ikarashi 2-nocho, Nishi-ku, Niigata 950-2181, Japan

[c] Integrated Nanotechnology Research Center, Khon Kaen University, Khon Kaen 40000 Thailand

[d] Department of Applied Physics, Faculty of Engineering, Rajamangala University of Technology Isan, Khon Kaen Campus, Khon Kaen 40000, Thailand

Keywords: flower-like gold nanostructures, gold nanosheets, hydrogen peroxide, oriented attachment, nanostructures, SERS.

Table S1 Molar ratios of $[H_2O_2]/[HAuCl_4]$ for each synthesis condition. The gold micro/nanostructures were synthesized in 1% w/v. Labeled color represents the observed gold micro/nanostructure for each synthesis condition.

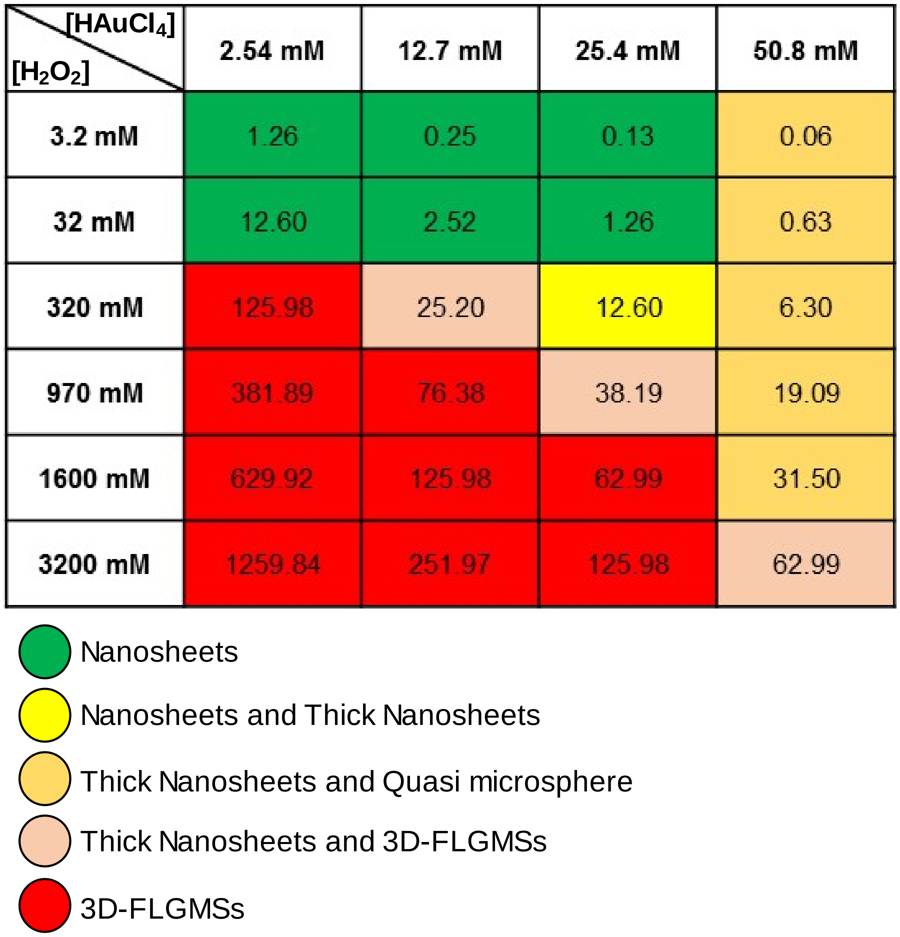

$[H_2O_2]$ \ $[HAuCl_4]$	2.54 mM	12.7 mM	25.4 mM	50.8 mM
3.2 mM	1.26	0.25	0.13	0.06
32 mM	12.60	2.52	1.26	0.63
320 mM	125.98	25.20	12.60	6.30
970 mM	381.89	76.38	38.19	19.09
1600 mM	629.92	125.98	62.99	31.50
3200 mM	1259.84	251.97	125.98	62.99

● Nanosheets

● Nanosheets and Thick Nanosheets

● Thick Nanosheets and Quasi microsphere

● Thick Nanosheets and 3D-FLGMSs

● 3D-FLGMSs

Table S2 the ratios of {111}/{200} and {111}/{220} of different gold micro/nanostructures.

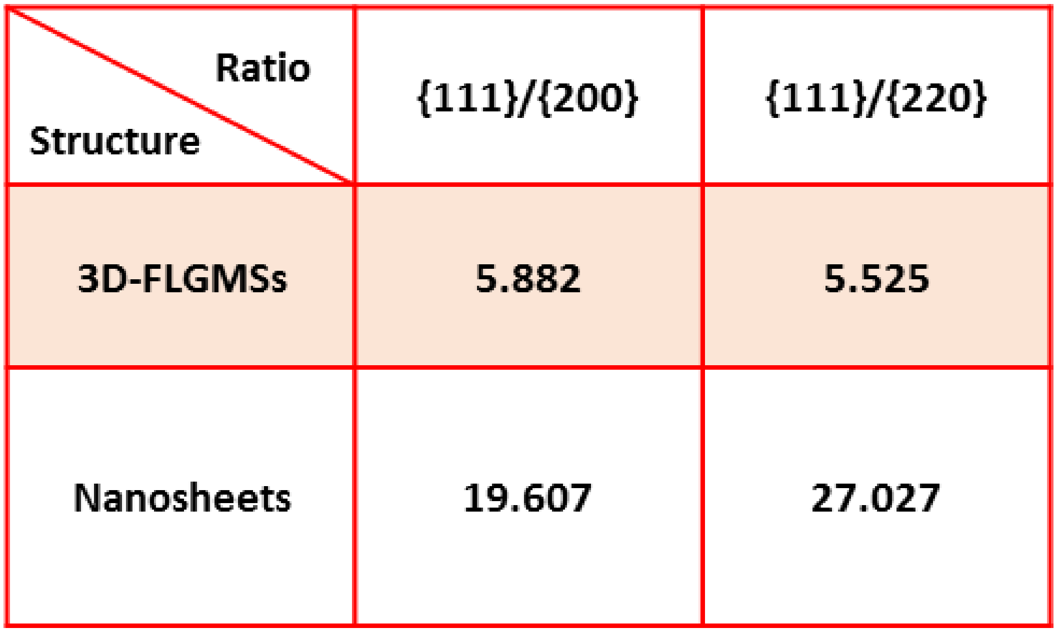

Ratio Structure	{111}/{200}	{111}/{220}
3D-FLGMSs	5.882	5.525
Nanosheets	19.607	27.027

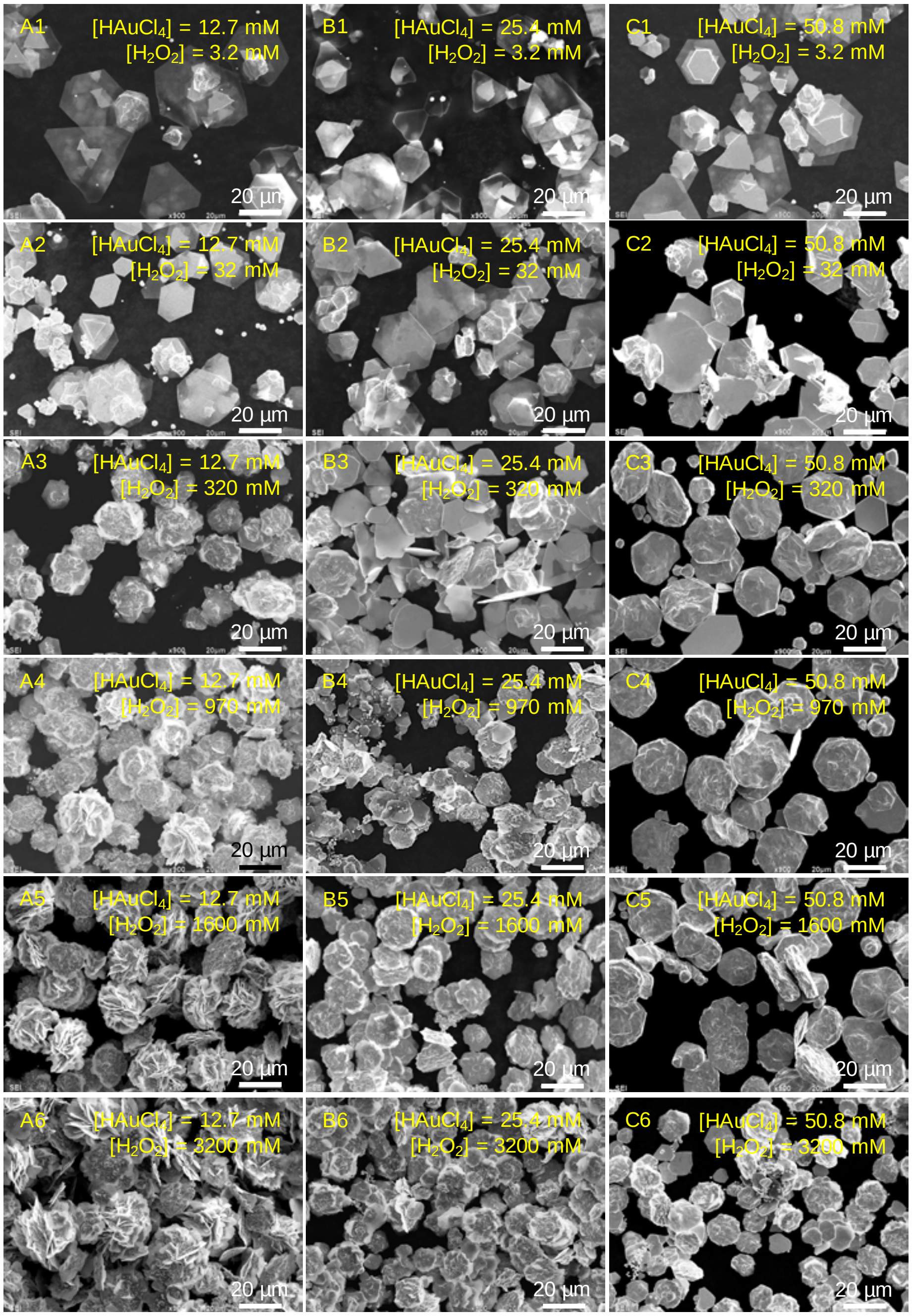

Figure S1 SEM images showing the influence of concentration of $HAuCl_4$ and H_2O_2 on the morphology of gold micro/nanostructures. Gold ions were reduced by H_2O_2 in 1% starch solution.

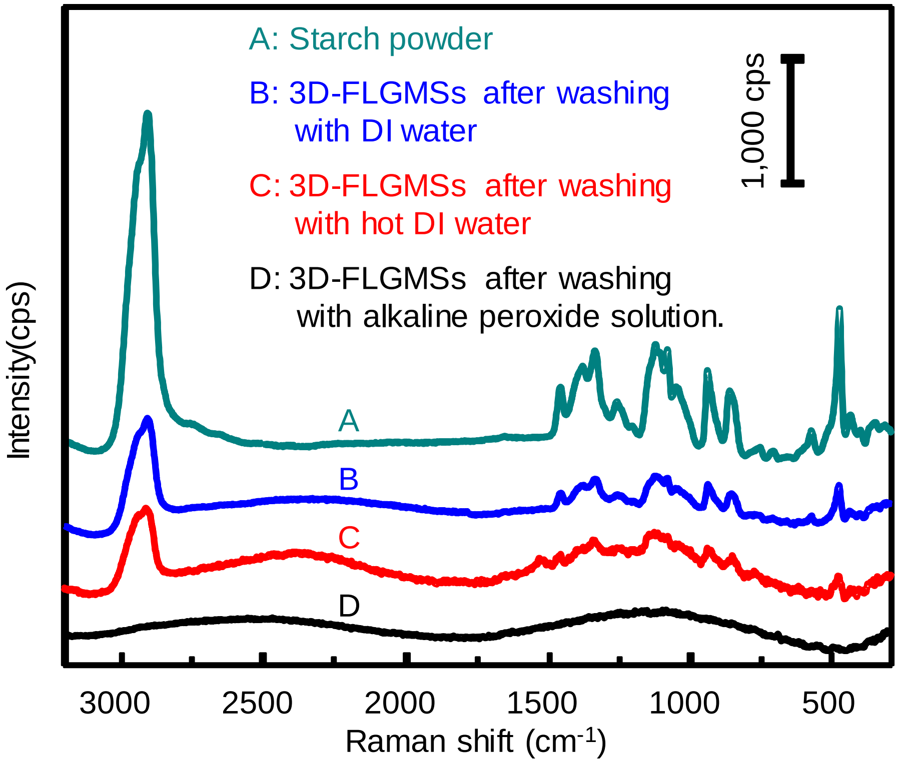

Figure S2 Raman spectra of (A) starch powder on an aluminum foil and 3D-FLGMSs after washing with (B) deionized water, (C) hot deionized water, and (D) alkaline-peroxide solution. The starch molecules on 3D-FLGMSs can only be removed by alkaline-peroxide solution suggest a strong adhesion.

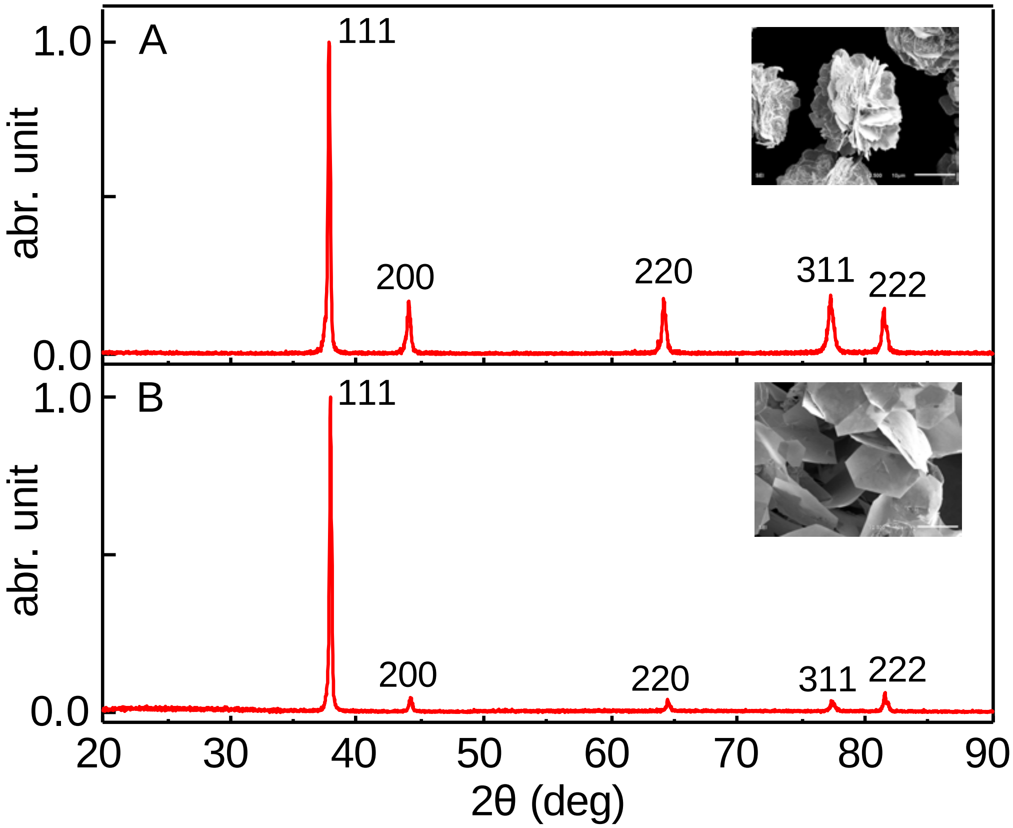

Figure S3 XRD patterns of (A) 3D-FLGMSs and (B) gold nanosheets. The inset pictures indicate the corresponded SEM images.

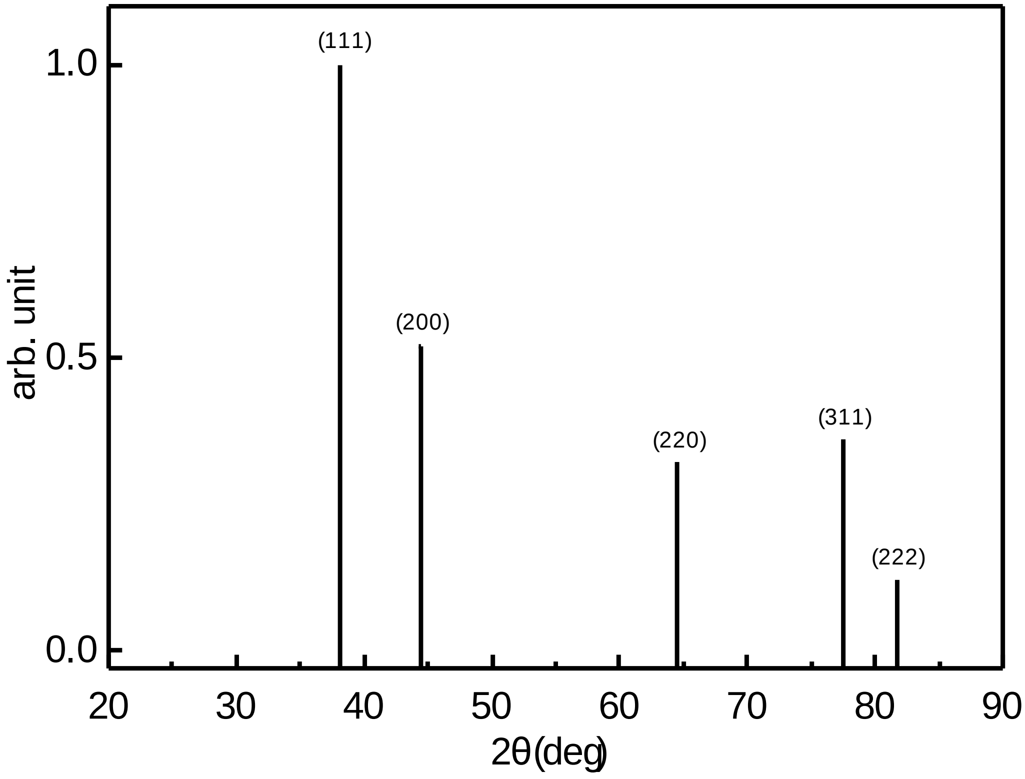

Figure S4 The standard XRD pattern of bulk gold (JCPDS 04-0748).

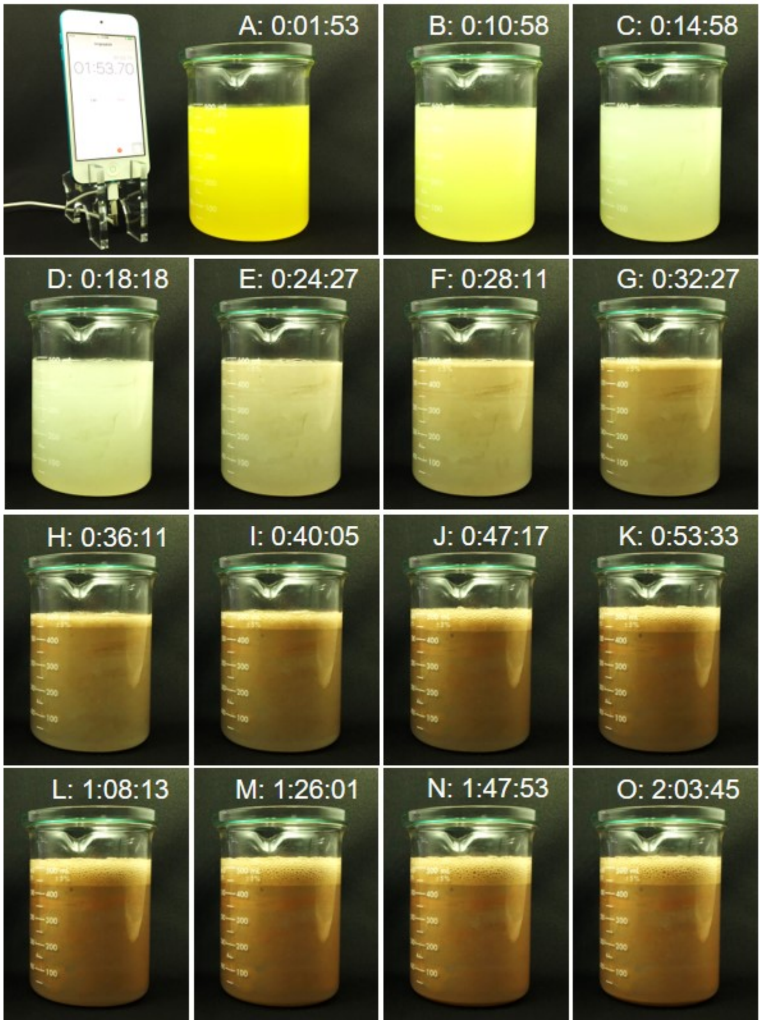

Figure S5 Time-lapse digital photographs illustrate the progress of the reaction in a 3D-FLGMS synthesis. A demonstration of a large-scale preparation of 3D-FLGMS (500 mL solution with a gold metal content of 2.5 g) was conducted by reduction of 12.7 mM $HAuCl_4$ by 3.2 M H_2O_2 in 1% (w/v) starch. It should be noted that although the reaction was completed within 120 min, a large number of bubbles was observed due to the decomposition of the remaining H_2O_2 on gold surfaces [1]. The pictures were captured by an iPhone 6s with time-lapse function.

Reference

[1] Y. Cheneviere, V. Caps, A. Tuel, Gold-catalyzed oxidation of substituted phenols by hydrogen peroxide, Appl. Catal., A 387 (2010) 129-134.

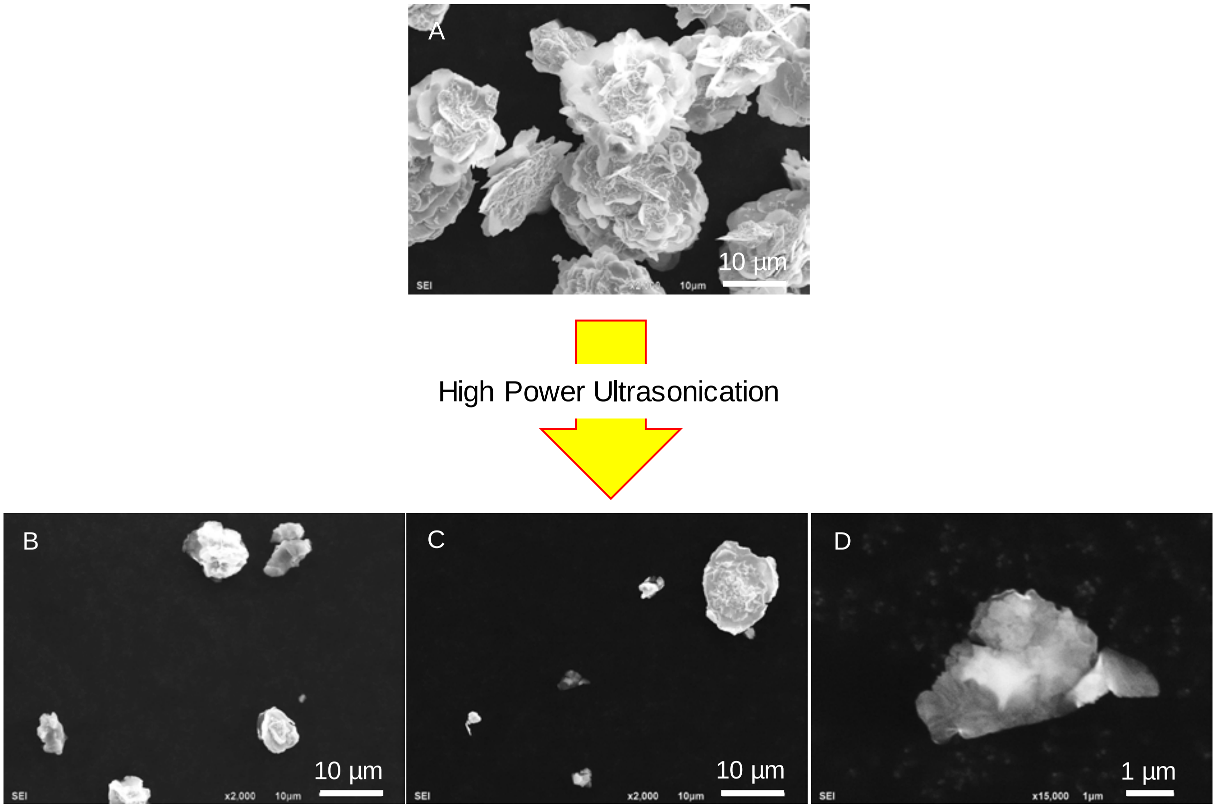

Figure S6 SEM images of 3D-FLGMSs (A) before and (B)-(D) after treating with high power ultrasonication for 5 min.

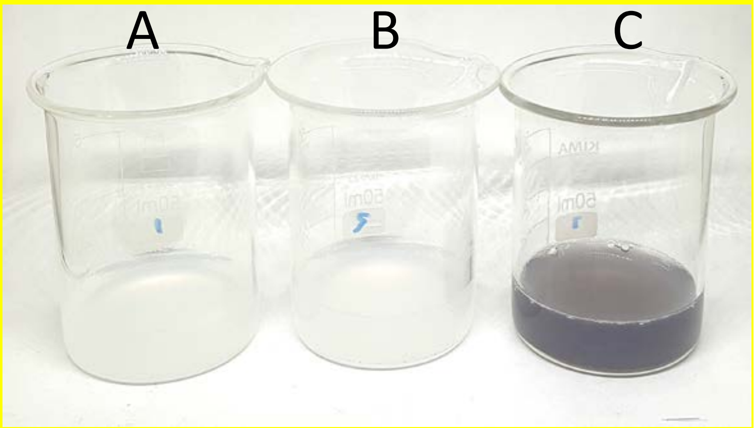

A: Supernatant

B: Supernatant + $NaBH_4$

C: Supernatant (with residual of gold ions)+ $NaBH_4$

*Supernatant contains starch

Figure S7 A digital photograph illustrates a solution of (A) supernatant (B) supernatant + $NaBH_4$ and (C) Supernatant with an additional of gold ions + $NaBH_4$. Hint : $NaBH_4$ represents an added 0.5 mL of 0.5 M $NaBH_4$.

A testing of residual gold ions in supernatant after the synthesis process was performed by dropping of 0.5 mL of $NaBH_4$ (0.5 M). After adding the strong reducing agent, if there are any residual gold ions left in the supernatant, they will be reduced to from gold particles presented as turbid colloids in the solution. As shown in the figure S7, it was found that the supernatant, which obtained from the reaction between 12.7 mM $HAuCl_4$ and 3200 mM H_2O_2 in a solution of 1% w/v starch, does not contain any residual gold ions because there is no observation on the generated turbid colloids after adding $NaBH_4$. Therefore, a 100% conversion of gold ions was confirmed.

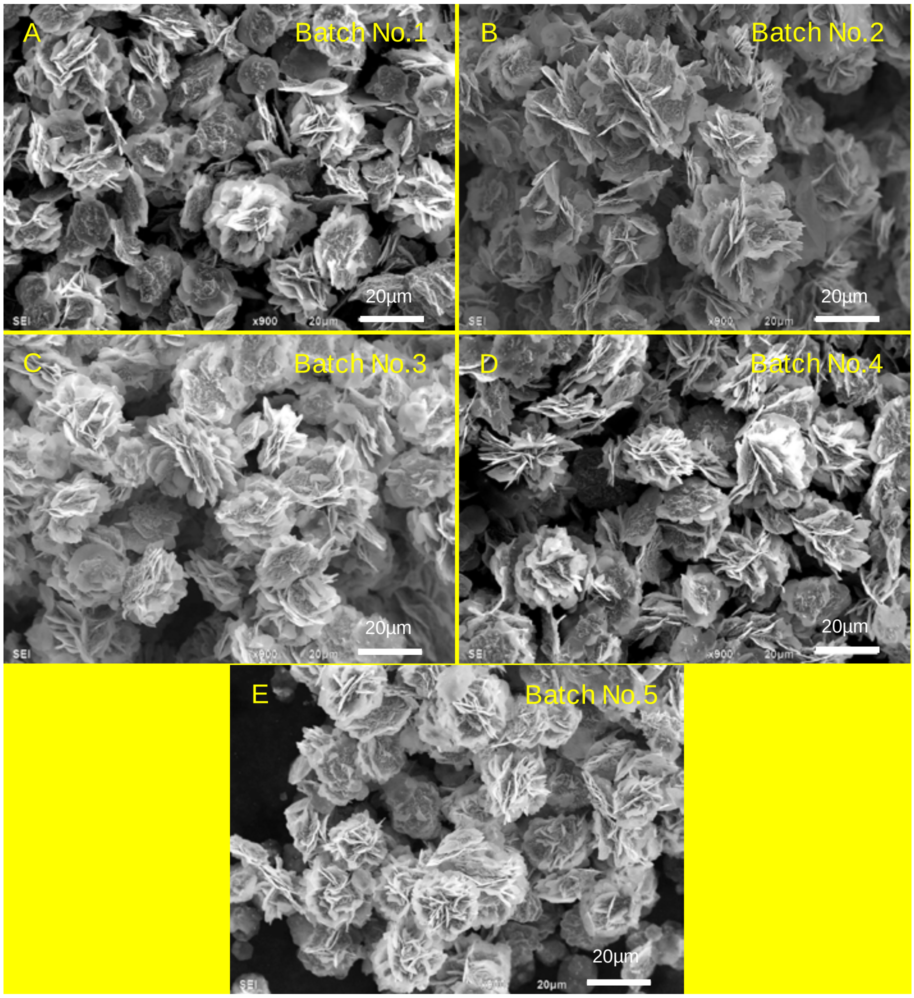

Figure S8 SEM images show the morphology of 3D-FLGMSs obtained from different 5 production batches. The concentration of $HAuCl_4$, starch and H_2O_2 were 12.7 mM, 1% w/v and 3200 mM, respectively. From the figures (A-E), 3D-FLGMSs could be reproduced in all production batches with the same size and morphology. This confirmed that the developed synthesis protocol has met the good reproducibility for the production of 3D-FLGMSs.